NASA/TP–2002-211848
AFDD/TR-02-A-001

Measurements of the Early Development of Trailing Vorticity from a Rotor

Kenneth W. McAlister and James T. Heineck

July 2002

The NASA STI Program Office ... in Profile

Since its founding, NASA has been dedicated to the advancement of aeronautics and space science. The NASA Scientific and Technical Information (STI) Program Office plays a key part in helping NASA maintain this important role.

The NASA STI Program Office is operated by Langley Research Center, the Lead Center for NASA's scientific and technical information. The NASA STI Program Office provides access to the NASA STI Database, the largest collection of aeronautical and space science STI in the world. The Program Office is also NASA's institutional mechanism for disseminating the results of its research and development activities. These results are published by NASA in the NASA STI Report Series, which includes the followintg report types:

- TECHNICAL PUBLICATION. Reports of completed research or a major significant phase of research that present the results of NASA programs and include extensive data or theoretical analysis. Includes compilations of significant scientific and technical data and information deemed to be of continuing reference value. NASA's counterpart of peer-reviewed formal professional papers but has less stringent limitations on manuscript length and extent of graphic presentations.

- TECHNICAL MEMORANDUM. Scientific and technical findings that are preliminary or of specialized interest, e.g., quick release reports, working papers, and bibliographies that contain minimal annotation. Does not contain extensive analysis.

- CONTRACTOR REPORT. Scientific and technical findings by NASA-sponsored contractors and grantees.

- CONFERENCE PUBLICATION. Collected papers from scientific and technical conferences, symposia, seminars, or other meetings sponsored or cosponsored by NASA.

- SPECIAL PUBLICATION. Scientific, technical, or historical information from NASA programs, projects, and missions, often concerned with subjects having substantial public interest.

- TECHNICAL TRANSLATION. English-language translations of foreign scientific and technical material pertinent to NASA's mission.

Specialized services that complement the STI Program Office's diverse offerings include creating custom thesauri, building customized databases, organizing and publishing research results ...even providing videos.

For more information about the NASA STI Program Office, see the following:

- Access the NASA STI Program Home Page at:
  http//www.sti.nasa.gov

- E-mail your question via the Internet to:
  help@sti.nasa.gov

- Fax your question to NASA Access Help Desk at:
  (301) 621-0134

- Telephone the NASA Access Help Desk at
  (301) 621-0390

- Write to:
  NASA Access Help Desk
  NASA Center for AeroSpace Information
  7121 Standard Drive
  Hanover, MD 21076-1320

NASA/TP–2002-211848
AFDD/TR-02-A-001

Measurements of the Trailing Vorticity from a Rotor

Kenneth W. McAlister
Army/NASA Rotorcraft Division
Aeroflightdynamics Directorate (AMRDEC)
US Army Aviation and Missile Command
Ames Research Center, Moffett Field, CA

James T. Heineck
Experimental Physics Branch
Ames Research Center, Moffett Field, CA

National Aeronautics and
Space Administration

Ames Research Center
Moffett Field, California 94035-1000

July 2002

ACKNOWLEDGEMENTS

The authors greatly appreciate the judicious reviews by Wayne Johnson, Preston Martin, William Warmbrodt, and Gloria Yamauchi. Calculations performed by Johnson using CAMRADII showed that $\Gamma_{bmax} = 2.25m^2/s$, $\Gamma/\Omega Rc = 2.61C_T/\sigma$, giving $\Gamma_*/\Gamma_{bmax} = 0.63$, and $\Gamma_c/\Gamma_{bmax} = 0.53$.

Available from:

NASA Center for AeroSpace Information
7121 Standard Drive
Hanover, MD 21076-1320
(301) 621-0390

National Technical Information Service
5285 Port Royal Road
Springfield, VA 22161
(703) 487-4650

Measurements of the Early Development of Trailing Vorticity from a Rotor

Kenneth W. McAlister
Army/NASA Rotorcraft Division
Aeroflightdynamics Directorate (AMRDEC)
US Army Aviation and Missile Command
Ames Research Center, Moffett Field, CA 94035-1000

James T. Heineck
Experimental Physics Branch
Ames Research Center, Moffett Field, CA 94035-1000

ABSTRACT

The wake behind a two-bladed model rotor in light climb was measured using particle image velocimetry, with particular emphasis on the development of the trailing vortex during the first revolution of the rotor. The distribution of vorticity was distinguished from the slightly elliptical swirl pattern. Peculiar dynamics within the "void" region may explain why the peak vorticity appeared to shift away from the center as the vortex aged, suggesting the onset of instability. The swirl and axial velocities (which reached 44 and 12 percent of the rotor-tip speed, respectively) were found to be asymmetric relative to the vortex center. In particular, the axial flow was composed of two concentrated zones moving in opposite directions. The radial distribution of the circulation rapidly increased in magnitude until reaching a point just beyond the core radius, after which the rate of growth decreased significantly. The core-radius circulation increased slightly with wake age, but the large-radius circulation appeared to remain relatively constant. The radial distributions of swirl velocity and vorticity exhibit self-similar behaviors, especially within the core. The diameter of the vortex core was initially about 10 percent of the rotor-blade chord, but more than doubled its size after one revolution of the rotor. According to vortex models that approximate the measured data, the core-radius circulation was about 79 percent of the large-radius circulation, and the large-radius circulation was about 67 percent of the maximum bound circulation on the rotor blade. On average, about 53 percent of the maximum bound circulation resides within the vortex core during the first revolution of the rotor.

INTRODUCTION

Unlike the wake of a fixed-wing aircraft, the wake of a helicopter rotor follows a trajectory that repeatedly passes near portions of the rotor system before it is finally convected downstream. As a consequence, the rotor wake not only has a considerable influence on the performance of the rotor, but it is principally responsible for the high levels of noise and vibration that result from encounters between the rotor blades and their collective wake (ref. 1).

Because of the complexity of the rotor wake, especially concerning the intensity and size of the dominant trailing vortex and its increasingly irregular trajectory, computational modeling of the flow field continues to be a challenge. An impressive effort was made recently to calculate the performance and aeroacoustics of the rotor without knowing the precise structure of the trailing vortex (ref. 2). An equally notable, although computationally demanding, computational fluid dynamics (CFD) code has been developed that attempts to accurately capture the details of the rotor wake development (ref. 3). To achieve this level of accuracy, numerical dissipation must be minimized by imposing very small spatial and temporal step sizes. Even though this highly resolved computational grid is selectively structured in the flow field only where it is most needed, an extraordinary length of time is required to perform the calculations. However, because of a more relaxed grid requirement, shorter computational times have been reported using a CFD formulation that incorporates a vorticity-confinement concept (ref. 4). Reliable experimental measurements are needed to support such efforts.

As new experimental techniques emerge, the rotor wake is frequently revisited in order to extract

more detailed information about the structure of the trailing vortex (refs. 5 – 18). For example, not only does the stereo particle image velocimetry (PIV) measurement technique render all three components of velocity over a sufficiently large cross section of the flow, but the vector fields from a sequence of images taken during successive revolutions of the rotor can also be conditionally ensemble averaged to remove the effects of vortex wander (ref. 17). Given this opportunity to acquire data more efficiently, highly resolved (in space and time) data on the development and aging of the trailing vortex is now possible. In addition to enhancing our physical understanding of the rotor wake, specific characteristics (such as composition, size, intensity, and location) of the trailing vortex at different wake ages will enable CFD models to be validated on a more detailed level.

Many questions have been raised concerning unexpected features appearing within the trailing vortex (ref. 6), the composition of the vortex relative to blade loading (ref. 2), vortex definitions (ref. 19), opinions dealing with the development and demise of vortex systems (ref. 20), and the appropriateness of simple vortex models (ref. 21). In response to these questions, an experiment was performed to provide data that focuses specifically on cross sections of the trailing vortex during a complete revolution of the rotor. The data are of sufficient quality to permit various modeling uncertainties to be resolved. This paper describes the test facility, model, flow measurement technique, and the data-acquisition and -processing procedure. A discussion of the results is provided along with specific findings.

NOMENCLATURE

a	speed of sound, meters per second (m/s)
A	area enclosed by circulation path, m^2
c	chord length, m
C_Q	torque coefficient, torque/$\rho\pi\Omega^2R^5$
C_T	thrust coefficient, thrust/$\rho\pi\Omega^2R^4$
d_h	distance between velocity peaks, horizontal cut
d_v	distance between velocity peaks, vertical cut
M	hover-tip Mach number, $R\Omega/a$
N	number of points to be averaged
N_b	number of rotor blades
R	radius of rotor-tip path, m
R_e	hover-tip Reynolds number, $cR\Omega/\nu$
r, θ, z	coordinates relative to rotor axis
u, v, w	velocity components, m/s
u_c,w_c	vortex-convection velocities, m/s
u_r,w_r	velocities relative to u_c,w_c, m/s
α	angle of position vector, degrees (deg)
β	angle of $\vec{u}+\vec{w}$ vector, deg
Γ	circulation, m^2/s
Γ_c	circulation at core radius, m^2/s
Γ_*	total vortex circulation in far field, m^2/s
δ	turbulent/laminar viscosity, ϵ/ν
ϵ	eddy viscosity, m^2/s
ζ	radius measured from void center, mm
ζ_c	radius of vortex core, millimeters (mm)
ζ_{c0}	value of ζ_c at trailing edge, mm
$\overline{\zeta}$	ζ/ζ_c
θ	local angle of rotor blade, deg
κ	radius measured from vorticity centroid, mm
λ	dimensionless hover-inflow velocity, $w_i/\Omega R$
ν	kinematic molecular viscosity, m^2/s
ρ	fluid density, kg/m^3
σ	rotor solidity, $N_bc/\pi R$
φ	swirl velocity, m/s
φ_c	swirl velocity at core radius, m/s
$\overline{\varphi}$	φ/φ_c
ψ	azimuthal wake age measured from blade, deg
ω_θ	vorticity normal to $r-z$ plane, per second
Ω	rotor revolutions per minute, rpm

ABBREVIATIONS

CCD	Charged coupled device
CFD	Computational fluid dynamics
LDV	Laser Doppler velocimetry
PIV	Particle image velocimetry

TEST DESCRIPTION

Test Facility

This experiment was performed in the settling chamber of the 7- by 10-Foot Subsonic Wind Tunnel at Ames Research Center (fig. 1). This location was selected to take advantage of the relatively large cross section of the tunnel (9.4 m x 10.0 m) and to better isolate the flow field around the rotor from ambient wind fluctuations external to the facility.

A model rotor was placed in the center of the settling chamber and mounted horizontally with its axis of rotation coincident with the centerline of the test section. Aside from the influence of the tunnel walls (approximately 4.6 m away) and the contraction into the test section (with an area ratio of 14:1), the rotor wake was allowed to pass through the test section without interference. A curtain was drawn across the air-exchanger section to prevent the wake from recirculating around the tunnel and contributing to an unwanted climb condition. In this configuration, any portion of the wake reaching this section would be expelled through the air-exchanger doors and fresh stagnant air would be drawn by the rotor into the tunnel circuit (as required by mass continuity).

Video cameras were mounted upstream and to the side of the rotor to monitor critical elements during the test (fig. 2). It is customary to infer the velocity in the test section from the differential pressure between the settling chamber and the test section. However, this procedure does not reveal the nonuniform character of the flow across the test section (due to blockage by the PIV apparatus in the settling chamber) and is not sufficiently accurate at low speeds. Therefore, the velocity in the test section due to the rotor wake was measured with a vane anemometer (1 to 39.6 m/s range) attached to an existing tunnel traverse. In the settling chamber, where the velocity was considerably lower, a hot-film probe was used to measure velocity (0 to 2.4 m/s range) directly upstream of the rotor at a distance of about 8.5 meters from the tip-path plane.

Model Rotor

The rotor used in this experiment was a 1/7-scale model of the full-scale AH-1/OLS rotor. The profile of this blade was based on a simple trailing-edge extension to the shape of a NACA 0012 airfoil (fig. 3). The rotor consisted of two blades, each with a chord of 103.9 mm, maximum thickness of 10.2 mm, and a span of 957.6 mm measured from the axis of rotation to the blade tip (fig. 4). Beginning at 25-percent radius, the twist of each blade was $-0.106°$/centimeter (cm), so that the total variation in geometric twist along the span was 7.55° (from the center of rotation to the rotor tip). Collective pitch settings were referenced to the geometric pitch angle at 75-percent radius. Therefore, a collective pitch setting of zero meant that the blade pitch was about 5.0° at the root (held fixed for locations less than $R/4$) and $-2.5°$ at the tip. The rotor hub had a built-in blade precone of 1.30°.

Information related to safety of flight was obtained by flap- and chord-bending gages mounted on the blade. The drag link used to adjust the blade sweep was instrumented with a strain gage that responded to the aerodynamic drag on the rotor, offering a redundant measurement of chord-wise bending. Depending on the sweep of the blade and the location of the center of mass of the blade, this gage could also be loaded by a centrifugal force induced moment. Strain gages were placed on the pitch horns that transmitted commanded pitch to the rotor blades. Reactions to these commands resulted in bending loads on these elements that were proportional to the torsional moments on the blades. A transducer for measuring the angular tilt of the rotor (called the teeter pot) was mounted on top of the hub. The rotor operator monitored the signals from each of these gages. Because the center of mass of each rotor blade was located aft of the feathering axis (aligned with the quarter chord), it was necessary to sweep the blades forward 1.20° to minimize steady chordwise bending due to centripetal force. The blades were strobed at 2/revolution (rev) to verify that the blades were tracking. A blade sweep of 1.20° corresponded to a $0.19c$ forward movement of the tip.

The model rotor was attached to a teetering hub, which in turn was mounted on the VSB-54 force and moment balance. The most significant element of the balance in the present test was the axial gage, which had a capacity of 159 kilograms (kg) and provided a measure of the rotor thrust. Rotor torque was measured using torsion gages mounted on a flex coupling located between the balance and the transmission, and had a capacity of 74.7 kg-m. The rotor was driven by a 90-horsepower (HP) electric motor through a 4:1 transmission. The complete rotor and drive system (fig. 5) was supported on a tripod-like structure that was rigidly attached to the frame of the wind tunnel. This setup placed the tip-path plane of the rotor about 1.8 m upstream of the beginning of the contraction section of the tunnel, well within the protective steel-wall section of the tunnel.

Stereo PIV Setup

The primary elements of the PIV system consisted of a pulsed laser, optics to spread the beam into a thin sheet, charged coupled device (CCD) cameras to record the images, and a calibration target. The plane of the light sheet was horizontal and passed just below the trailing edge of the rotor when the rotor was at zero azimuth (fig. 6). In order for both cameras to receive close to the same amount of forward-scattered light, two opposing, coplanar light sheets were established (figs. 6 and 7). To avoid interference with the model supports, the cameras were placed at different distances away from the light sheet (nominally 1.5 m) and at different angles. Two Nd:YAG lasers, 120 millijoules (mJ) each, were positioned and synchronized. Cameras and lasers were triggered off of a 1/rev reference signal that was keyed to the rotor. This signal was obtained by directing a small continuous-wave laser beam onto a small mirror attached to the hub of the rotor and intercepting the reflected beam with a fast-response photodetector. Acquisition software was used to delay the reference signal in order to obtain data at different wake ages.

Images were acquired with 8-bit CCD cross-correlation cameras, each having a sensor array of 2K $\times$ 2K pixels (nominal). Each pixel measured 7.4 microns (μm) on a side. The cameras were operated in a double-exposure mode to acquire two noninterlaced, full-frame images during a single frame interval. These were nonstandard video cameras that could be

externally triggered and driven at any frequency up to 15 Hertz (Hz) in double-exposure mode. A computer interface provided control over gain, contrast, black level, and trigger mode. Because the cameras were located at different distances from the object plane, one used a 55-mm lens, while the other used an 85-mm lens. The lenses were remotely translated to focus on the centerline of the image area, and the sensor (located inside the camera body) was rotated about its centerline to satisfy the Scheimpflug condition[1].

Each Nd:YAG laser was frequency doubled to provide a beam having a wavelength of 532 nanometers (nm), a pulse width of about 4 nanoseconds (ns), and power of 120 mJ. The laser beam initially had a diameter of about 5 mm and a divergence of 0.60 milliradians (mrad). In this test, each laser-light sheet was formed by first passing the beam through a set of spherical lenses (consisting of focal lengths of -500 mm and $+500$ mm). By adjusting the distance between these two lenses, the beam waist (or sheet thickness, approximately 1 mm thick) could be positioned in the region imaged by the cameras. Two cylindrical lenses (with focal lengths of -12.7 mm and $+25.4$ mm) were used to expand the beam in the horizontal direction. The distance between the sheet-forming optics and the imaged area was about 1.5 m.

The lasers, sheet-forming optics, and cameras were rigidly mounted on a common structure, which could be traversed in three orthogonal directions. This arrangement allowed the cameras to be focused only on the trailing vortex region of the flow, and then traversed as required to follow the position of the vortex at different wake ages.

Prior to taking data, a flat aluminum plate, with a 15- by 23-cm rectangle precisely milled into the surface, was used to calibrate the camera views. The calibration plate was leveled and the light sheets adjusted so as to evenly graze the surface. The lens of each camera was traversed along its optical axis and the CCD sensors were rotated until a uniform focus on the calibration target was achieved. The calibration supplied all the parameters required to accurately dewarp the images and construct the three-component velocity fields.

Proper seeding of the flow is critical for obtaining accurate PIV measurements. The seed particles must be evenly distributed and of sufficient density to define the flow without altering its physical properties. The particles must also be small enough to accurately follow the flow (especially challenging in accelerating flows), yet large enough so that they scatter a sufficient amount of light to be detected. The particle generator used in this test employed an inert gas to atomize a nontoxic, pharmaceutical-grade mineral oil. The mist was vaporized and then condensed before being released into the flow. The particle size was estimated by the manufacturer to be less than 0.5 μm. The particle generator was located upstream of the settling chamber so that the particles would mix with the air entering the tunnel circuit before being drawn into the wake of the rotor.

Calibration, data acquisition, and image processing were all performed using ProVision software developed by Integrated Design Tools (IDT). The principles of the PIV technique and the application of this software to the study of vortex-dominated flows are discussed in greater detail in reference 17.

PROCESSING WAKE IMAGES

After completion of the test, the data were processed on a PC workstation. To obtain good resolution of the trailing vortex, a calculation grid measuring 92 horizontal nodes by 79 vertical nodes was constructed over the region of significant interest in the flow field. The area covered by the grid resulted in approximately 12 pixels between nodes in both directions, as determined by (Grid range in terms of pixels)/(Number of nodes -1). The interrogation window was set at 22 pixels on a side, giving a 45-percent overlap according to (Interrogation window $-$ Interval between nodes)/(Interrogation window). The physical area measured in each image zone was 168 mm (with an axial increment of 1.8 mm) by 106 mm (with a radial increment of 1.4 mm). The 1.8- by 1.4-mm increments, which defined the calculation step sizes in the axial and radial directions, also defined the resolution of the measurements. Therefore, the interrogation window (containing 484 pixels) covered an area measuring 2.5 mm in the radial direction by 3.4 mm in the axial direction.

Consider an interrogation area (fig. 8) in which 10 particle pairs (the minimum number required to yield a valid resultant vector) have been registered on a 22- by 22-pixel image of a small region in a swirling flow. The software derives a representative in-plane velocity vector based on a second-order calculation of all the individual particle displacements within that interrogation area. Note that the effective "probe size" is, therefore, less than the interrogation area. All the rotational velocity components within the vortex are accounted for, but they are represented in a collective sense over contiguous regions defined by the size of the interrogation area. For an initial core diameter of 10 mm, the core would have been covered by about nine interrogation areas (78.5 $mm^2/8.5\ mm^2$). Considering an interrogation overlap of 47 percent means that about 18 vectors would be

[1]Uniform focus requires that the light sheet, camera lens, and camera sensor planes intersect along a common line (see fig. 7).

calculated within the vortex core. Given that the size of the vortex grows as it ages, the number of vectors calculated within the core would also increase. In this present test, for example, a vortex that had grown to a diameter of 20 mm would contain about 72 vectors.

A single file for each wake age included a flag for every velocity measurement that indicated the nature of that vector (such as valid, invalid, interpolated, recalculated, or not calculated). Reduced data files containing the coordinates of each calculation node and the three components of velocity (in terms of displacement) were stored in ASCII format and then transferred to a mainframe computer for analysis. The velocity components were first converted from displacement units to velocity units based on the pulse duration for that particular measurement. The physical coordinates were transformed so that $r = z = 0$ would correspond to the center of the rotor hub (fig. 6).

Because of centripetal effects, heavier seed particles appear to have been driven outward from the center of the vortex as it moved through the fluid. Because the size of the remaining lighter particles were most likely much smaller, less light would have been scattered from this region, thereby giving it the appearance of a "void." Nevertheless, the particles that were present inside the void were sufficient to obtain PIV measurements. In searching for vortex characteristics that can be known with certainty, the size of the "apparent void" cannot always be equated to the size of the core, nor can the center of the void be assumed to be coincident with the center of swirl. On the other hand, the physical location of the void was an indisputable feature and was, therefore, judged to be the most reliable indicator of how the vortex was convecting through the fluid. In addition, in order to account for the ever-present vortex meander, the coordinates of the voids for a set of images acquired over time at a particular azimuth behind the rotor provided a very accurate basis for conditionally averaging the images.

The distribution of particles around an apparent vortex void often exhibited a peculiar pattern (fig. 9). Particles were not always uniformly distributed in the flow as it approached the rotor. In these instances, some form of particle "banding" frequently occurred adjacent to the void region. Calculations have been made that show that banding is also a natural consequence of the balance of forces (drag, centrifugal, and Coriolis) that act on the seed particles within a vortex (ref. 22). Small particles settle in an annular region that is smaller than the vortex core, compared to larger particles that yield a band that is larger than the vortex core. Regardless of how uniform the flow appeared to be seeded in the present experiment, a fairly broad range of void sizes was observed at all wake ages (fig. 10). The average size of the void increased rapidly during the first 100° of azimuth, after which the rate of increase diminished substantially.

In this study, the sequence for extracting the characteristics of the trailing vortex began with a physical examination of each raw image to determine the size and location (relative to a superimposed mesh) of the apparent void (fig. 11). At each wake age the images were averaged to smooth out the small irregularities that were invariably present in the flow. Because the vortex was located at different positions from image to image (vortex meander), performing a simple average would have risked smearing out important details concerning the structure of the vortex. Instead, the data were averaged only after aligning the set of images based on the most dominant recurring feature in the flow, which in this case was the apparent void.

This procedure is referred to as conditional ensemble averaging, the condition here being the alignment of all the images in the set based on their void centers. The image with a void center closest to the mean location that was established for the set of images was selected as the "anchor." The indices of all image matrices (that is, grid points i,j) for each wake age were then adjusted according to the offset of each void from the coordinates of the void in the anchor image. All data in the anchor image were retained. However, some portion of all other images with adjusted indices that fall outside the boundaries of the anchored image were necessarily discarded. Hence, as a consequence of vortex wander, the population contributing to the conditional average was greatest over the interior of the matrix (or calculation grid).

At this intermediate point, the conditionally averaged flow field at each wake age embodies the trailing vortex within a highly nonuniform downwash. The time-averaged downwash for a single-bladed rotor can be determined by averaging the flow field over an entire revolution of the rotor (refs. 8, 10). When the time-averaged downwash velocity field is subtracted from the phase-averaged velocity field, the resulting velocity profiles tend to appear more symmetric along the extremities of the vortex, but not near the core radius (ref. 8). In the present experiment, this procedure could not be implemented because data were not obtained over the required half revolution in each zone. However, the axial and radial locations of the voids at each wake age, along with the known time intervals between each wake age, were known and did yield the convection velocity of the vortex at each wake age. These components of the convection velocity, u_c and w_c, were subtracted from the phase-averaged flow field. However, because the axial component of the downwash over the inboard region was significantly higher than the axial convection velocity

of the vortex (w_c), velocity profiles across the center of the vortex cannot be expected to be symmetric.

To extract information about the geometry of the vortex (after performing averages based on the void centers at each wake age), the center of the vortex was assumed to be at the center of swirl[2]. Using the void center as a starting point, the surrounding locations were interrogated to determine the best node for which the sum of the dot products of two unit vectors produced a minimum over a neighborhood[3] of locations surrounding the candidate node. The coordinates of the neighboring node relative to the candidate node defined one of the unit vectors. The velocity vector at the neighboring node defined the other unit vector. With the angles of these two unit vectors denoted by α and β (fig. 12), the node nearest the center of swirl was said to be found when the following expression was a minimum:

$$\sum_{n=1}^{N} |\cos(\alpha - \beta)| / N \qquad (1)$$

where N is the total number of neighboring points considered. Relative to the center of swirl for a pure vortex in a stationary flow, α and β will be orthogonal for all neighboring points and the sum will be exactly zero. For most real flows the sum will not be precisely zero, and the procedure works best when the neighborhood under consideration does not extend beyond about one or two core diameters (which is normally sufficient to cover most of the vorticity in a single trailing vortex).

The size of the vortex core was found by first dividing the surrounding region into annular zones and calculating the average swirl velocity and the associated mean radius of each annulus. These data were fit with a least-squares spline subject to the condition that the resulting curve have only one inflection along its inner extent (nominally set to twice the estimated core radius). The point of inflection was used to define the radius of the vortex core, because that is where a maximum value for the swirl velocity is reached. This procedure was considered to offer a more rational approach for determining the size of the vortex, especially when the velocity peaks that are characteristic of vortices (and upon which core sizes are traditionally based) are dependent on how the vortex is sliced (vertical, horizontal, or otherwise).

Vorticity was calculated by integration (circulation box method) according to:

$$\omega_\theta = A^{-1}\Gamma = A^{-1} \oint (\vec{u}, \vec{w}) \cdot d(\vec{r}, \vec{z}) \qquad (2)$$

where the direction of integration was such that the enclosed area, A, was on the left of the integration path. The size of each circulation box was defined by the local grid spacing, which on average rendered $A = 2.5$ mm^2.

Test Conditions

The experiment was performed at a constant rotor speed of 870 rpm (14.5 Hz), which for a rotor diameter of 191.5 cm corresponds to a tip speed of 87.2 m/s. Based on an average ambient temperature of 16.7 degrees Centigrade (°C), the Reynolds number based on rotor-tip chord was $R_e = 0.6 \times 10^6$ and the Mach number was $M = 0.26$. The collective pitch angle of the rotor was fixed at 11°.

To obtain high-resolution PIV images, the cameras were focused on a small region of the wake behind the trailing edge of the rotor. The camera view was radially and axially translated to provide three zones of coverage (A, E, and F). The PIV measurement locations (which were selected to follow the vortex development at different wake ages), along with the laser pulse delays needed to capture the highest velocities, are shown in table 1. Results presented later in this report show that even for the longest pulse delay, 5 microseconds (μs), the vortex moved less than 1/1000 of the core radius between pulses. The blade was considered to be at zero azimuth when the trailing edge of the rotor blade was horizontal. When the blade is in this position, the light sheets (both of which intersect in a horizontal plane) pass just beneath the trailing edge of the blade. The procedure for taking images at the different wake ages was accomplished by delaying the 1/rev signal from the rotor, thereby allowing the tip of the rotor blade to move past the measurement plane by the desired azimuthal increment. The data were taken at a nominal increment of 15° (fig. 13), with some exceptions as required to avoid reflections of the laser light from any portion of the blade surface that might damage the camera sensors.

RESULTS AND DISCUSSION

Rotor Performance

Rotor loads and tunnel velocity measurements (fig. 14) were taken from an earlier experiment (ref. 18). The colors used in the contour plots of the test-section velocity for each collective angle are scaled so that red represents the maximum velocity (and blue the minimum) for that case. Strictly speaking, the rotor is not in hover, as evidenced by the magnitude

[2]Neither the void center nor the swirl center was necessarily at the center of the vorticity that was accreted from the rotor wake, itself having the form of a spiraling sheet containing varying amounts of vorticity.

[3]Because the quality of the data within the void may be in question, these vectors were omitted during this operation.

Table 1: Measurement locations

Wake age, deg	Zone	Pulse delay, μs
0	A	5.0
15	A	5.0
30	A	5.0
45	A	5.5
60	A	5.0
75	A	5.0
90	A	4.5
105	A	4.5
120	A	4.5
135	A	4.5
150	A	4.5
180	E	5.0
195	E	3.5
210	E	4.0
225	E	4.0
240	E	4.0
255	E	4.0
270	F	5.0
285	F	5.0
300	F	5.0
315	F	5.0
328	F	5.0
344	F	5.0
375	F	5.0
390	F	5.0

of the velocity upstream of the rotor. Because the flow around the rotor is bounded by the wind tunnel walls, and because the rotor wake lowers the pressure in the test section (in turn inducing a finite flow everywhere ahead of the rotor), a slight climb condition cannot be avoided (see ref. 18 for a full discussion). Assuming the upstream velocity entirely represents the climb velocity, then the climb rate for this part of the experiment can be calculated from $w_\infty/R\Omega$, and is included with other relevant quantities in table 2.

Rotor Wake

The center of the vortex void, the center of vorticity, the center of swirl, and the center between velocity peaks are all considered to be distinct quantities. For each wake age, starting with $\psi = 0°$, the flow field has been summarized in terms of quantities that focus on the trailing vortex (*i.e.*, fig. 15). Vortex wander was qualitatively identified by plotting the locations of the vortex voids for each image set relative to the calculation grid that was used to compute the flow field. Only two grid steps in each direction are shown. To the right of this plot is a sketch of the rotor showing the location of the rectangular zone covered by

Table 2: Rotor loads

Rotational speed of rotor, rpm	870
Collective pitch angle, deg	11
Solidity	0.0691
Torque, foot-pounds (ft-lbs)	11.69
Thrust, lb	39.76
Upstream velocity, ft/s	1.28
Climb rate	0.0045
Hover figure of merit	0.61
C_T	0.00657
C_Q	0.00062
C_T/σ	0.095

the entire calculation grid (92 steps in the z direction and 79 steps in the r direction). The three field plots in the left-most column show the out-of-plane vorticity, $\vec{\omega}_\theta$ (contours with red and blue hues to indicate direction and a continuous range of saturations to indicate magnitude), inplane velocity relative to the convection velocity of the vortex, $\vec{u}_r + \vec{w}_r$ (vectors with a continuous range of hues to indicate magnitude), and the out-of-plane velocity, $\vec{v}$ (contours with red and blue hues to indicate direction and a continuous range of saturations to indicate magnitude). The three profiles in the center column show $\vec{\omega}_\theta$, $\vec{w}_r$, and $\vec{v}$ along z = Constant and passing through the center of swirl. The central portion of these profiles is shown in red and demarcated with dashed vertical lines in order to identify the void region. The horizontal and vertical dashed lines included in each of the field and profile plots mark the location of the swirl center.

The lower plot in the right-most column shows the inplane swirl velocity, φ, averaged over incremental annular regions with radii (ζ) measured from the swirl center. The upper plot in the right-most column shows an enlargement of the inplane velocity ($\vec{u}_r + \vec{w}_r$), limited to a region twice the diameter of the vortex core. The two circles identify the size of the vortex core (solid curve) and the vortex void (dashed curve). Finally, values are given at each wake age for the void center, the vorticity center (or centroid of vorticity), the swirl center, the vortex convection velocity (obtained from the path of the vortex voids), and the core radius along with the maximum swirl velocity (both of which are fixed by the peak value found from the curve fit to φ *vs.* ζ). These values are also given in tables 3 to 5.

Based on a review of the data for all wake ages (figs. 15 – 39), the highest velocities are found to occur within the first 15 degrees behind the rotor blade. During this interval, the maximum inplane (swirl) and out-of-plane velocities reached 44 and 12 percent of

the rotor tip velocity (87.2 m/s), respectively. Although the degree of vortex wander was somewhat erratic, it generally increased with wake age. On average, the standard deviation (based on the mean location of the void center) was only about 9 percent of the diameter of the vortex core (the worst case being 18 percent). The calculated locations of the vorticity, swirl, and velocity-peak[4] centers generally differed from the void center by about 11, 26, and 11 percent of the vortex diameter, respectively (fig. 40). There was no apparent correlation between the void and swirl centers from image to image.

The out-of-plane velocity exhibited the most unusual appearance. Aside from the boundary layer wake that is shed from the trailing edge of the rotor blade and is most distinct when $\psi \leq 30°$ (figs. 15 – 17), there appear to be two concentrated zones of oppositely directed flow near the center of the vortex. Because both of these zones are generally offset from the vortex center, the bisecting profiles taken along z = Constant do not reveal the magnitude of the "excess" and "deficit" velocities that contribute to the overall structure of the trailing vortex.

Even though the convection velocity of the vortex at each wake age has been subtracted, the relative "vertical" component of velocity, $\vec{w}_r$, exhibits an asymmetric profile. Greater symmetry near the vortex may be achieved by subtracting the local downwash, which can only be approximated from a time average of the flow field at corresponding locations over one or more revolutions (refs. 8, 10). However, it is not clear that this effort will yield any better understanding of the vortex structure, especially because the resulting profiles (including the peaks) will still be asymmetric (refs. 8, 13). Given the inevitable likelihood of asymmetry, traditional estimates of the core size and peak velocity would still have to be based on an average between the two halves of the asymmetric profile, and this is effectively what is already provided in the more general annular averages that produce the φ *vs.* ζ plot. Nevertheless, the profile plots are important because they retain certain nuances that can prove helpful in explaining other unexpected features in the flow.

During the initial development of the trailing vortex, $\psi \leq 30°$, the vorticity within the vortex reached a peak value very near the center of the vortex, and rapidly diminished to near zero at a distance not far beyond the core diameter. For larger wake ages, $\psi \geq 45°$, the peak values of vorticity appear to reside in an annular region defined by the size of the void, yet are clearly within the core diameter. Assuming these measurements are valid, this variation in vorticity would imply that much of the interior region of the vortex was not fully in solid-body rotation. Evidence for this can be found in the vertical component of velocity, $\vec{w}_r$, which shows a change in the slope near the vortex center (see, for example, the profile at $\psi = 255°$ appearing in fig. 31). This peculiar departure from the traditional view of a vortex has appeared in other rotor vortex data (ref. 6, where the flow was seeded with incense particles and measurements made with a laser Doppler velocimetry (LDV) technique, and ref. 23).

To be sure, other explanations (seeding being among them) for the unusual velocity and vorticity profiles over the interior of the vortex are plausible. Although centripetal effects may have been a factor, the extent to which the velocity within the core was significantly altered is unknown because the size of the particles was not measured. Another factor may have been the rival between legitimate, but barely visible, small particles and the presence of sensor noise, the result being an abundance of interpolated vectors within the void region. Until these issues can be more thoroughly addressed, it is uncertain whether the data show an onset of vortex instability; reflect a difference in particle dynamics because of a nonuniform distribution of particle sizes in a highly accelerated flow; or are simply due to a processing limitation arising from a marginal scattering of light from very small particles that resulted in incorrect interpolations.

The location with the greatest number of interpolations always occurred within the void region. The number of interpolated values contributing to the average at these "worst-case" locations ranged from 16 to 60 percent. Although far from ideal, no location consisted solely of interpolated values.

To address a possible flaw in the logic used to average the data during the analysis phase, the case for $\psi = 195°$ was reexamined. First, the results for single images (hence, unaveraged) were individually studied to see if the nonlinear slope in the core velocity might simply have been an artifact of the averaging process. Although the unaveraged velocity profiles were noticeably more "noisy," the peculiar change in slope near the center of the vortex was found to be present and similar to the conditionally averaged results. As a final check, a different criterion was considered for obtaining the conditional average. In this case the more classical approach of using the midpoint between the velocity peaks (highest maximum and minimum values occurring during horizontal cuts across the vortex) was adopted. Again, the variation in slope across the vortex was essentially unchanged from that observed when the conditional averaging criterion was based on the locations of the voids. In fact, the same conclusion was reached after considering the swirl centers as

[4]The velocity-peak center is based on the locations that define d_h (see fig. 41).

the averaging criterion.

Another curious feature of the vortex is its slightly elliptical shape. This was also observed in the flow pattern constructed from LDV measurements in the near wake of a hovering rotor (ref. 24). A minor amount of ellipticity can be attributed to the fact that the axis of the vortex is not perpendicular to the plane of the light sheet. This would cause the vortex to appear stretched in the radial and axial directions (relative to the rotor coordinates). The amount of stretching in both directions was nearly the same during the early wake ages, thereby increasing the apparent core size by about 0.06 percent and having essentially no effect on ellipticity. As the vortex aged, the apparent stretching became progressively more biased in the axial direction (because the radial displacement was approaching a constant), but the degree of ellipticity caused by the angle of the vortex axis was still less than 0.4 percent after one revolution. Judging by the amount of ellipticity observed in the data (sometimes reaching an aspect ratio of about 1.23), and by the alternating orientation of the major axis, the cause for this elliptical flow pattern cannot be due to a changing angle of the vortex axis as the vortex ages (unless small-amplitude undulations are superimposed on the vortex trajectory, although the data in figure 40 do not show this).

To study this phenomenon in more detail, the dimensions of the vortex (major and minor axes) were equated to the distances between the velocity peaks found from horizontal and vertical cuts across the center of the vortex (fig. 41). The peak-to-peak distances associated with the horizontal and vertical cuts were designated by d_h and d_v, respectively, and these are shown for wake ages $\psi = 0°$ to 390°. Using red and green color bars to indicate the size of d_h relative to d_v, the data suggest that the elliptical pattern is rotating. This figure also shows that the nonlinear behavior of the velocity profile within the core does not depend on the direction of the cut (horizontal or vertical) or the direction of the major axis of the ellipse (horizontal or vertical).

According to the location of the void center, the radial and axial coordinates of the vortex with increasing wake age are known (fig. 42). Based on curve fits to this data, the corresponding convection velocities were calculated. These data indicate that the highest radial velocity occurred immediately after the trailing vortex left the trailing edge of the rotor. This figure shows that the magnitude of the radial velocity rapidly decreased and then approached an asymptotically diminishing value near the completion of one rotor revolution. The behavior of the axial velocity component was quite different. The magnitude of the axial velocity was lowest immediately after the trailing vortex left the rotor, but then increased until its progress was noticeably impeded after the passage of the following rotor blade. The velocities may have a slightly different appearance if curve fits to the data are separated into segments before and after passage of the second blade ($\psi = 180°$). The wake contraction can also be viewed in the r-z plane (fig. 43), which shows the characteristic "knee" due to the influence of the second blade, and the increasing dominance of the axial velocity as the wake aged.

Based on the radial distribution of the swirl velocity at each wake age (figs. 15 – 39), the peak (or inflection) in the curve fit was used to define the core size and the maximum swirl velocity. The initial diameter of the vortex core was about 10 percent of the chord of the rotor blade ($c = 104$ mm) and more than doubled its size after one revolution of the rotor (fig. 43). The maximum swirl velocity was highest during the initial formation of the trailing vortex, decreased rapidly during the first half revolution, and settled on a nearly constant value (on average) during the last half revolution of the rotor. It is difficult to say exactly how the intensity of the vortex (which is related to the maximum swirl velocity) changed with wake age because of the unavoidable influence of the downwash on the magnitude of the swirl velocity (the vortex is embedded in a nonuniform velocity field).

To examine more closely the structure of the trailing vortex, contour plots of the vertical component of velocity, $\vec{w}_r$, and the out-of-plane vorticity, $\vec{\omega}_\theta$, are shown at wake ages $\psi = 15°$ and 195° along with profiles taken from several closely spaced horizontal cuts across the vortex (figs. 44 and 45). The velocity profiles are clearly more linear within the core of the vortex at $\psi = 15°$ than they are at $\psi = 195°$ (fig. 44). The corresponding vorticity profiles exhibit a single peak when crossing the vortex at $\psi = 15°$, whereas a double peak is evident along several cross sections of the flow at $\psi = 195°$ (fig. 45).

Another point of interest is the radial distribution of circulation across the vortex. Using the swirl velocity to calculate the circulation, and normalizing both φ and Γ by values existing at the core radius (ζ_c), results for $\psi = 15°$, 195°, and 375° are shown in figure 46. As the distance increased from the center of swirl ($\zeta = 0$), the circulation rapidly increased until reaching a point just beyond the core radius, after which the rate of growth decreased significantly.

Similar to the selected views of circulation, the radial distribution of vorticity was examined during the development of the trailing vortex. However, because the vorticity center and the swirl center (as well as the void center) data were generally not collocated, the normalized vorticity profile was referenced to the vorticity center. The peak vorticity occurred at the

center ($\kappa = 0$) when $\psi = 15°$ (fig. 47). At subsequent wake ages ($\psi = 195°$ and 375°), the vorticity in the center decreased and the peaks progressively shifted toward the core diameter. A similar change in the distribution of vorticity was reported in an earlier fixed-wing experimental study using a vorticity meter (ref. 25). As discussed earlier, it is not known to what extent this characteristic might be due to potentially inaccurate data within the void region. Nevertheless, the fact that this radial shift in the vorticity peak has been observed while using other measurement techniques (vorticity meter and LDV) suggests that the PIV data are authentic and that the vortex was indeed becoming unstable.

The self-similar nature of the swirl velocity and the vorticity for the entire set of wake ages ($\psi = 0°$ to 390°) are shown in figure 48. The swirl velocity was made dimensionless by its value at the core radius (φ/φ_c), and the radius (measured from the swirl center) was made dimensionless by the core radius (ζ/ζ_c). Some data points for the dimensionless swirl, $\overline{\varphi}$, exceed 1.0 because the maximum swirl velocity, φ_c, was based on curve fits to φ *vs.* ζ at each wake age (figs. 15 – 39). The dimensionless form of a popular vortex model (ref. 21)

$$\overline{\varphi} = \frac{\Gamma_*}{\Gamma_c} \frac{\overline{\zeta}}{\left(1 + \overline{\zeta}^{2n}\right)^{1/n}} \tag{3}$$

has also been included in the plot. The best fit to the data occurred when $n = 3$ and $\Gamma_*/\Gamma_c = 1.26$. According to this model, the circulation around a contour placed at the core boundary, Γ_c, was about 79 percent of the total far-field (or large-radius) value, Γ_*. Note that at the core radius $\overline{\varphi} = \overline{\zeta} = 1$, so that equation (3) requires that $\Gamma_*/\Gamma_c = 2^{1/n} = 1.26$ when $n = 3$.

The self-similar distribution of accumulated vorticity can be found from the product of the local vorticity (ω_θ) and the incremental area over which it acts ($\Delta r \Delta z$), and then summed over regions defined by the radius from the vorticity center (κ). In principle, the result should be equivalent to the variation of circulation with radius, provided the swirl and vorticity centers are coincident. Within the core ($\kappa \leq \zeta_c$), the distribution of vorticity is quite similar and is well represented by the model, $\overline{\varphi\zeta}$. Beyond the core radius the accumulated vorticity asymptotically approaches a constant value and on average agrees with that predicted by the vortex model, which states that $\overline{\varphi\zeta} \rightarrow 1.26$ as $\overline{\zeta}$ becomes large.

The core-radius circulation, Γ_c, was observed to increase slightly with wake age (fig. 49). Because some vorticity was found to exist beyond the core radius at all wake ages, and because the core radius generally increased with wake age (fig. 49), it is probable that additional vorticity was gradually being gathered into the core. The total far-field vorticity appears to be fairly constant, $\Gamma_* = 1.42$ m^2/s. The growth in the size of the vortex core can be approximated by the following model (ref. 26, and further developed in ref. 24):

$$\zeta_c = (\zeta_{c0}^2 + 5\delta\nu\psi/\Omega)^{1/2} \tag{4}$$

where $\delta = 16$ provides the best fit to the present data (for laminar flow, $\delta = 1$). Data included from another experiment (ref. 24, based on LDV measurements) was reported to be best fit by the model when $\delta = 8$. It should be noted that δ strongly depends on the initial core size, ζ_{c0}, and that lower values of ζ_{c0} require lower values of δ. The results presented in reference 24, which are for a single-bladed rotor, show a similar range of core sizes and growth rate.

Based on an isolated vortex model (refs. 22, 27) that assumes a turbulence mixing length that is proportional to the vortex radius, the ratio of the core-radius to large-radius circulation should be fixed by the vortex Reynolds number, Γ_*/ν. However, the data for this test ($\Gamma_*/\nu \approx 1.2 \times 10^5$) fall above the curve and are, on average, aligned with a laminar value for Γ_c/Γ_* (fig. 49). This would imply that $\delta \approx 1$ rather than 16 as required for a good fit to the ζ_c *vs.* ψ data, and would suggest that either the models are imprecise or that the core radius is not as large as measured.

Just as the core-radius circulation was less than the large-radius circulation during the first revolution of the rotor, the large-radius circulation is expected to be less than the maximum bound circulation on the blade. Although the blade circulation was not measured in this test, a value can be approximated from blade-element momentum theory (ref. 28). For a blade with constant chord, the total thrust coefficient can be stated in terms of the dimensionless inflow, λ, as

$$C_T = \int_0^1 4\lambda^2 r dr \tag{5}$$

and the sectional value in terms of the local circulation, Γ_b, on the blade as

$$dC_T = \frac{\sigma\Gamma_b}{\Omega R c} r dr \tag{6}$$

From the above two equations it follows that the inflow velocity and the blade circulation (both are functions of r) are related by

$$\frac{\sigma\Gamma_b}{\Omega R c} = 4\lambda^2 \tag{7}$$

The local inflow velocity for hover can be stated as (ref. 28)

$$\lambda = \frac{\sigma C_{l\alpha}}{16}\left(\sqrt{1+\frac{32r\theta}{\sigma C_{l\alpha}}}-1\right) \tag{8}$$

where θ is the local blade angle. Because the climb rate in this test was insignificant, hover conditions are assumed to apply. The change in blade angle along the span for the rotor used in this test is shown in figure 50. If the blade angle, $\theta(r)$, is known, and if it is assumed that $C_{l\alpha} \approx 0.1$, the local inflow velocity predicted by equation (8) can be determined (fig. 50). However, in order to more easily perform the integration given in equation (5), simple analytical expressions for the inflow in the form of $\lambda = \lambda_0 r^n$ have been proposed (refs. 22, 28). The results for $n = 0$ (constant inflow), $n = 0.5$ (linear circulation), and $n = 1$ (linear inflow) are shown in figure 50. Although this power function has served well to illustrate various performance trends, the inflow used in the present analysis was

$$\lambda = \lambda_0\sqrt{\sin\frac{\pi}{2}r} \tag{9}$$

From equations (5), (7), and (9) the maximum bound circulation on the rotor blade is

$$\left(\frac{\Gamma_b}{\Omega R c}\right)_{max} = 2.47\frac{C_T}{\sigma} \tag{10}$$

Recalling that $C_T = 0.00657$ and $\sigma = 0.0691$, then equation (10) states that $(\Gamma_b)_{max} = 2.13$ m^2/s for this test. To summarize:

$$\frac{\Gamma_c}{\Gamma_*} = 0.79 \tag{11}$$

$$\frac{\Gamma_*}{\Gamma_{b\,max}} = 0.67 \tag{12}$$

implying that the core-radius circulation is only about 53 percent of the maximum bound circulation on the rotor blade.

CONCLUSIONS

1. The highest velocities occurred within the first 15° behind the rotor blade. The swirl and axial velocities reached 44 and 12 percent of the rotor tip speed, respectively.

2. The initial diameter of the vortex core was about 10 percent of the blade chord and more than doubled its size after one revolution of the rotor. The rate of growth followed a square-root function of wake age.

3. The boundary layer wake that was shed along the span of the rotor blade disappeared after $\psi = 30°$; however, two concentrated zones of oppositely directed axial flow were observed near the center of the vortex throughout the first rotor revolution.

4. The void, vorticity (or centroid of vorticity), and the swirl centers occurred at distinct locations, but were never separated by more than 26 percent of the vortex diameter.

5. The axially directed velocity profile, relative to the convection velocity of the void center, was asymmetric because of the influence of the rotor downwash. The vortex also appeared to have an elliptical shape that rotated as the wake aged.

6. The peak vorticity occurred near the center of the vortex during the early development of the trailing vortex, and then progressively shifted toward the core diameter. It is presently unknown to what extent this result is due to weakly defined characteristics within the void region.

7. The magnitude of the radial distribution of the circulation rapidly increased until reaching a point just beyond the core radius, after which the rate of growth decreased significantly. The core-radius circulation increased slightly with wake age, but the large-radius circulation appeared to remain relatively constant.

8. The radial distributions of swirl velocity and vorticity exhibit self-similar behaviors, especially within the core. According to vortex models that approximate the measured data, the core-radius circulation was about 79 percent of the large-radius circulation, and the large-radius circulation was about 67 percent of the maximum bound circulation that was calculated for the rotor blade. On average, about 53 percent of the maximum bound circulation resides within the vortex core during the first revolution of the rotor.

REFERENCES

[1] Tung, C.; Yu, Y. H.; and Low, S. L.: Aerodynamic Aspects of Blade-Vortex Interaction (BVI). AIAA 96-2010, 27th AIAA Fluid Dynamics Conference, New Orleans, La., 1996.

[2] Wachspress, D. A.; and Quackenbush, T. R.: BVI Noise Prediction Using a Comprehensive Rotorcraft Analysis. 57th Annual Forum of the American Helicopter Soc., Washington, D.C., 2001.

[3] Strawn, R. C.; and Djomehri, M. J.: Computational Modeling of Hovering Rotor and Wake Aerodynamics. 57th Annual Forum of the

American Helicopter Soc., Washington, D.C., 2001.

[4] Hu, G.; Grossman, B.; and Steinhoff, J.: A Numerical Method for Vortex Confinement in Compressible Flow. AIAA 2000-0281, 38th Aerospace Sciences Meeting & Exhibit, Reno, Nev., 2000.

[5] Tung, C.; Pucci, S. L.; Caradonna, F. X.; and Morse, H. A.: The Structure of Trailing Vortices Generated by Model Rotor Blades. *Vertica*, vol. 7, no. 1, 1983.

[6] Komerath, N. M.; Thompson, T. L.; Kwon, O. J.; and Gray, R. B.: Velocity Field of a Lifting Rotor Blade in Hover. *J. Aircraft*, vol. 25, no. 3, 1988.

[7] Bagai, A.; and Leishman, J. G.: Flow Visualization of Compressible Vortex Structures Using Density Gradient Techniques. *Experiments in Fluids*, vol. 15, no. 6, 1993.

[8] Leishman, J. G.; Baker, A.; and Coyne, A.: Measurements of Rotor Tip Vortices Using Three-Component Laser Doppler Velocimetry. *J. American Helicopter Soc.*, vol. 41, no. 4, 1996.

[9] Han, Y. O.; Leishman, J. G.; and Coyne, A. J.: On the Turbulent Structure of a Tip Vortex Generated by a Rotor. 52th Annual Forum of the American Helicopter Soc., Washington, D.C., 1996.

[10] Boutier, A.; Lefevre, J.; and Micheli, F.: Analysis of Helicopter Blade Vortex Structure by Laser Velocimetry. *Experiments in Fluids*, vol. 21, no. 1, 1996.

[11] Seelhorst, U.; Raffel, M.; Willert, C.; Vollmers, H.; Butefisch, K. A.; and Kompenhans, J.: Comparison of Vortical Structures of a Helicopter Rotor Model Measured by LDV and PIV. 22nd European Rotorcraft Forum, Brighton, UK, 1996.

[12] McAlister, K. W.: Measurements in the Near Wake of a Hovering Rotor. AIAA 96-1958, 27th AIAA Fluid Dynamics Conference, New Orleans, La., 1996.

[13] Leishman, J. G.: Measurements of the Aperiodic Wake of a Hovering Rotor. *Experiments in Fluids*, vol. 25, no. 4, 1998.

[14] Bhagwat, M. J.; and Leishman, J. G.: On the Relationship between Blade Circulation and Tip Vortex Characteristics. 54th Annual Forum of the American Helicopter Soc., Washington, D.C., 1998.

[15] Martin, P. B.; Leishman, J. G.; Pugliese, G. J.; and Anderson, S. L.: Stereoscopic PIV Measurements in the Wake of a Hovering Rotor. 56th Annual Forum of the American Helicopter Soc., Virginia Beach, Va., 2000.

[16] Heineck, J. T.; Yamauchi, G. K.; Wadcock, A. J.; Lourenco, L.; and Abrego, A. I.: Application of Three-Component PIV to a Hovering Rotor Wake. 56th Annual Forum of the American Helicopter Soc., Virginia Beach, Va., 2000.

[17] McAlister, K. W.; Tung, C.; and Heineck, J. T.: Forced Diffusion of Trailing Vorticity from a Hovering Rotor. 57th Annual Forum of the American Helicopter Soc., Washington, D.C., 2001.

[18] McAlister, K. W.; Huang, S. S.; and Abrego, A. I.: A Model Rotor in Axial Flight. NASA TM–2001-210925, 2001.

[19] Spalart, P. R.: Airplane Trailing Vortices. *Annual Review of Fluid Mechanics*, vol. 30, 1998.

[20] Spalart, P.: Wake-Vortex Physics: The Great Controversies. NASA/CP-97-206235, Proceedings of the NASA First Wake Vortex Dynamic Spacing Workshop, 1997.

[21] Vatistas, G. H.; and Kozel, V.: A Simpler Model for Concentrated Vortices. *Experiments in Fluids*, vol. 11, no. 1, 1991.

[22] Martin, P. B.: Measurements of the Trailing Vortex Formation, Structure, and Evolution in the Wake of a Hovering Rotor. Ph.D. Dissertation, University of Maryland, 2001.

[23] Yamauchi, G. K.; Burley, C. L.; Mercker, E.; Pengel, K.; and JanakiRam, R.: Flow Measurements of an Isolated Model Tilt Rotor. 55th Annual Forum of the American Helicopter Soc., Montreal, Canada, 1999.

[24] Martin, P. B.; Pugliese, G. J.; and Leishman, J. G.: High Resolution Trailing Vortex Measurements in the Wake of a Hovering Rotor. 57th Annual Forum of the American Helicopter Soc., Washington, D.C., 2001.

[25] McCormick, B. W.; Tangler, J. L.; and Sherrieb, H. E.: Structure of Trailing Vortices. *J. Aircraft*, vol. 5, no. 3, 1968.

[26] Squire, H. B.: The Growth of a Vortex in Turbulent Flow. *The Aeronaut. Quart.*, vol. 16, no. 3, 1965.

[27] Iversen, J. D.: Correlation of Turbulent Trailing Vortex Decay Data. *J. Aircraft*, vol. 13, no. 5, 1976.

[28] Leishman, J. G.: *Principles of Helicopter Aerodynamics*. Cambridge Univ. Press, New York, 2000.

Table 3: Locations related to vortex

Wake age (deg)	Vorticity center r (mm)	Vorticity center z (mm)	Swirl center r (mm)	Swirl center z (mm)	Void center r (mm)	Void center z (mm)	Core radius (mm)	Void radius (mm)
0	945.78	2.89	946.11	1.93	946.00	3.00	5.00	0.71
15	934.78	−1.01	934.25	−1.31	934.70	−0.80	5.25	2.21
30	922.28	−7.88	922.99	−8.66	922.10	−8.80	5.00	2.85
45	909.53	−16.08	909.51	−14.88	910.00	−16.00	6.75	3.42
60	899.23	−26.00	899.35	−25.80	899.30	−26.70	6.75	3.74
75	888.40	−35.37	888.98	−34.31	888.40	−35.20	6.75	4.42
90	877.85	−44.60	878.04	−45.51	878.20	−45.20	7.50	5.04
105	868.99	−54.56	867.06	−54.17	869.00	−55.20	7.75	5.44
120	858.57	−64.35	858.66	−63.02	858.50	−64.50	8.50	5.55
135	850.34	−76.28	851.04	−73.69	850.00	−75.70	8.50	5.84
150	842.34	−83.49	839.95	−84.16	842.20	−85.40	10.50	5.94
180	829.99	−112.12	828.45	−112.83	830.60	−111.80	8.75	6.71
195	820.94	−130.12	820.29	−130.54	823.60	−131.10	8.75	7.08
210	820.87	−148.14	819.50	−146.08	821.10	−149.40	9.51	6.80
225	814.53	−165.86	812.56	−166.17	816.60	−166.00	8.75	6.82
240	810.73	−185.65	808.70	−183.76	812.70	−185.30	9.99	6.62
255	809.76	−200.91	808.47	−201.46	810.50	−202.00	10.24	7.49
270	810.10	−218.07	807.03	−217.92	810.70	−217.60	9.75	6.51
285	804.78	−231.66	801.58	−231.76	804.50	−232.60	10.00	6.28
300	802.36	−246.28	800.52	−245.89	803.10	−247.00	9.75	6.57
315	802.14	−262.10	800.28	−261.70	802.40	−263.10	9.75	6.72
328	801.18	−277.29	803.30	−276.32	801.10	−277.00	10.00	7.04
344	794.13	−293.91	791.73	−295.04	794.50	−293.60	10.50	6.76
375	795.78	−312.19	796.70	−309.02	795.50	−311.90	11.00	7.11
390	798.17	−328.52	797.79	−325.25	798.90	−329.10	11.25	7.14

Table 4: Vortex convection and shape

Wake age (deg)	Vortex convection u_c (m/s)	w_c (m/s)	Max swirl velocity (m/s)	Velocity peak separation d_h (mm)	d_v (mm)
0	−3.43	−3.03	30.77	10.77	9.07
15	−3.43	−3.04	35.36	9.58	11.15
30	−3.41	−3.07	32.24	10.93	11.02
45	−3.37	−3.14	24.88	13.64	12.88
60	−3.24	−3.31	25.86	13.51	14.55
75	−3.23	−3.39	27.39	13.68	12.75
90	−3.12	−3.57	24.59	13.65	14.58
105	−2.99	−3.79	23.26	13.67	14.56
120	−2.84	−4.04	20.29	13.49	18.30
135	−2.66	−4.30	16.62	14.91	18.36
150	−2.48	−4.57	17.07	16.26	18.19
180	−2.09	−5.07	20.78	17.61	14.46
195	−1.89	−5.28	17.50	19.03	18.14
210	−1.70	−5.43	17.94	18.04	17.81
225	−1.52	−5.53	17.52	17.99	15.68
240	−1.35	−5.58	15.32	19.37	17.65
255	−1.20	−5.58	17.82	19.38	19.71
270	−1.06	−5.53	17.27	19.02	18.26
285	−0.95	−5.45	15.94	18.99	16.44
300	−0.85	−5.35	19.57	18.97	18.32
315	−0.77	−5.25	18.20	19.04	18.10
328	−0.72	−5.17	17.71	19.07	18.26
344	−0.68	−5.08	17.84	19.02	18.29
375	−0.64	−4.99	16.35	18.96	21.74
390	−0.64	−4.99	15.63	19.11	21.82

Table 5: Vorticity and velocity extrema

Wake age (deg)	Vorticity normal to measurement plane max (1/s)	min (1/s)	Velocity within measurement plane max (m/s)	min (m/s)	Velocity normal to measurement plane max (m/s)	min (m/s)
0	20463.3	−2484.1	36.32	1.08	4.79	−10.78
15	22942.8	−994.0	38.76	1.21	2.62	−9.40
30	21014.8	−1290.1	35.08	1.54	1.83	−9.25
45	11374.9	−1198.1	26.59	0.23	2.33	−7.61
60	11808.0	−1055.6	26.67	0.02	2.79	−7.16
75	11929.1	−1043.4	29.03	0.14	2.71	−6.72
90	10505.9	−918.7	26.52	0.05	4.57	−6.61
105	9416.3	−1028.0	25.78	0.05	4.49	−6.56
120	7657.5	−1050.3	23.93	0.03	4.69	−6.55
135	5812.4	−1172.7	22.56	0.20	5.03	−6.96
150	6990.6	−1288.0	25.69	0.85	4.55	−9.30
180	8575.8	−1143.9	24.23	1.37	3.31	−5.31
195	8755.1	−1814.7	23.55	0.72	3.52	−6.09
210	8154.6	−900.5	23.14	0.61	3.48	−5.76
225	7746.3	−1147.3	22.40	0.44	3.26	−4.50
240	6852.9	−1623.4	19.61	0.24	3.46	−4.41
255	7020.4	−724.5	20.62	0.76	4.19	−5.36
270	7006.7	−870.7	22.13	0.27	2.77	−4.82
285	6732.1	−1318.6	19.52	0.06	2.40	−4.43
300	7062.0	−706.5	22.23	1.37	2.11	−5.33
315	6382.8	−773.3	19.93	1.20	2.35	−3.68
328	6532.7	−788.4	21.20	0.90	2.79	−4.44
344	6841.8	−859.0	20.49	0.38	1.72	−9.15
375	5851.2	−492.8	20.95	0.73	2.63	−7.30
390	5977.2	−734.8	21.39	0.05	4.32	−7.26

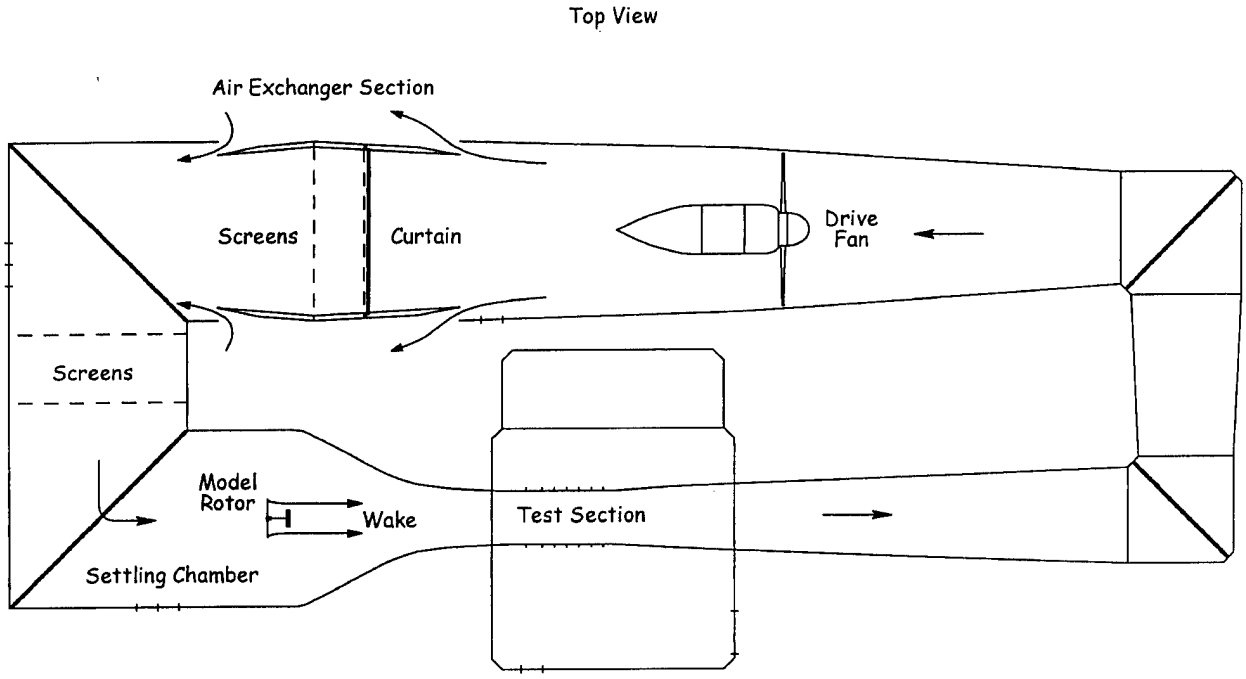

Figure 1: The 7- by 10-Foot Subsonic Wind Tunnel flow circuit.

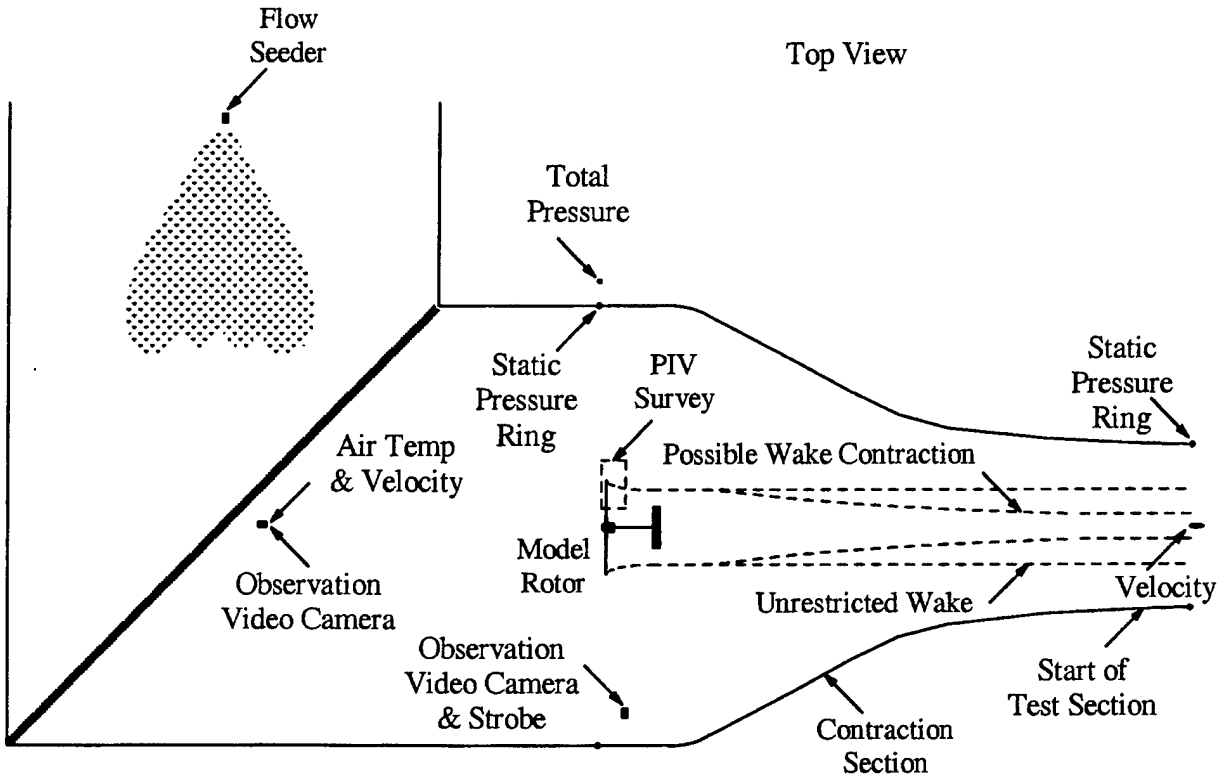

Figure 2: Instrument setup in settling chamber of 7- by 10-Foot Subsonic Wind Tunnel.

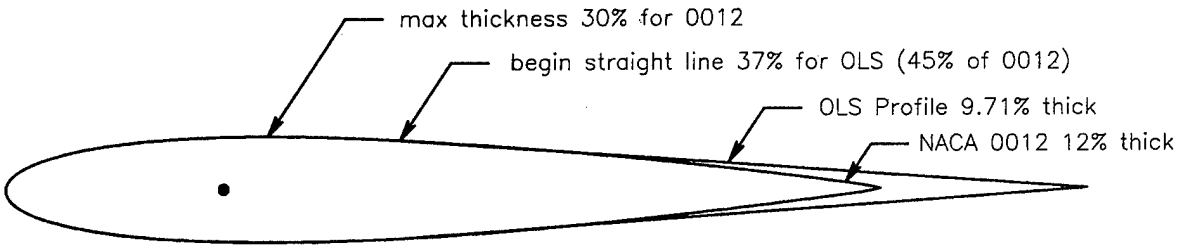

Figure 3: OLS blade profile.

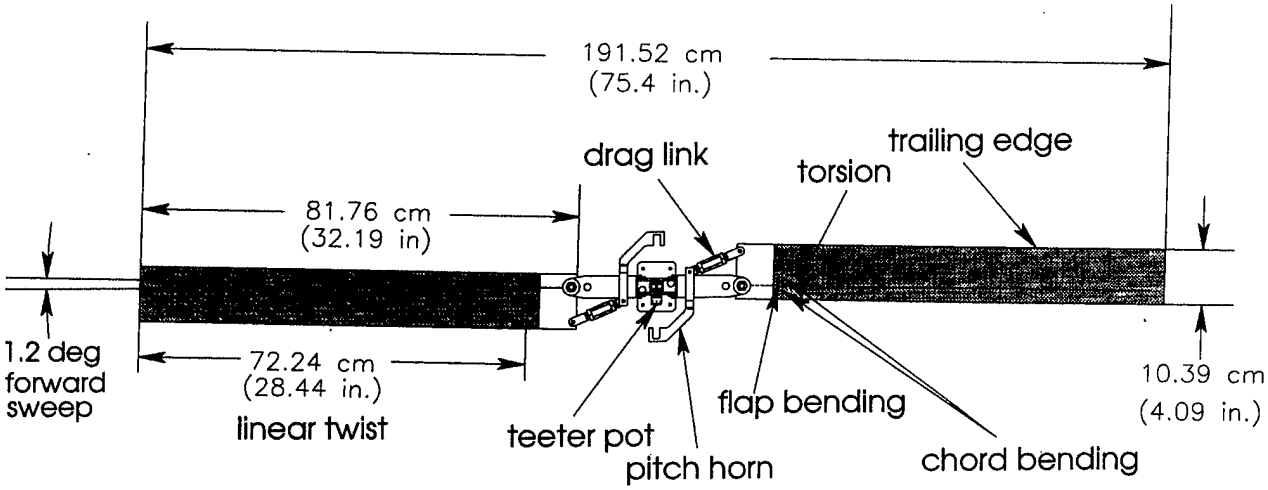

Figure 4: OLS model rotor head.

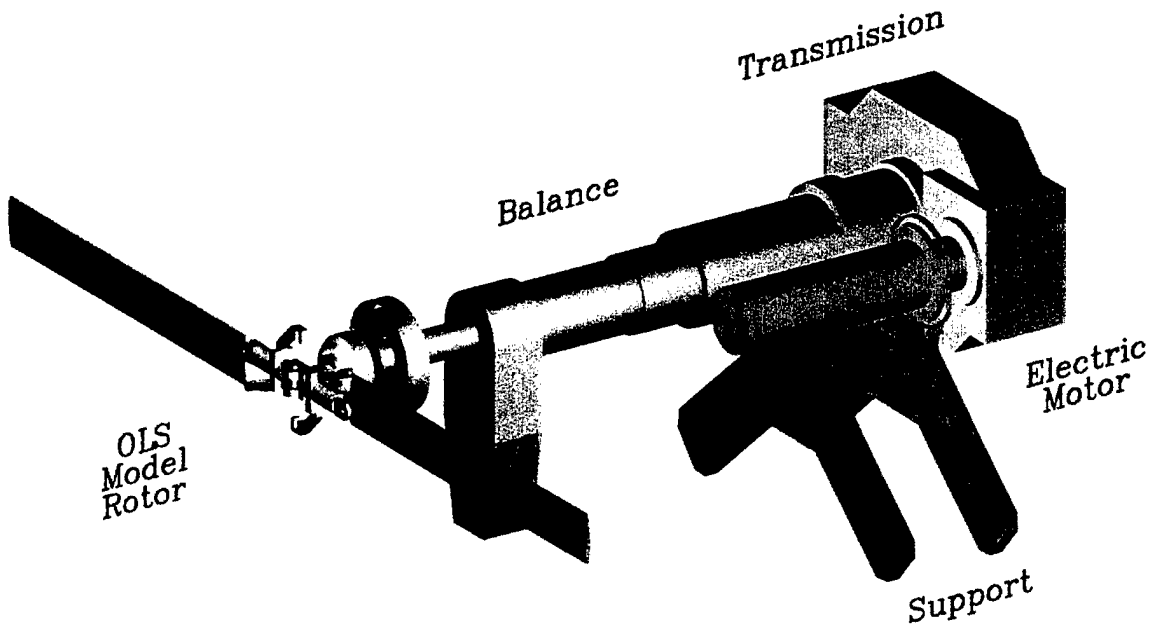

Figure 5: Model rotor assembly and support structure.

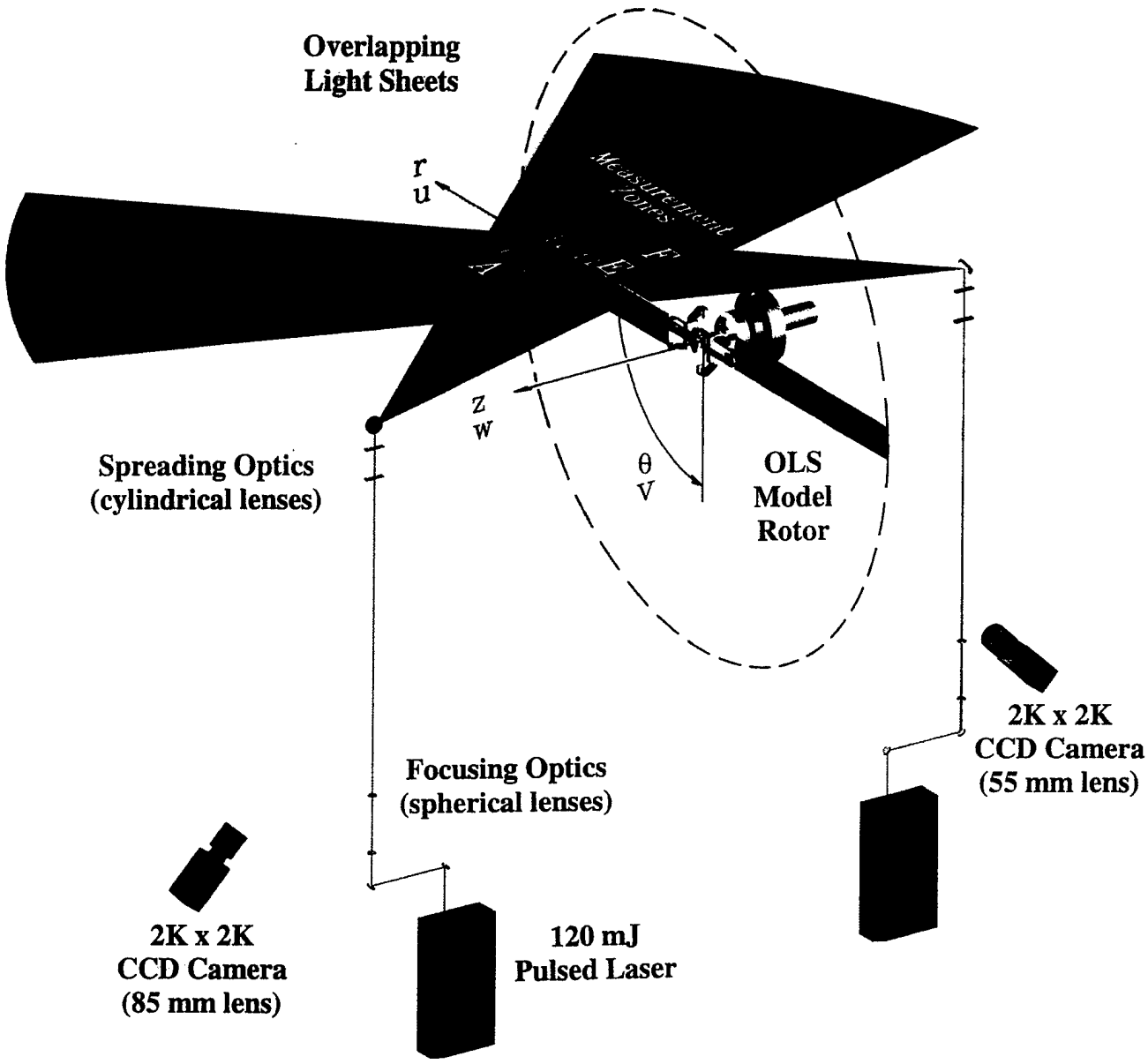

Figure 6: Particle imaging system layout (light sheets are horizontal).

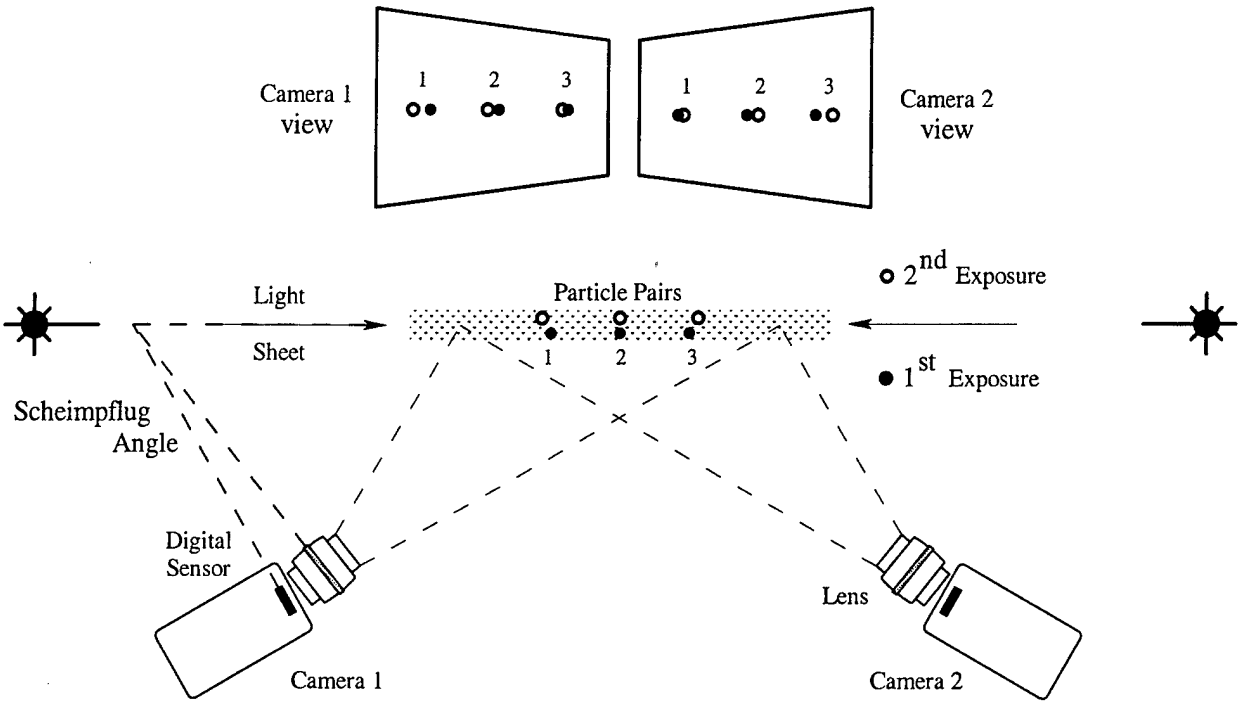

Figure 7: Perspective effect of particle displacement with stereoscopic PIV.

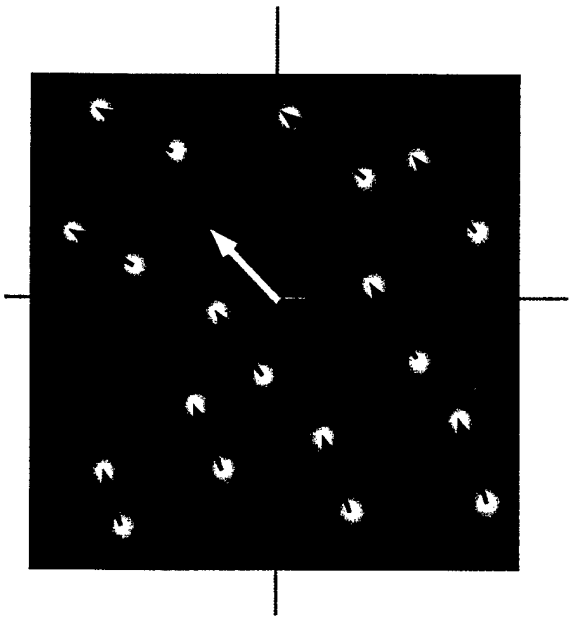

Figure 8: A single interrogation area in which ten particle displacements are registered on a 22- by 22-pixel CCD grid.

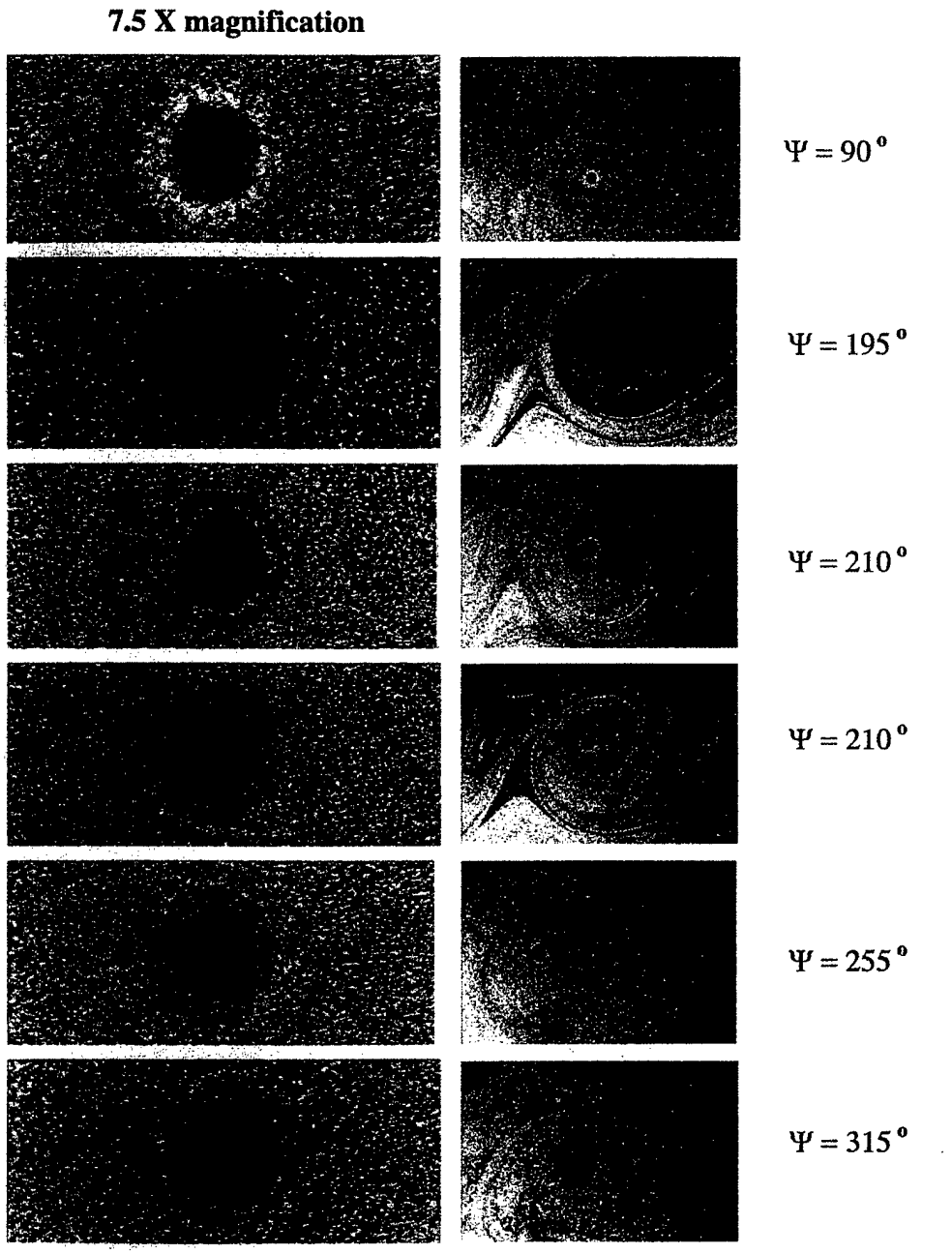

Figure 9: Particle distributions often observed around apparent vortex voids when flow is not uniformly seeded (camera view; images not dewarped).

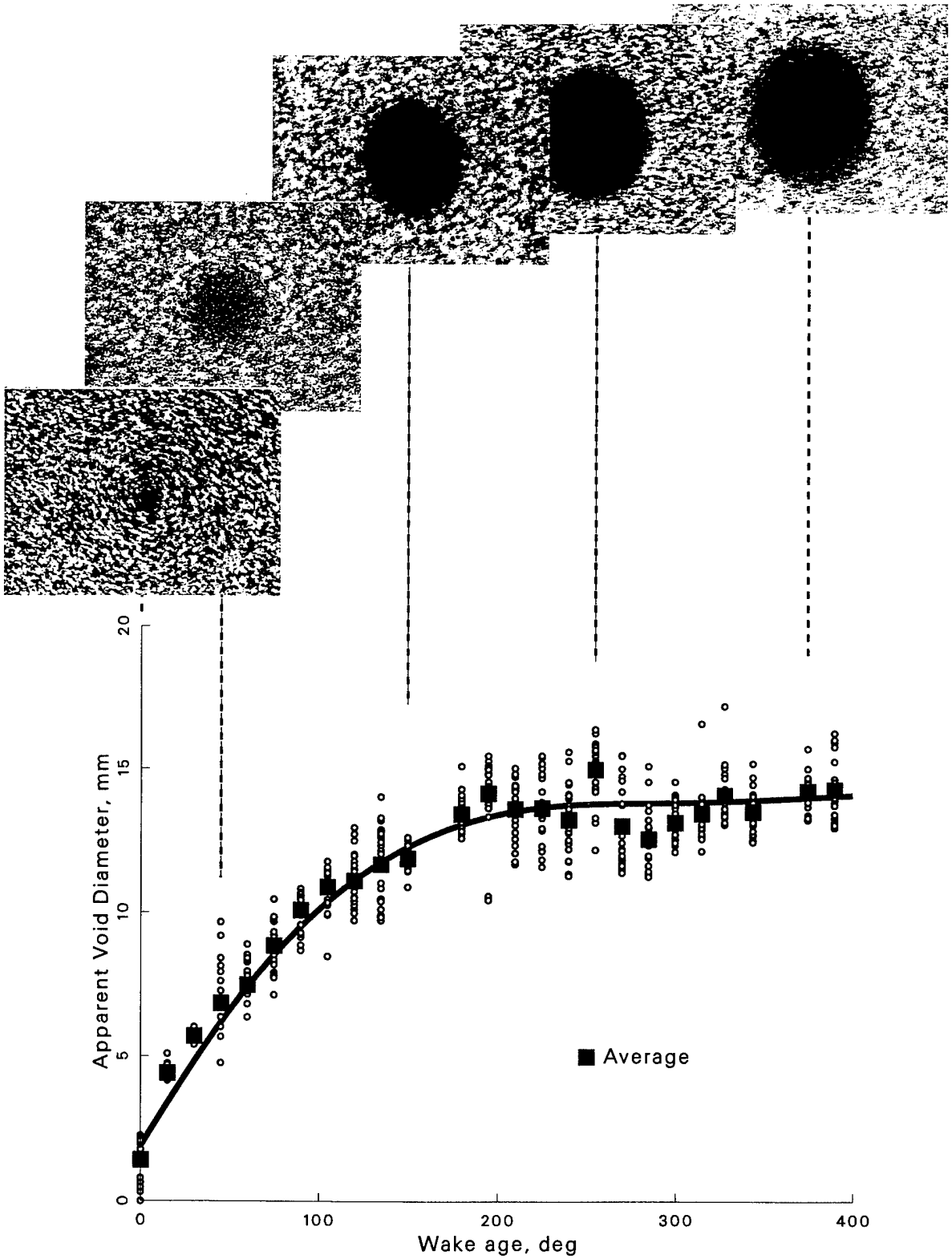

Figure 10: Diameter of apparent vortex voids and images typically observed at different wake ages.

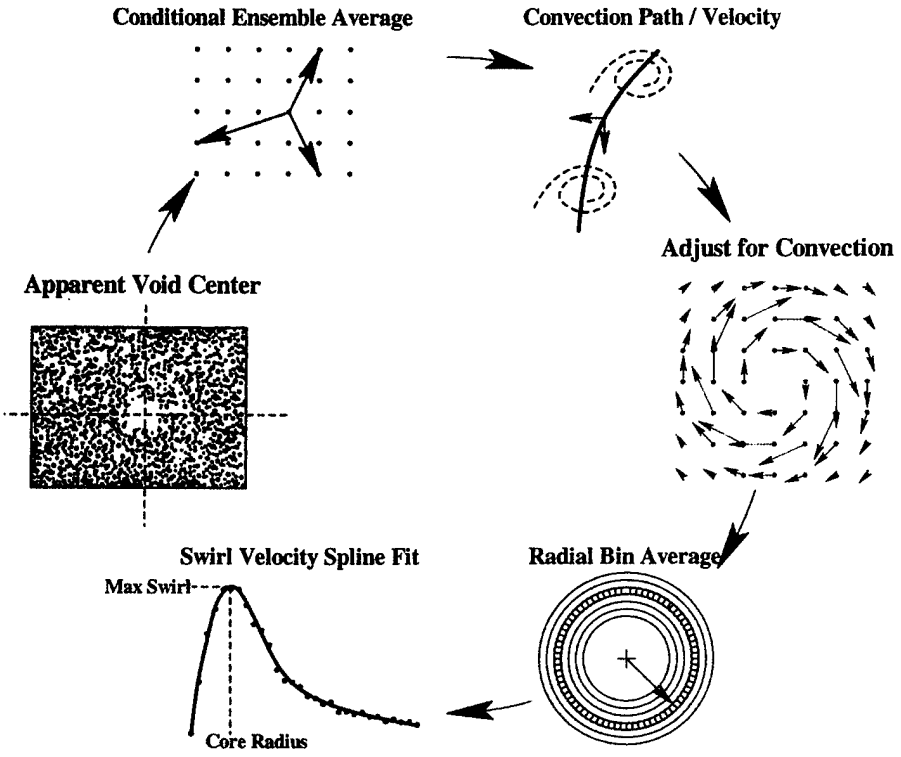

Figure 11: Sequence for extracting vortex characteristics.

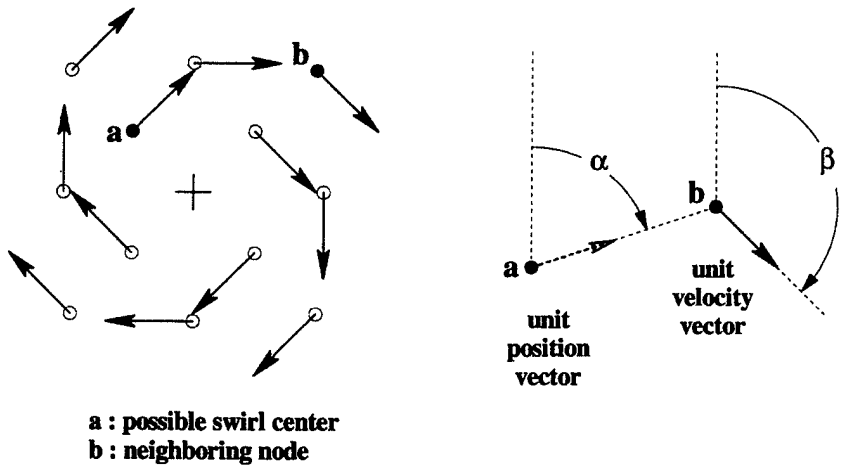

Figure 12: Angles used in search for center of swirl.

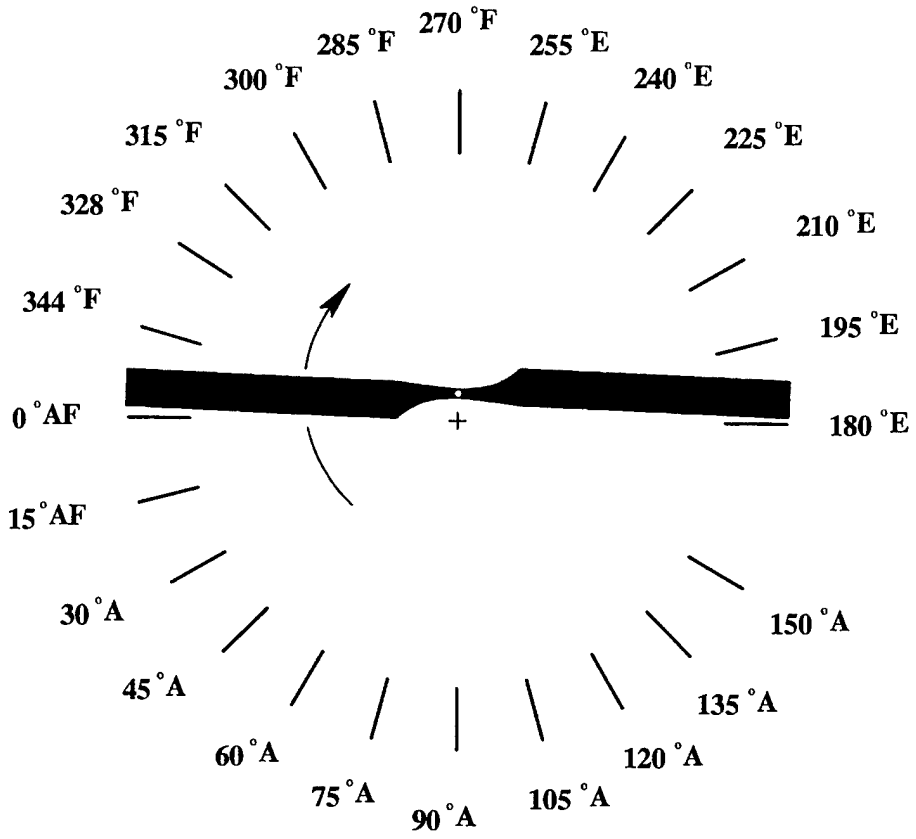

Figure 13: Wake ages at which PIV data were recorded.

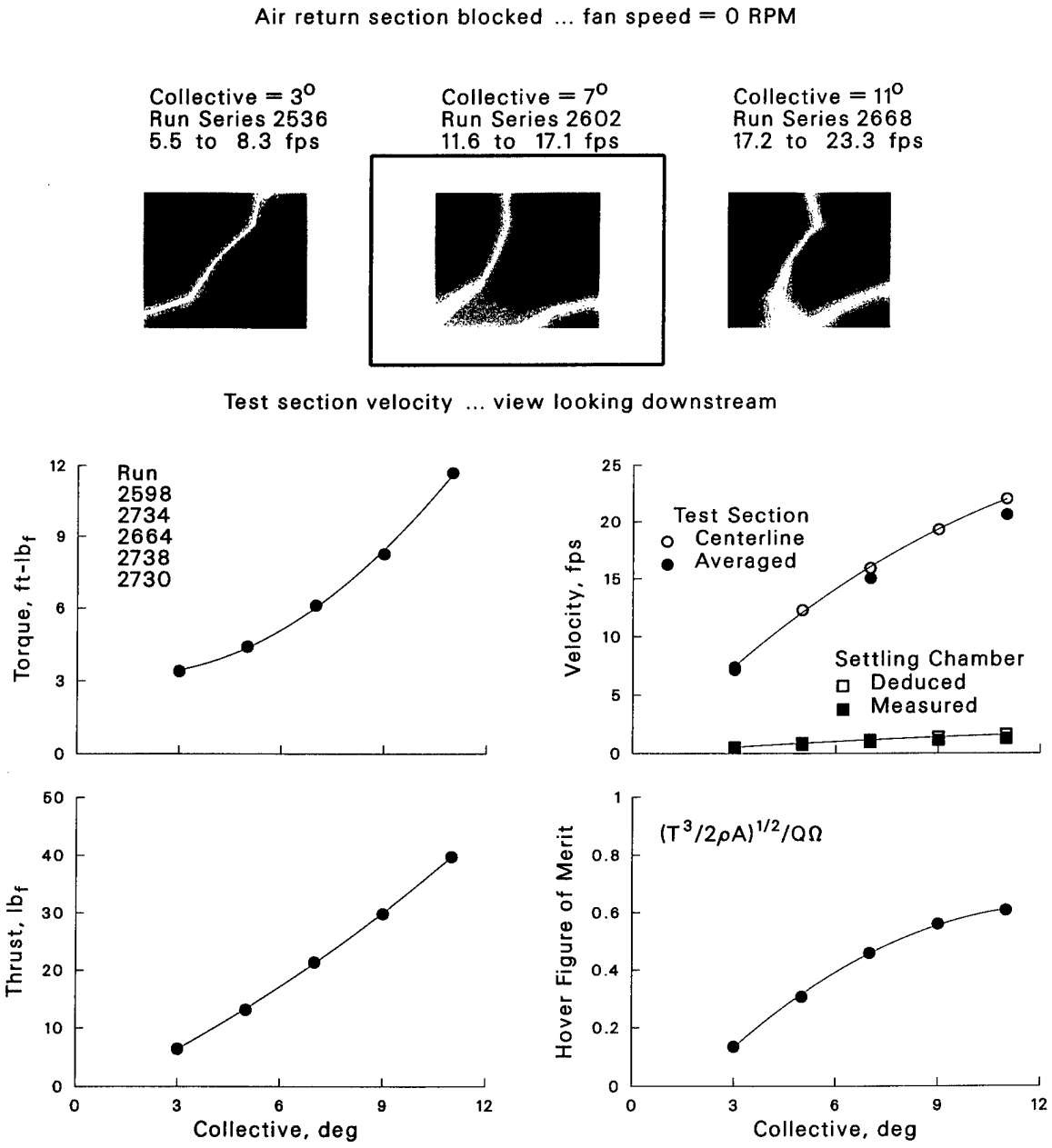

Figure 14: Rotor loads and tunnel velocities with return flow blocked (ref. 8).

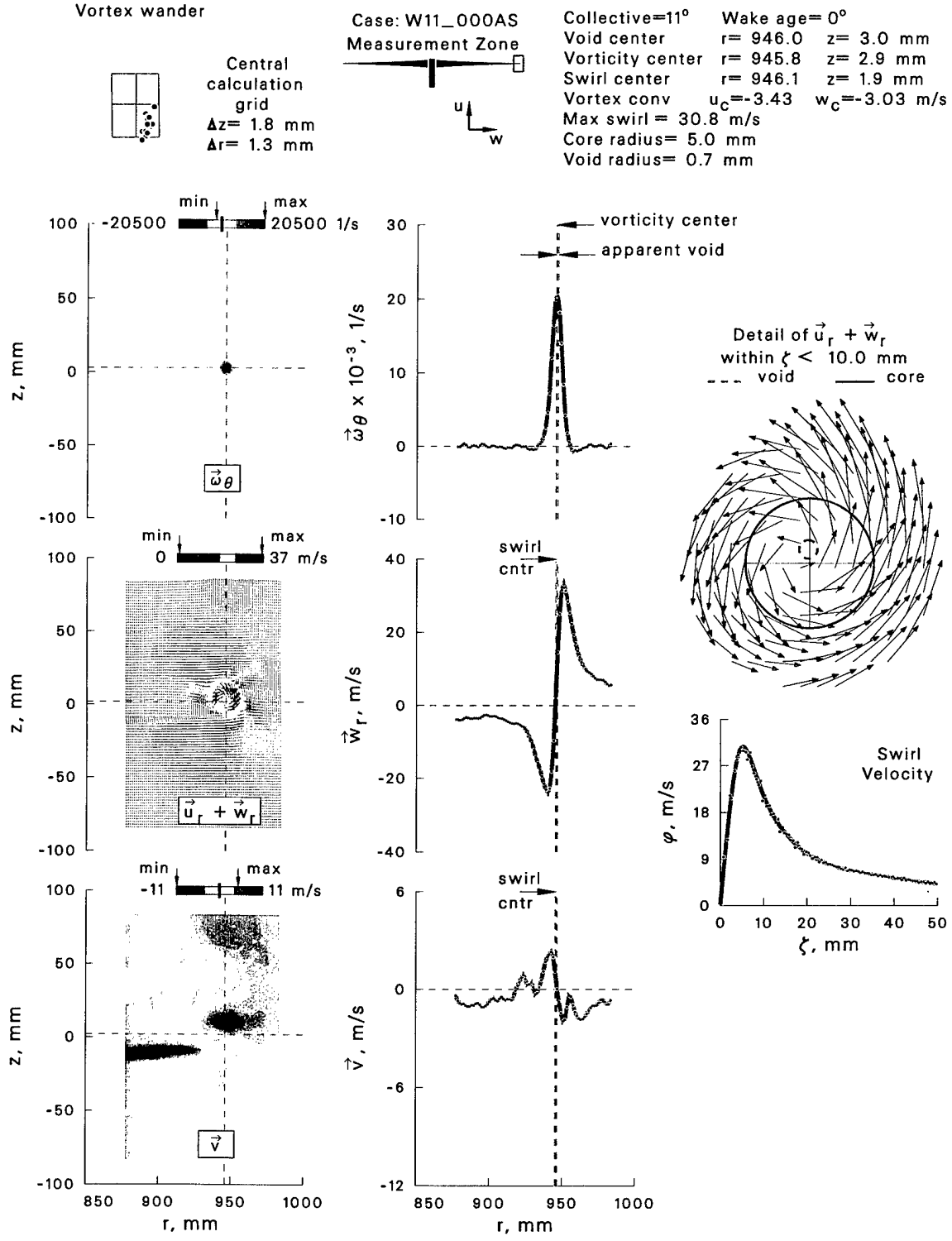

Figure 15: Velocity and vorticity characteristics with reference to the center of swirl at $\psi = 0°$.

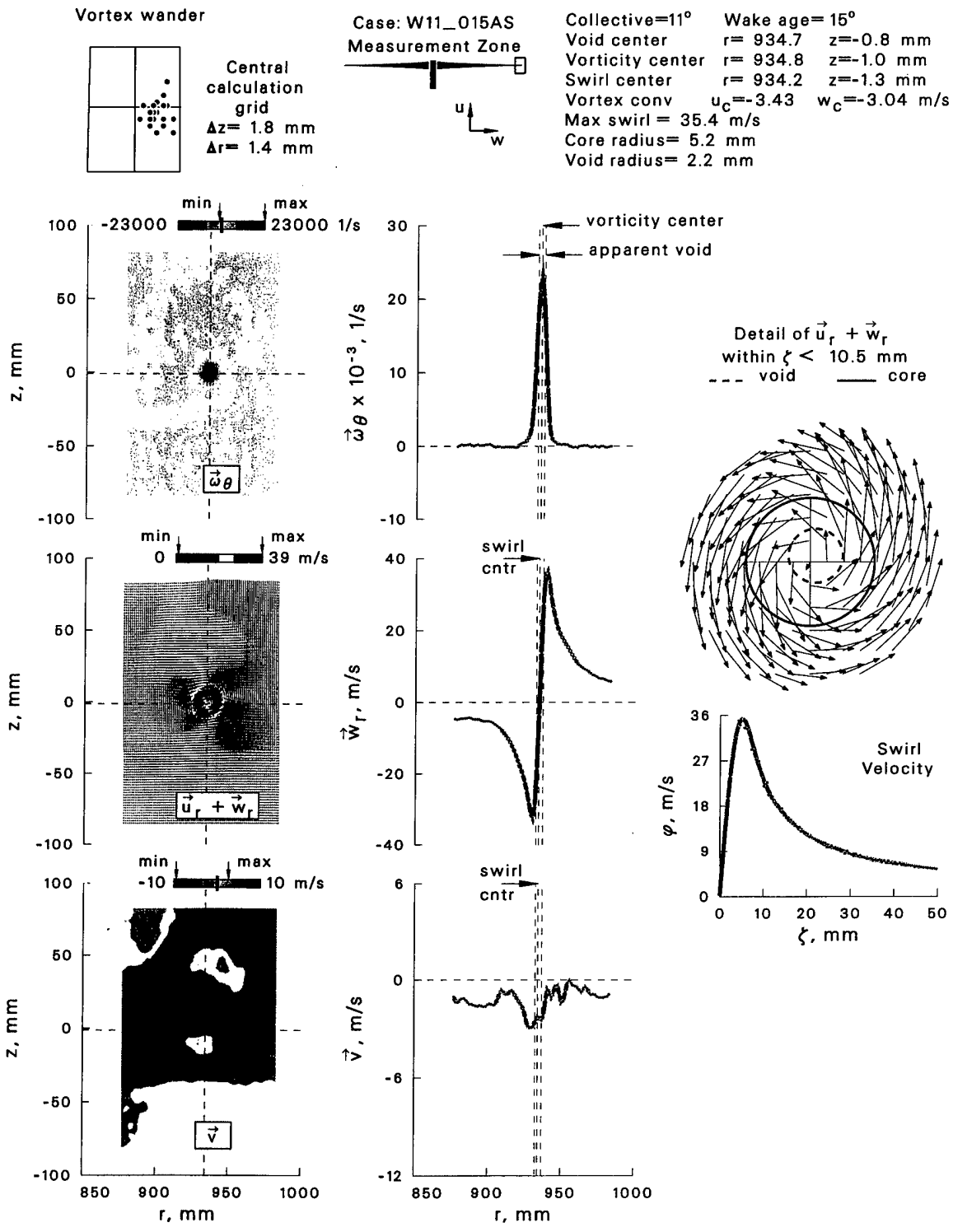

Figure 16: Velocity and vorticity characteristics with reference to the center of swirl at $\psi = 15°$.

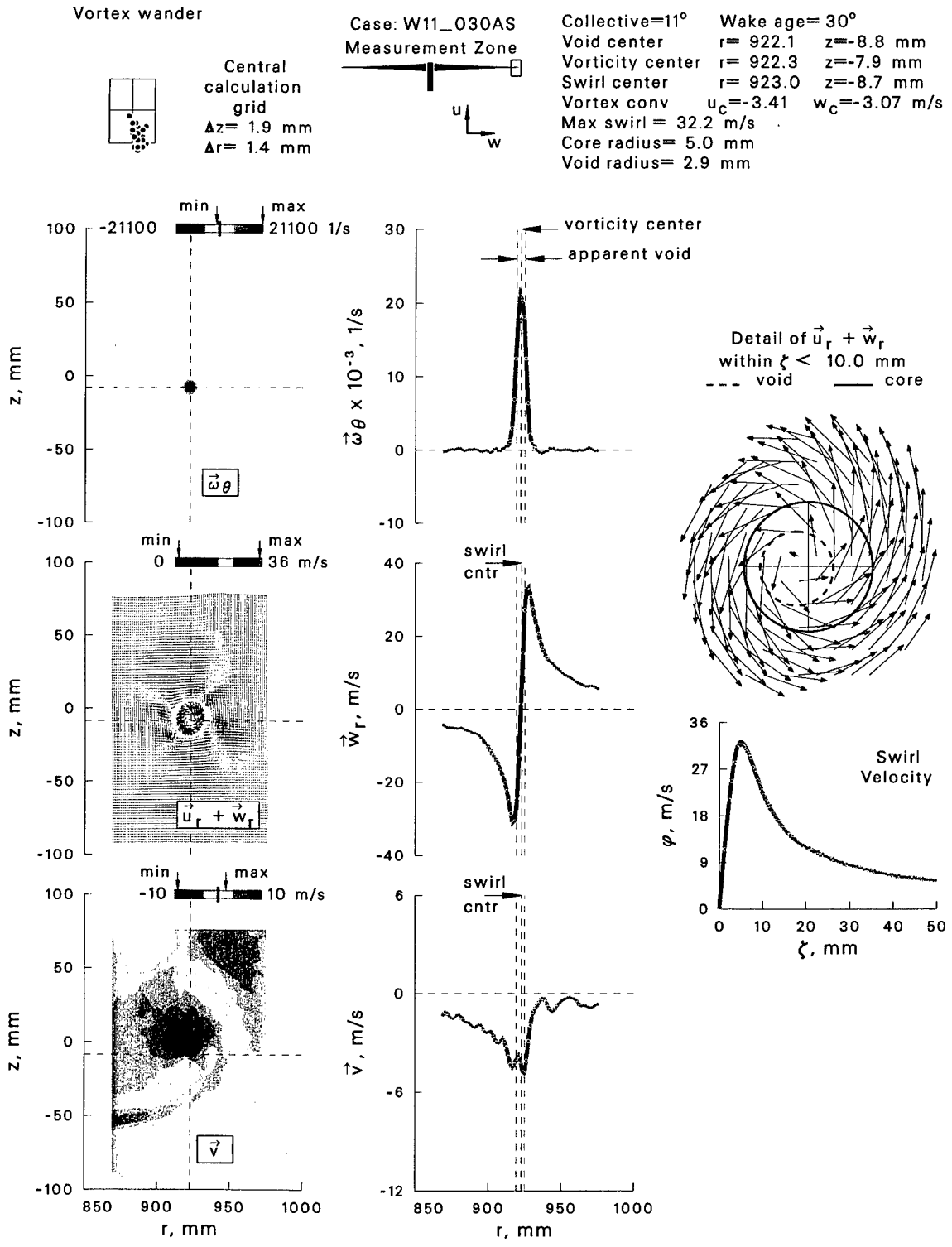

Figure 17: Velocity and vorticity characteristics with reference to the center of swirl at $\psi = 30°$.

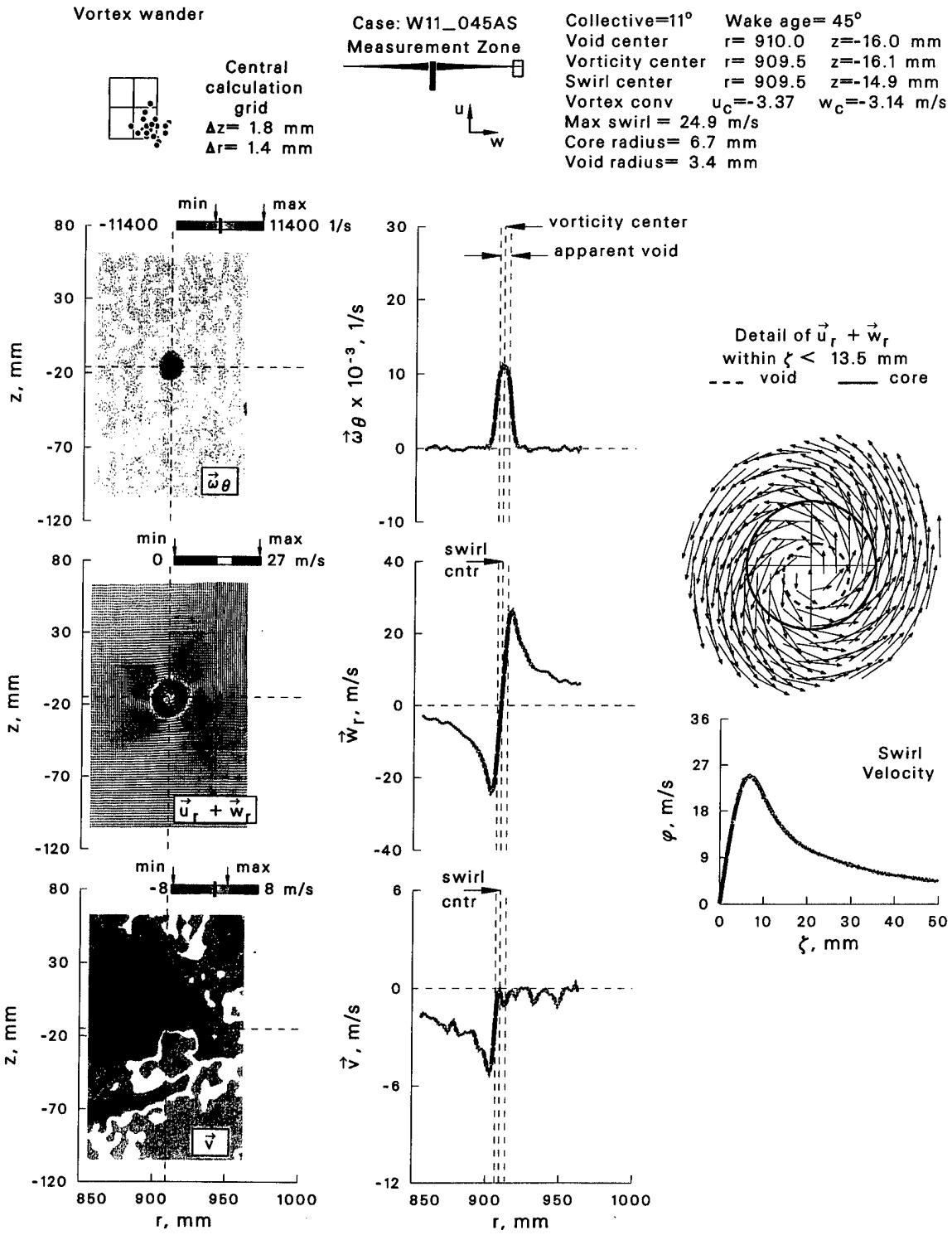

Figure 18: Velocity and vorticity characteristics with reference to the center of swirl at $\psi = 45°$.

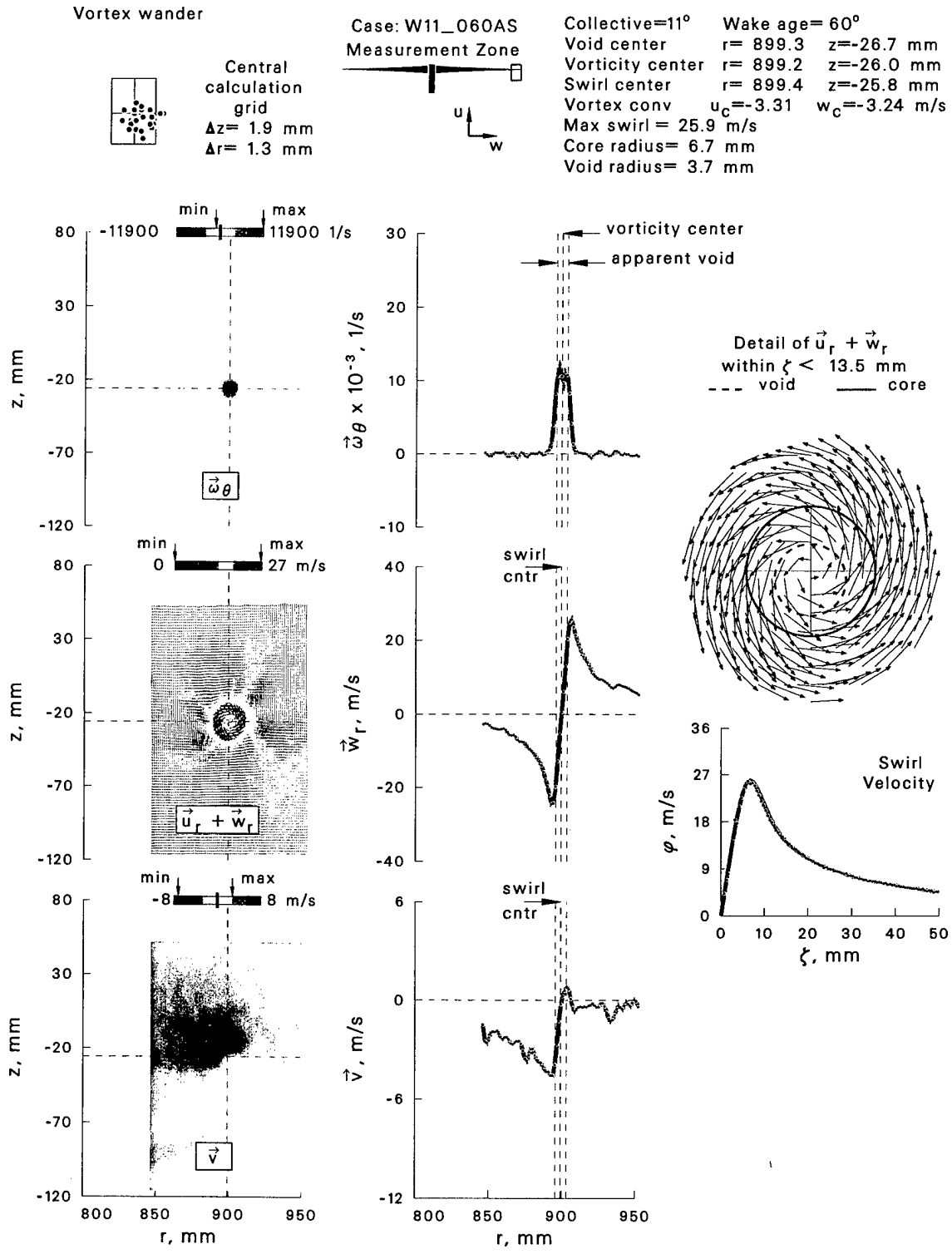

Figure 19: Velocity and vorticity characteristics with reference to the center of swirl at $\psi = 60°$.

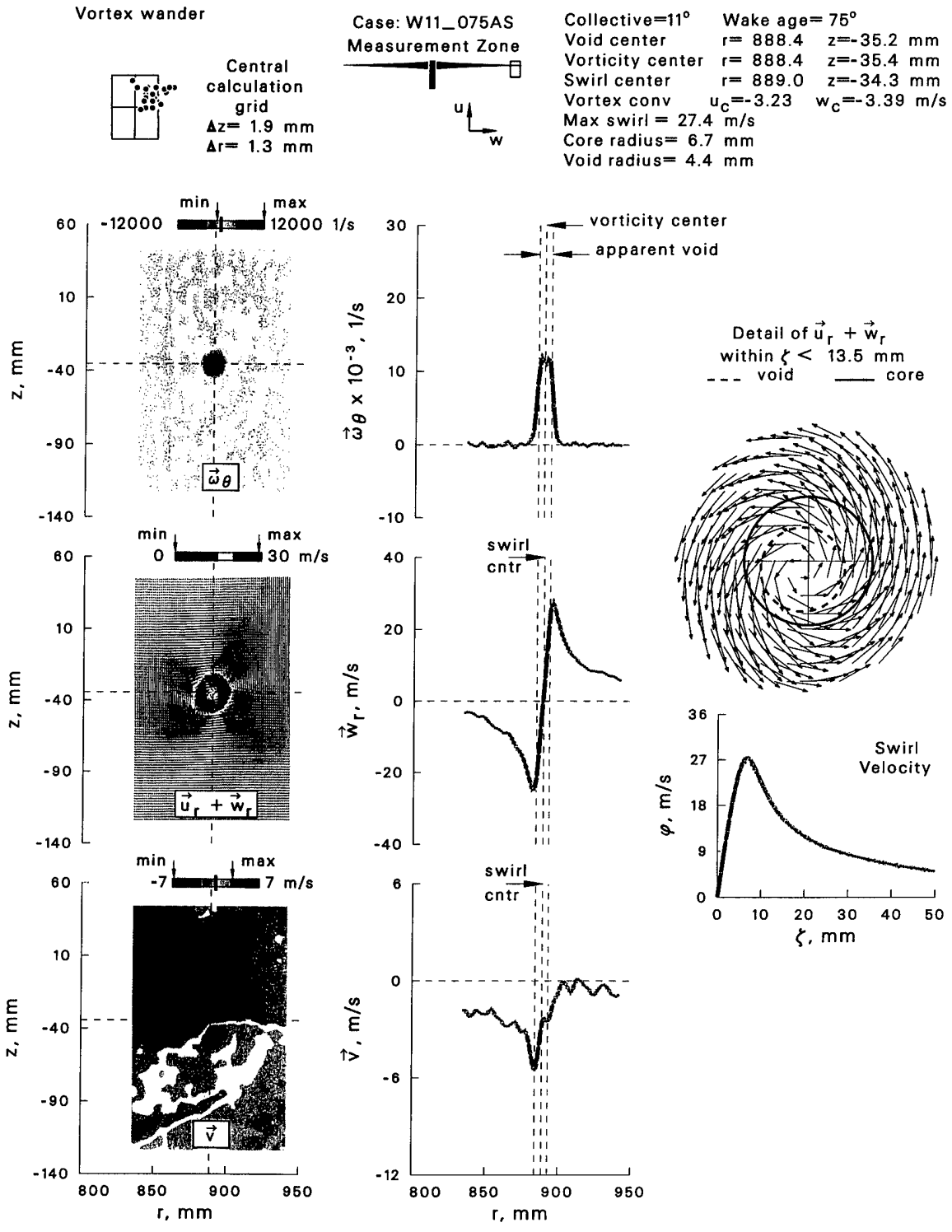

Figure 20: Velocity and vorticity characteristics with reference to the center of swirl at $\psi = 75°$.

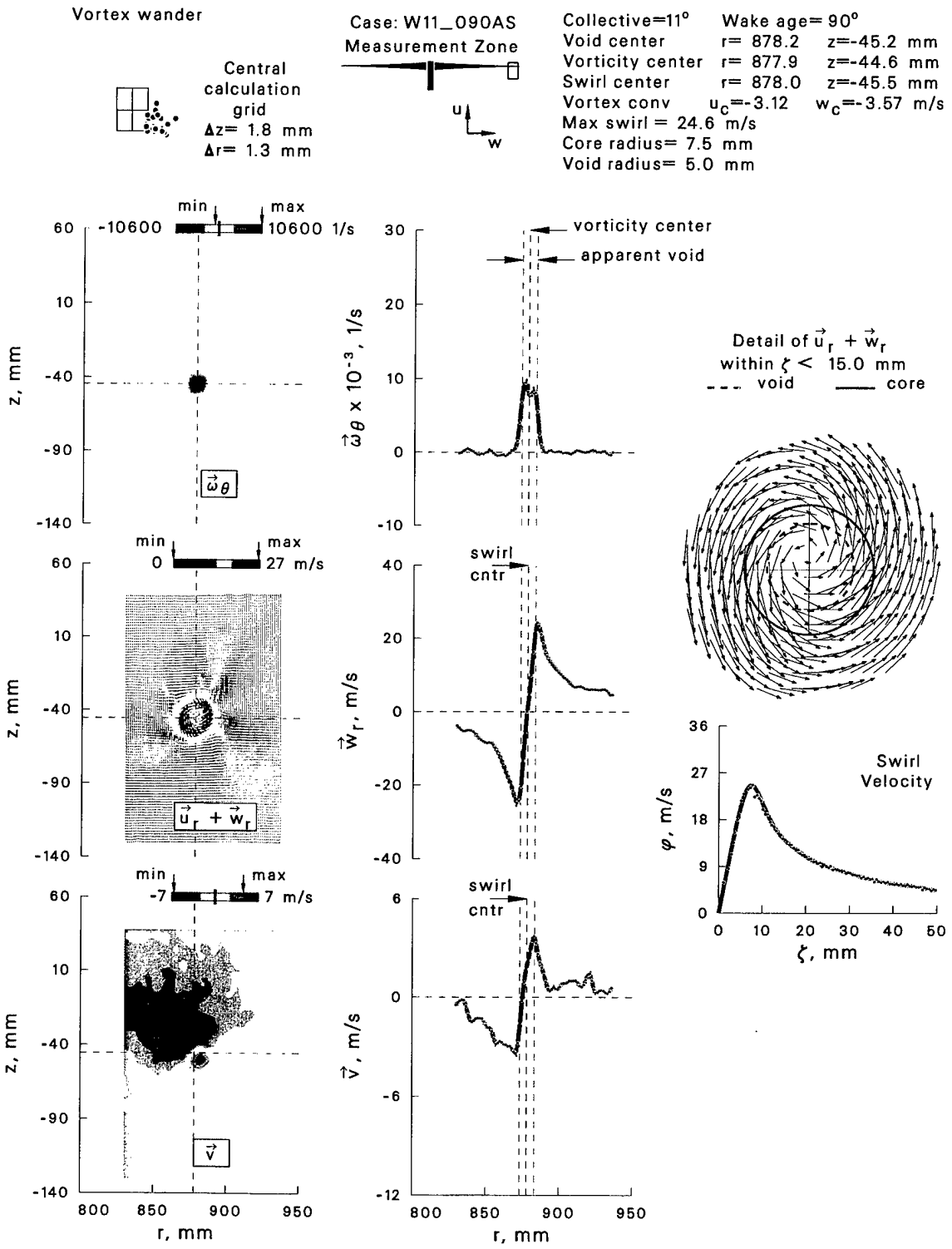

Figure 21: Velocity and vorticity characteristics with reference to the center of swirl at $\psi = 90°$.

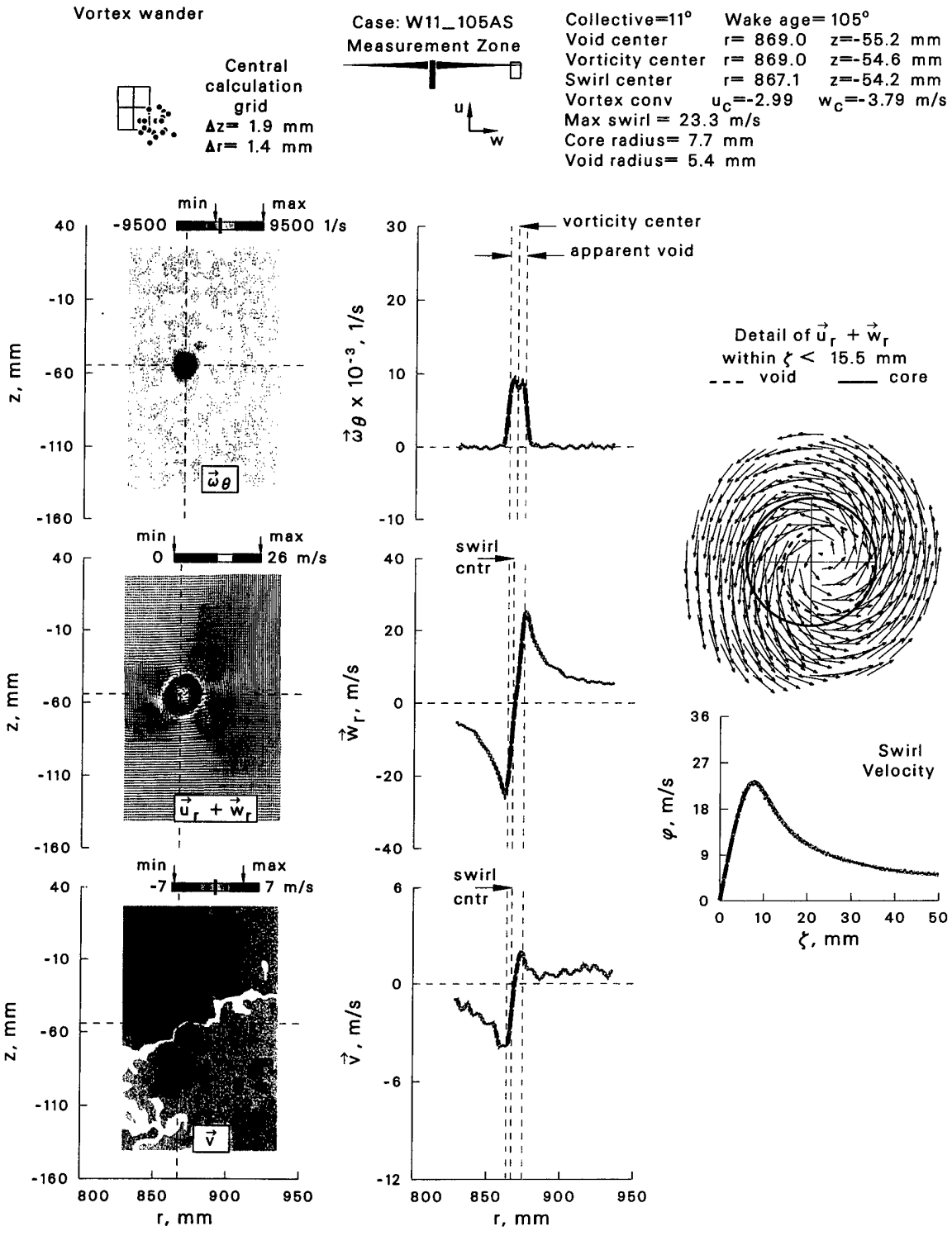

Figure 22: Velocity and vorticity characteristics with reference to the center of swirl at $\psi = 105°$.

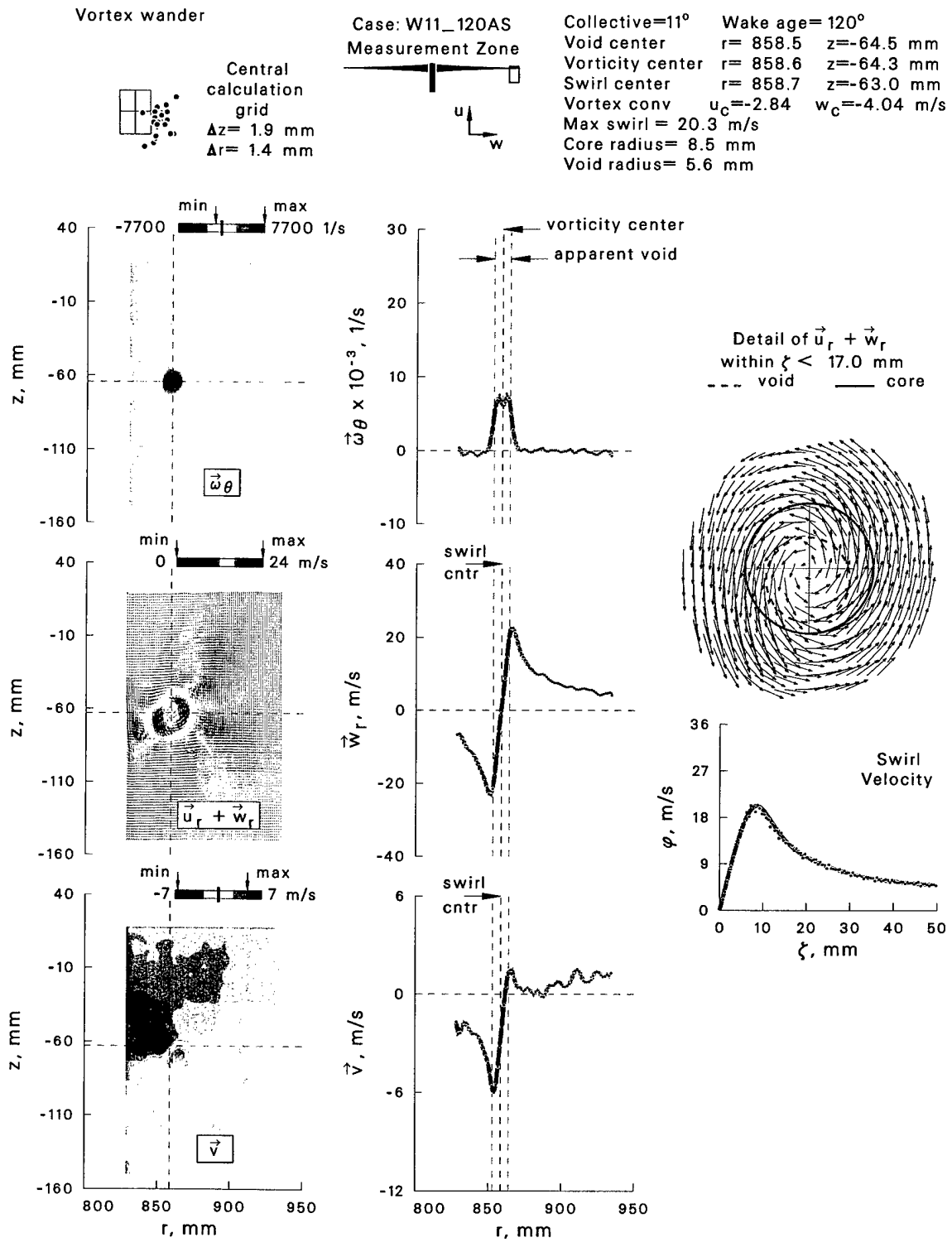

Figure 23: Velocity and vorticity characteristics with reference to the center of swirl at $\psi = 120°$.

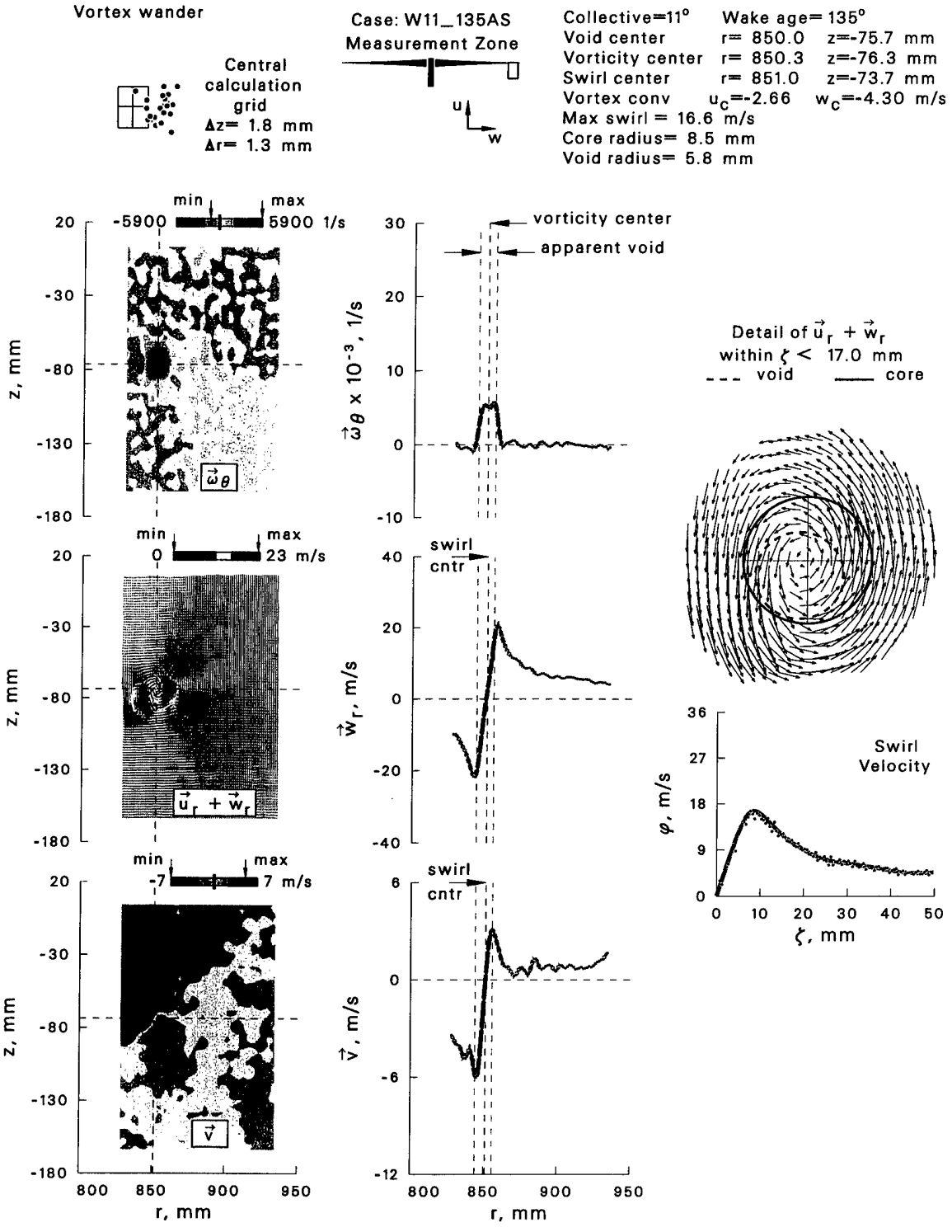

Figure 24: Velocity and vorticity characteristics with reference to the center of swirl at $\psi = 135°$.

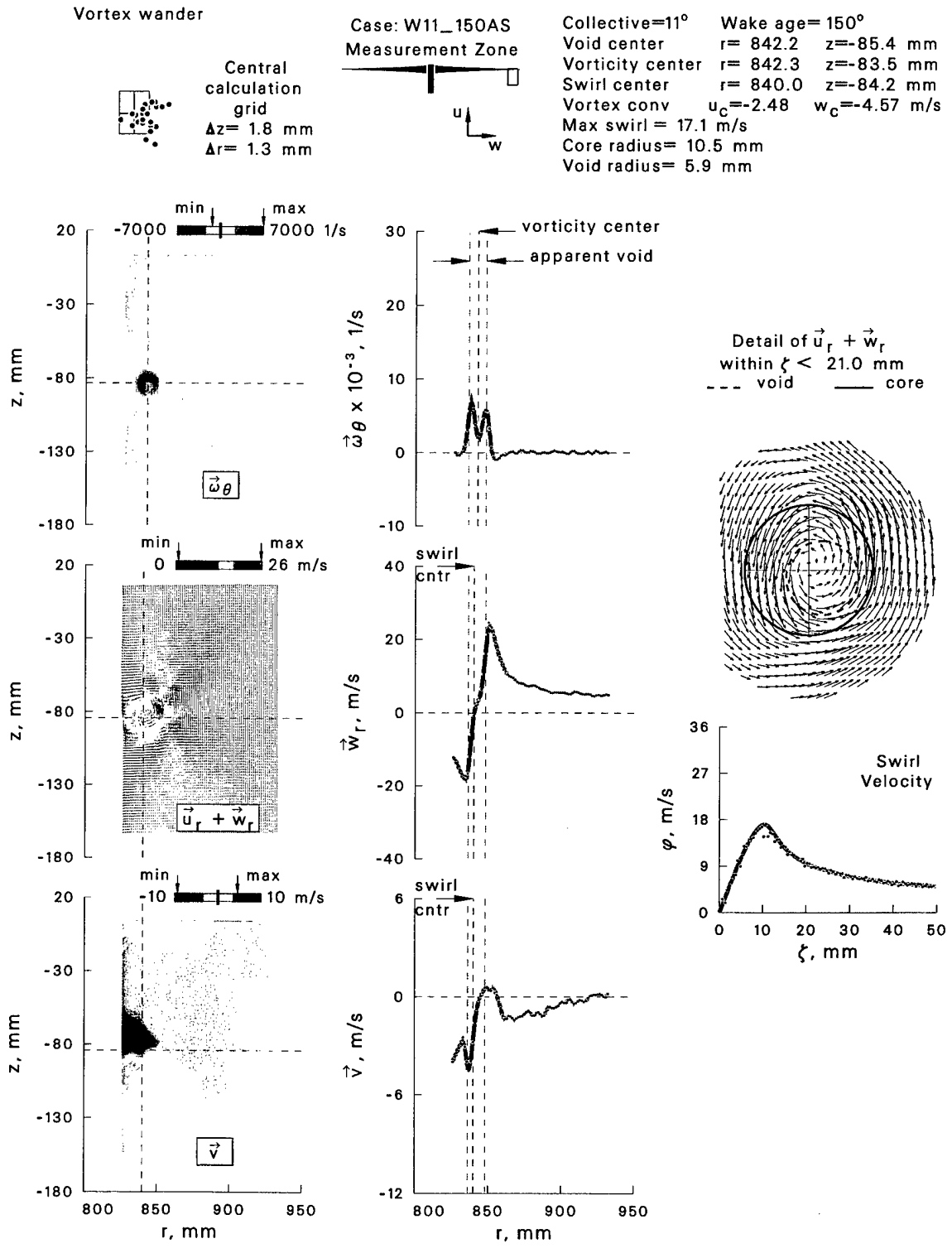

Figure 25: Velocity and vorticity characteristics with reference to the center of swirl at $\psi = 150°$.

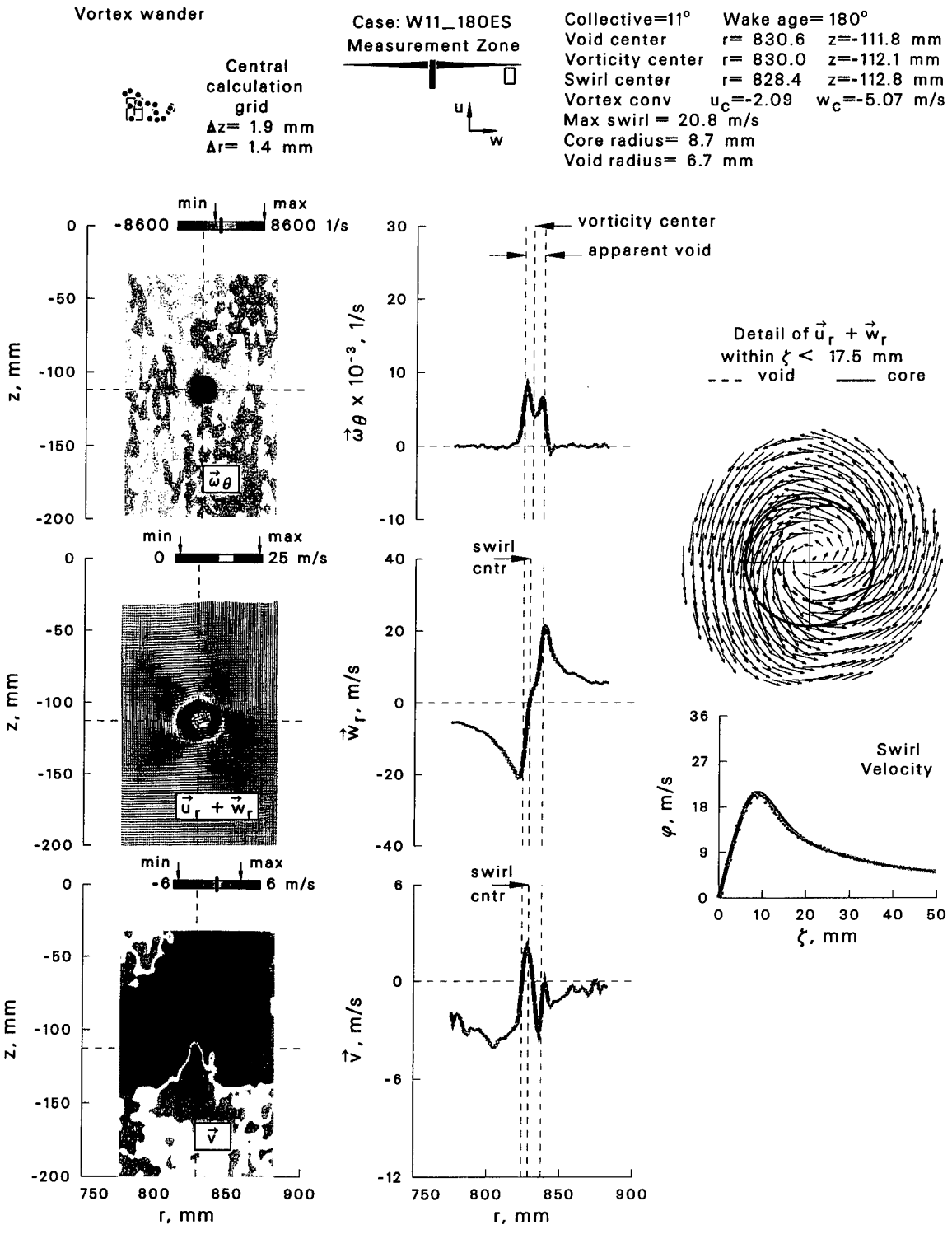

Figure 26: Velocity and vorticity characteristics with reference to the center of swirl at $\psi = 180°$.

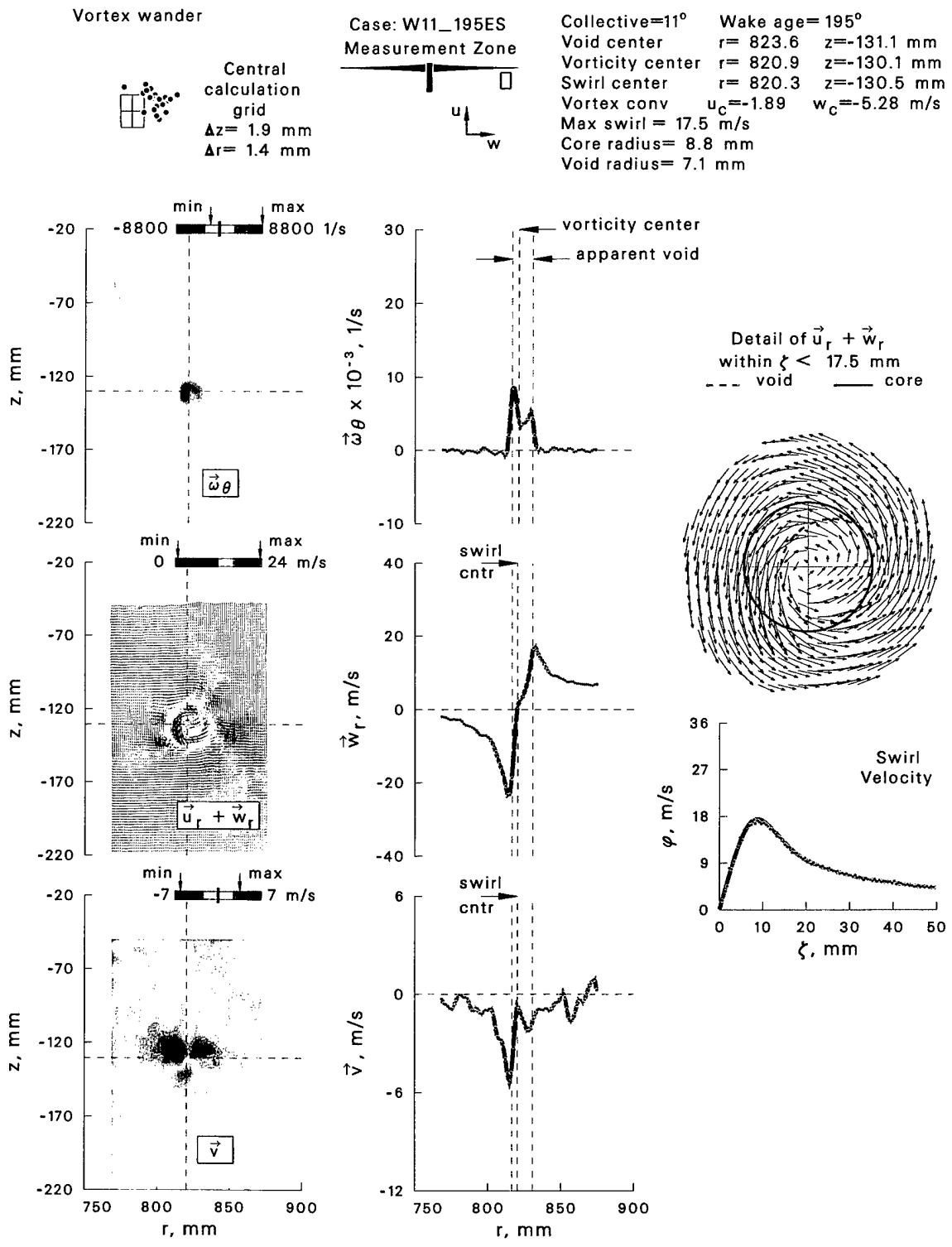

Figure 27: Velocity and vorticity characteristics with reference to the center of swirl at $\psi = 195°$.

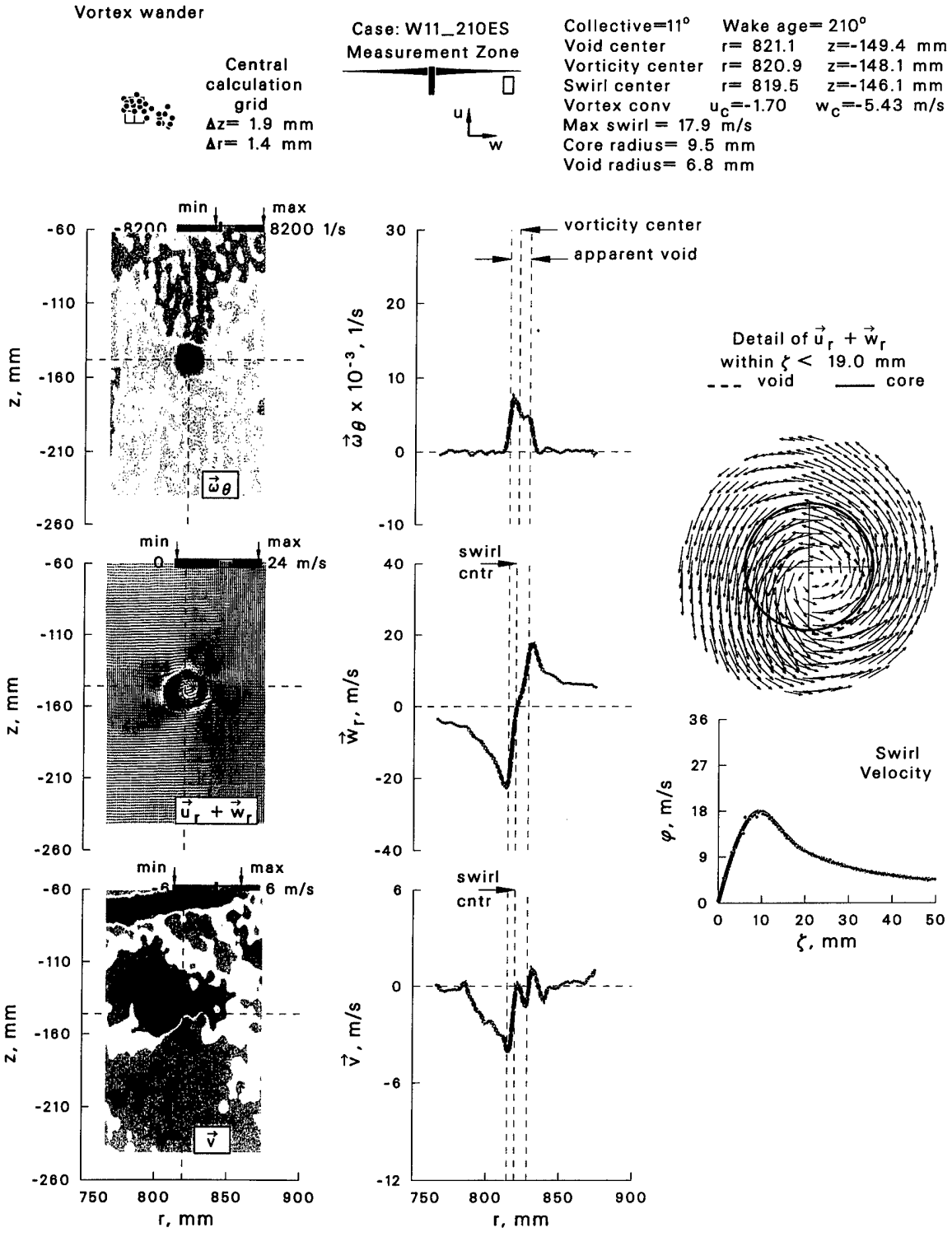

Figure 28: Velocity and vorticity characteristics with reference to the center of swirl at $\psi = 210°$. .

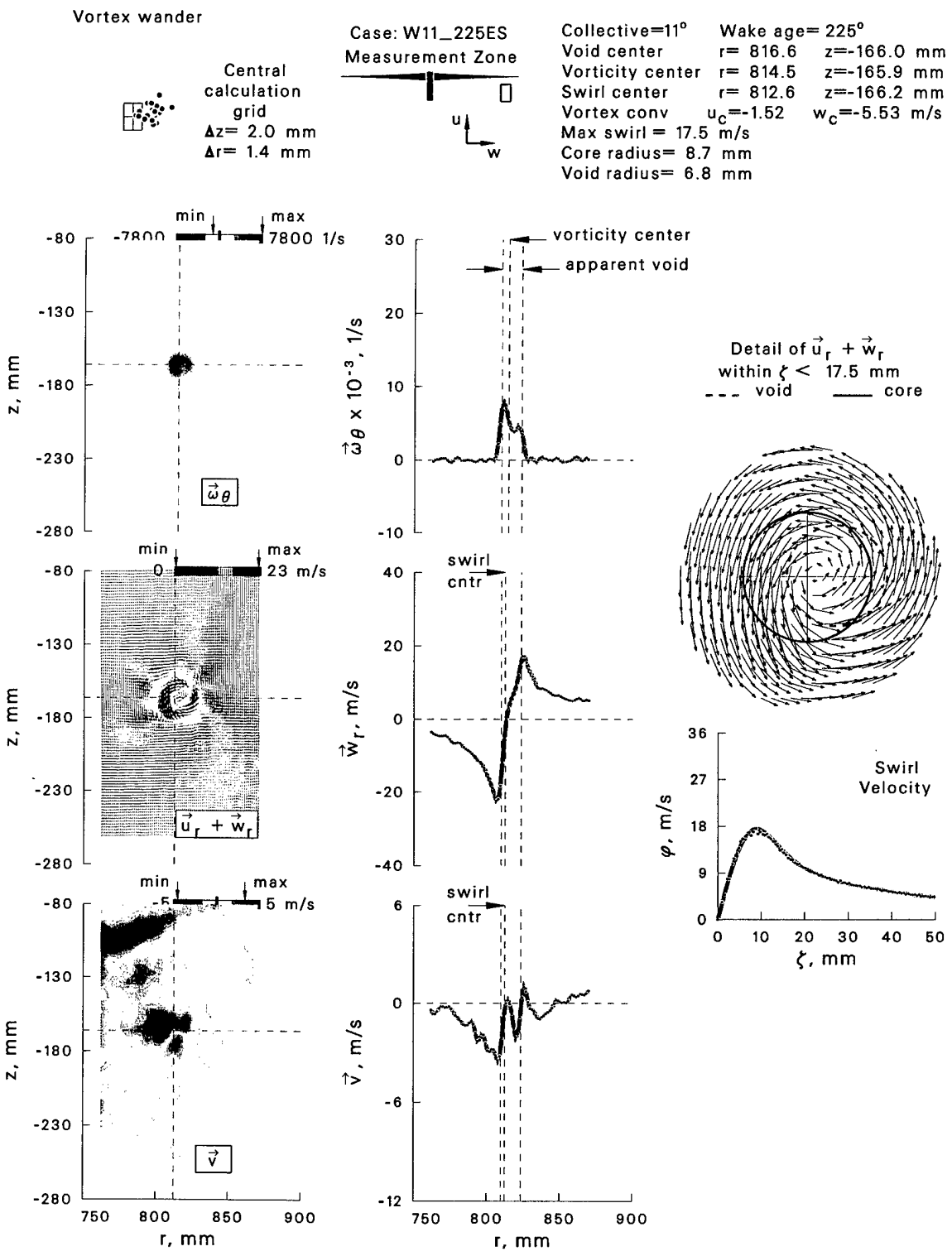

Figure 29: Velocity and vorticity characteristics with reference to the center of swirl at $\psi = 225°$.

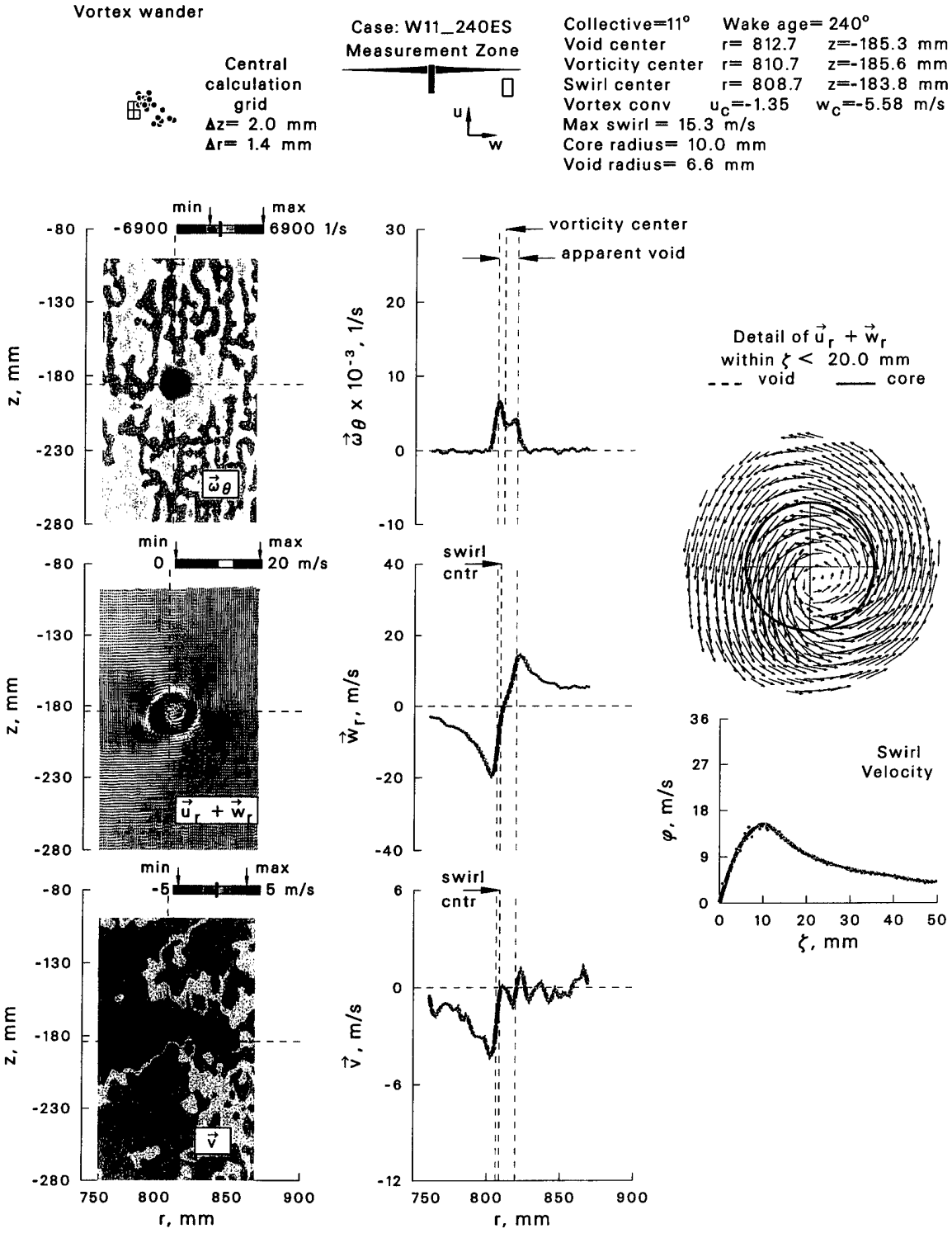

Figure 30: Velocity and vorticity characteristics with reference to the center of swirl at $\psi = 240°$.

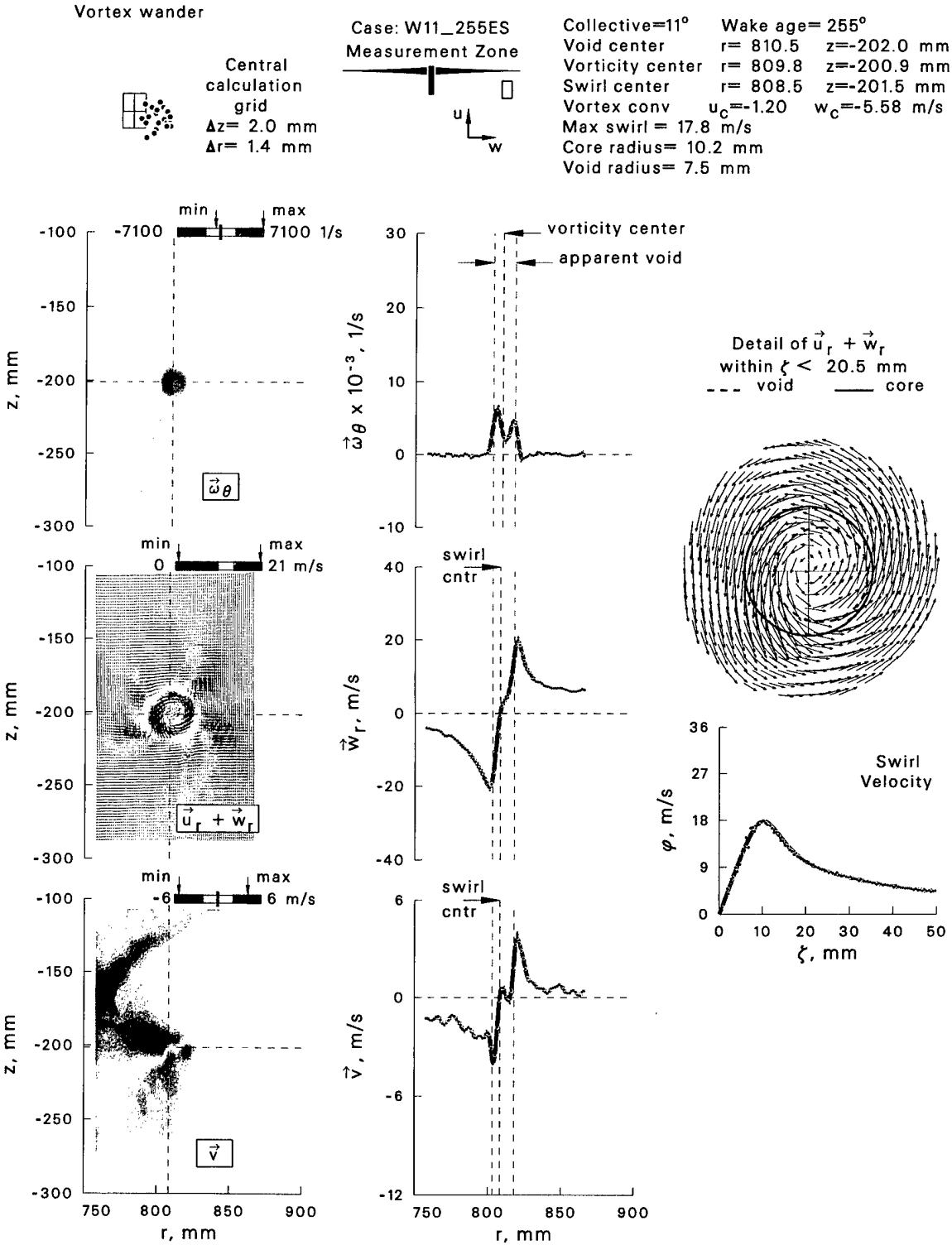

Figure 31: Velocity and vorticity characteristics with reference to the center of swirl at $\psi = 255°$.

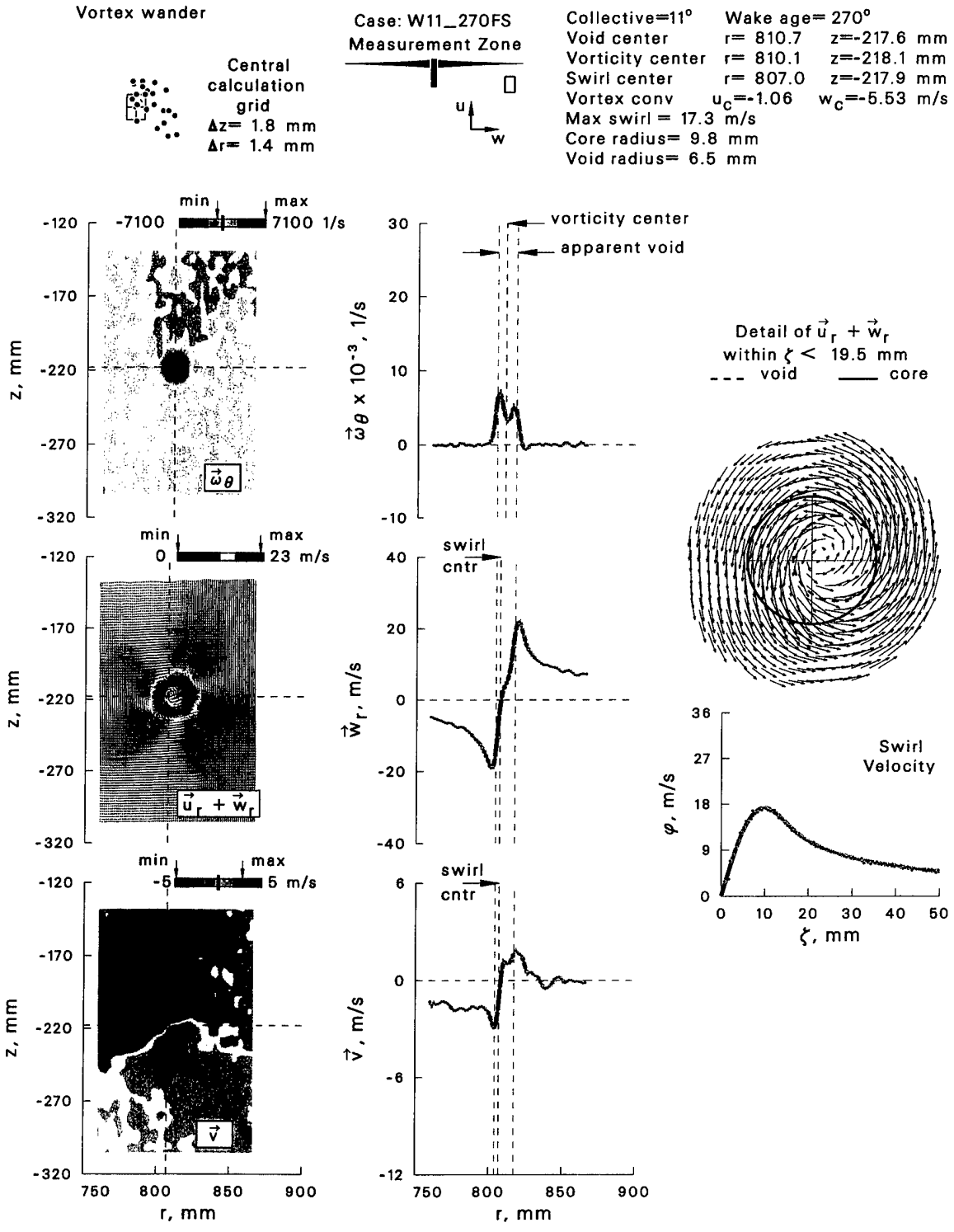

Figure 32: Velocity and vorticity characteristics with reference to the center of swirl at $\psi = 270°$.

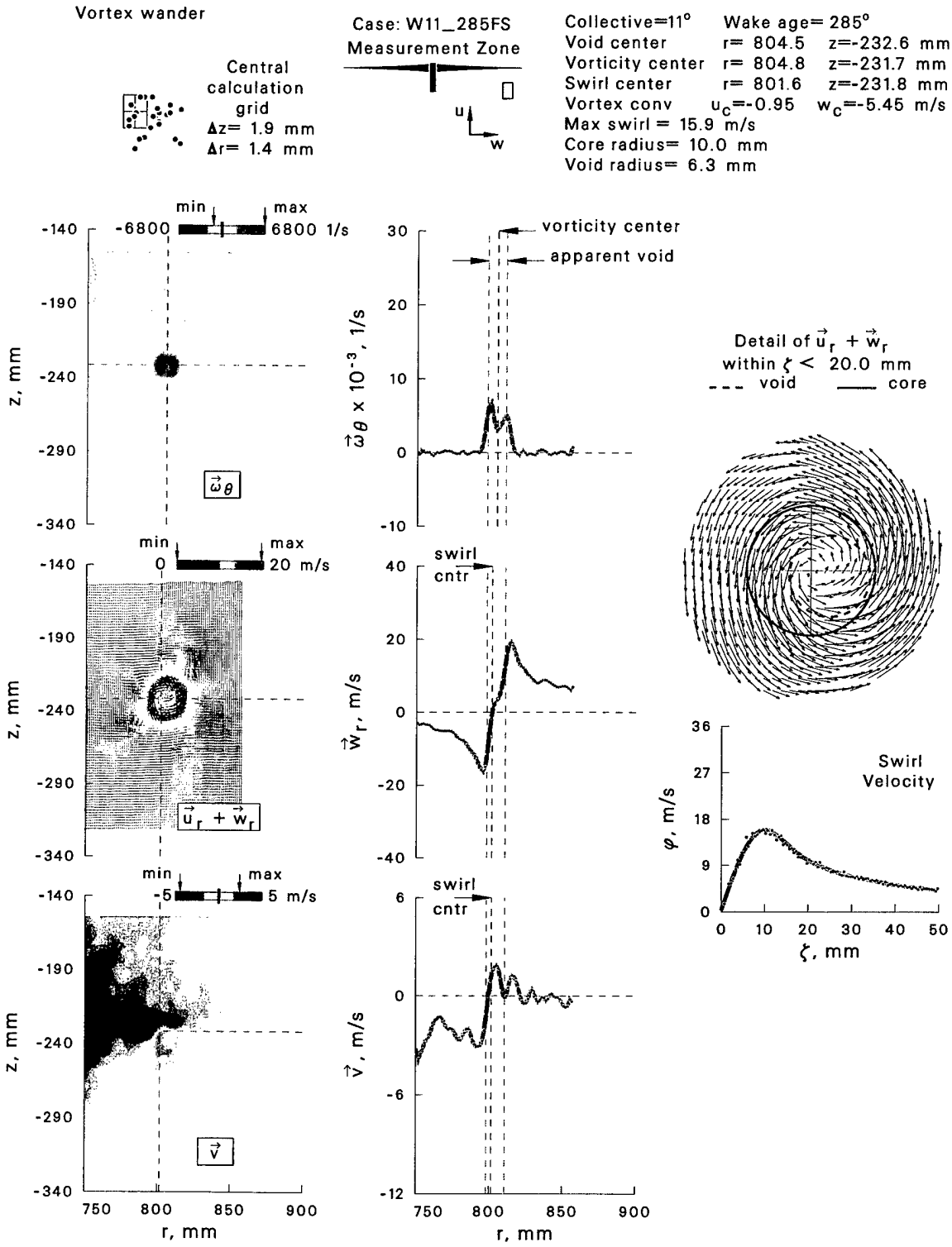

Figure 33: Velocity and vorticity characteristics with reference to the center of swirl at $\psi = 285°$.

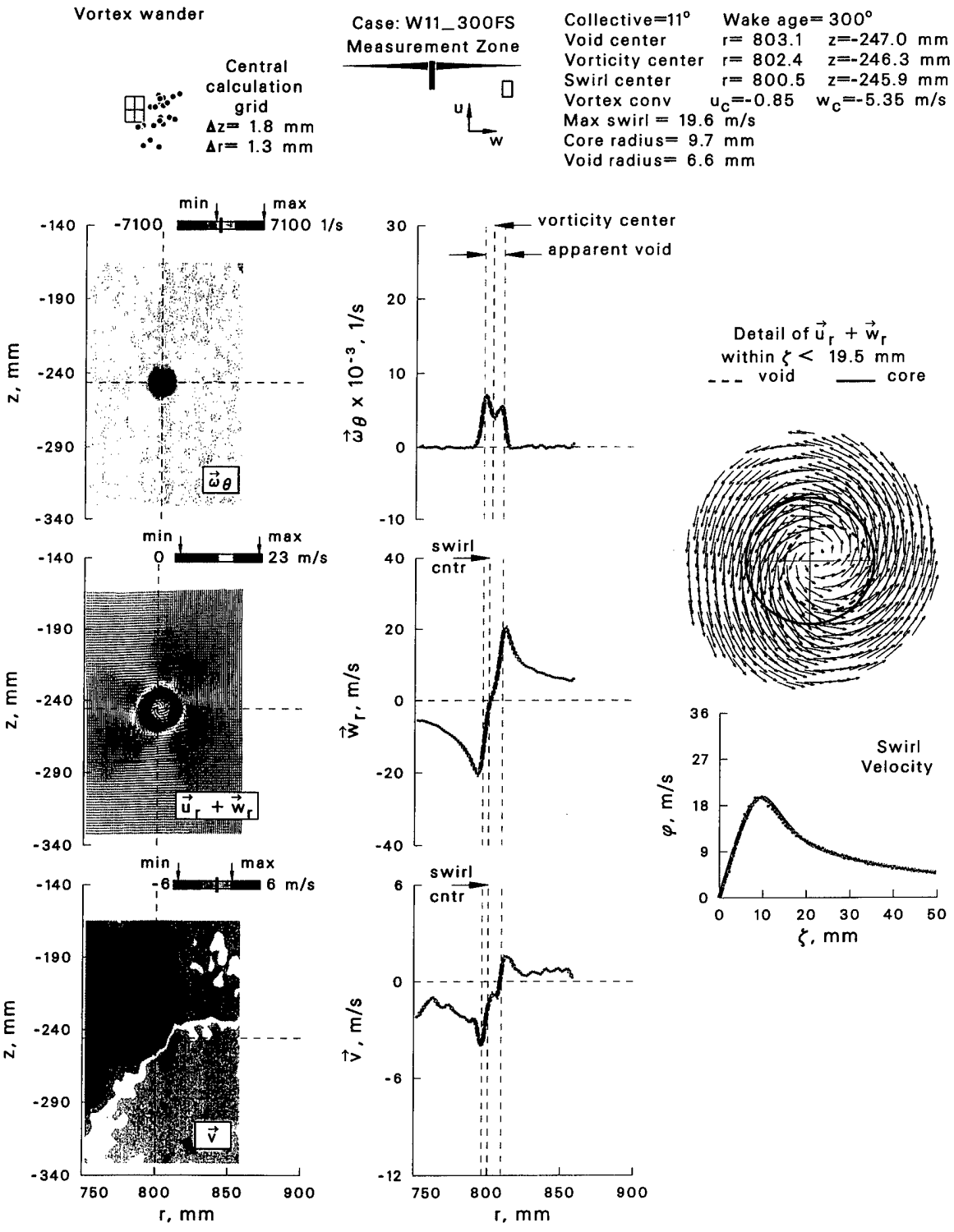

Figure 34: Velocity and vorticity characteristics with reference to the center of swirl at $\psi = 300°$.

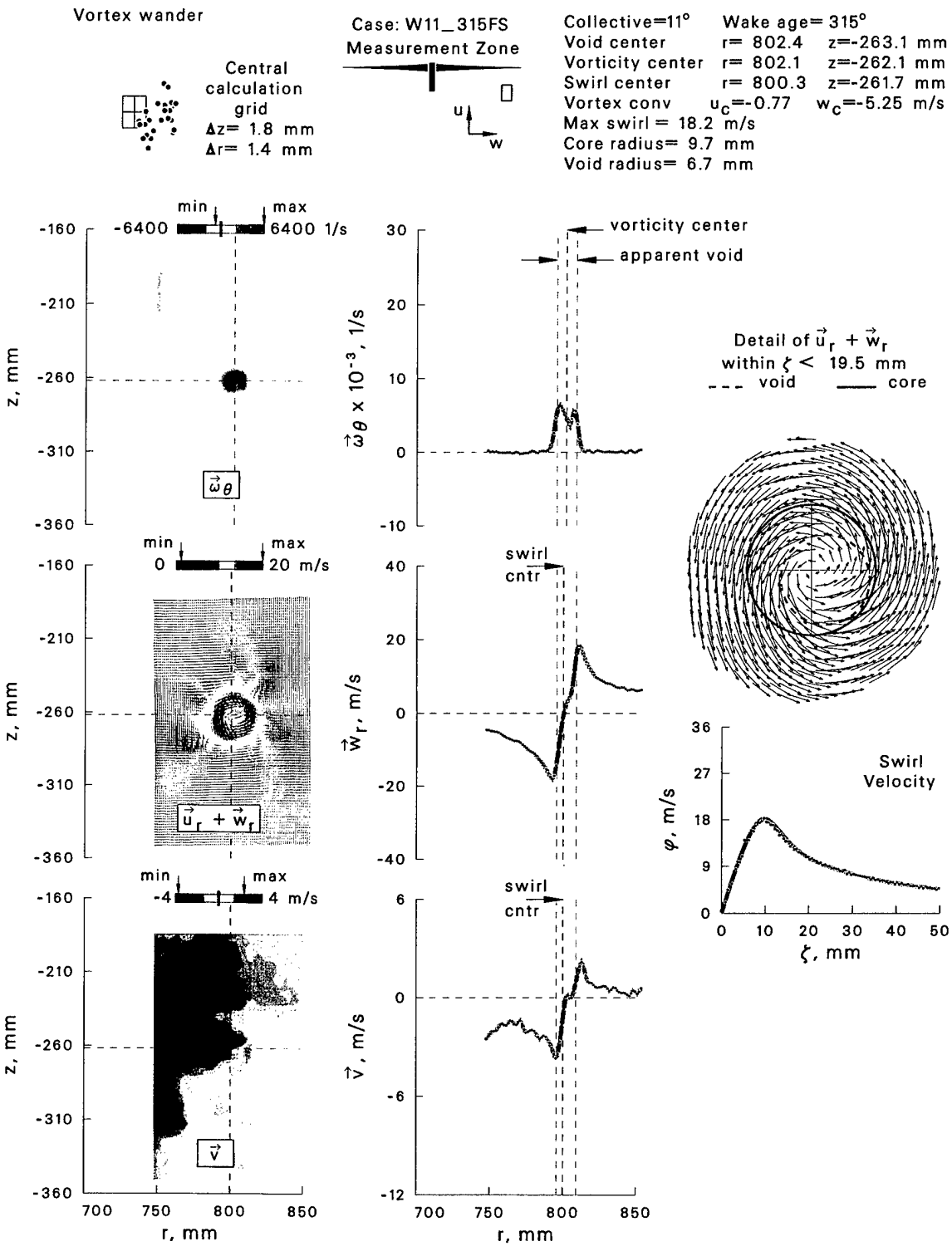

Figure 35: Velocity and vorticity characteristics with reference to the center of swirl at $\psi = 315°$.

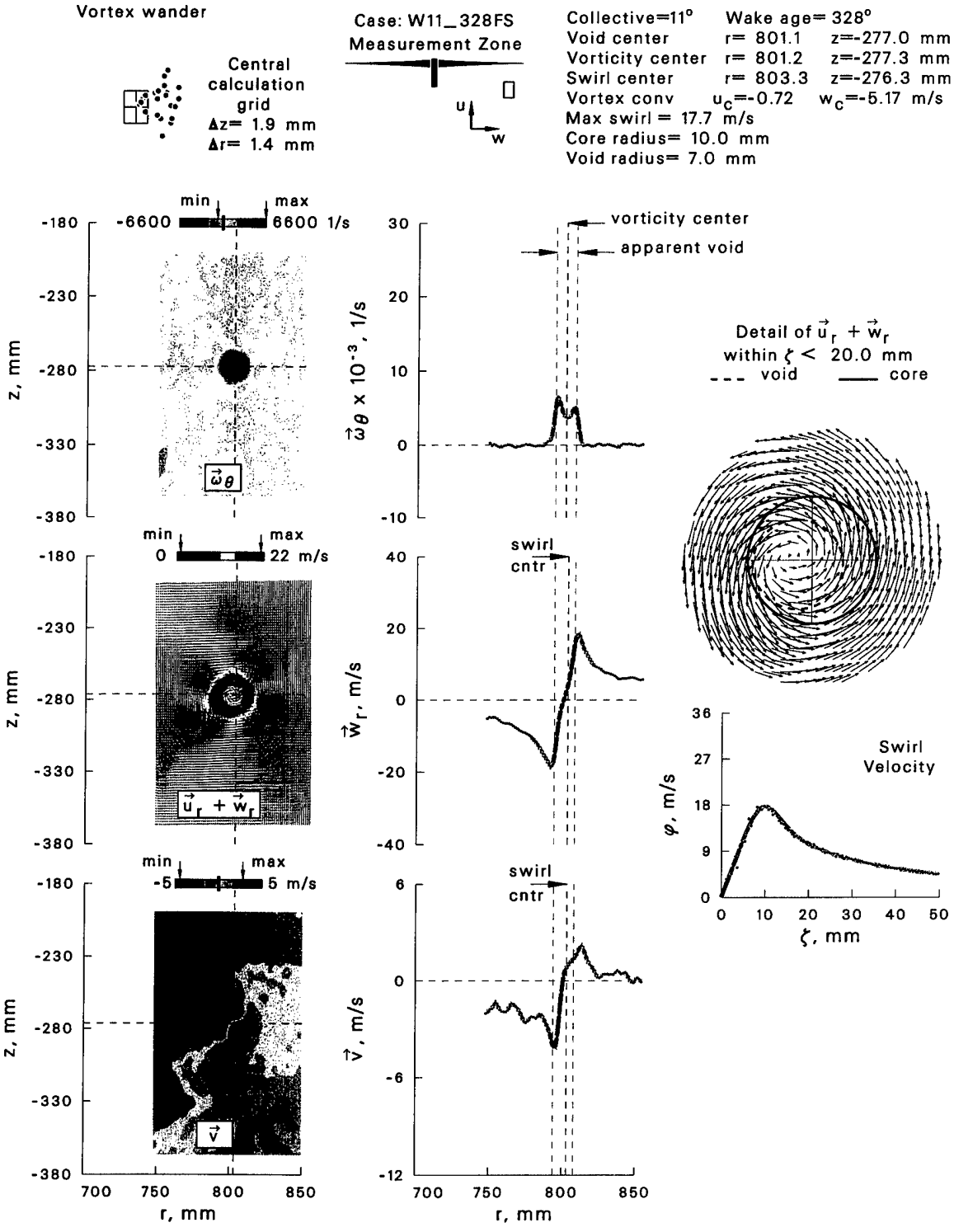

Figure 36: Velocity and vorticity characteristics with reference to the center of swirl at $\psi = 328°$.

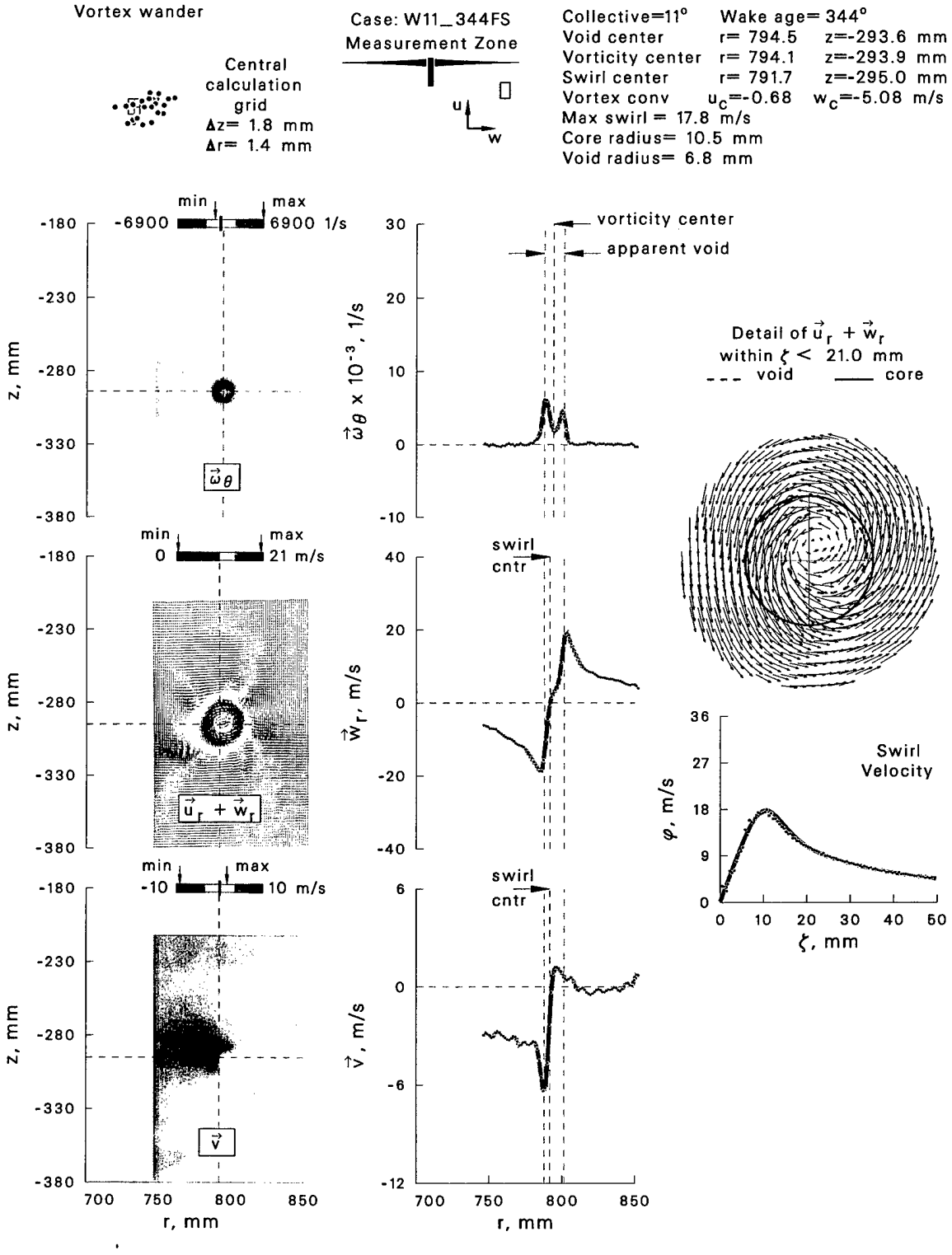

Figure 37: Velocity and vorticity characteristics with reference to the center of swirl at $\psi = 344°$.

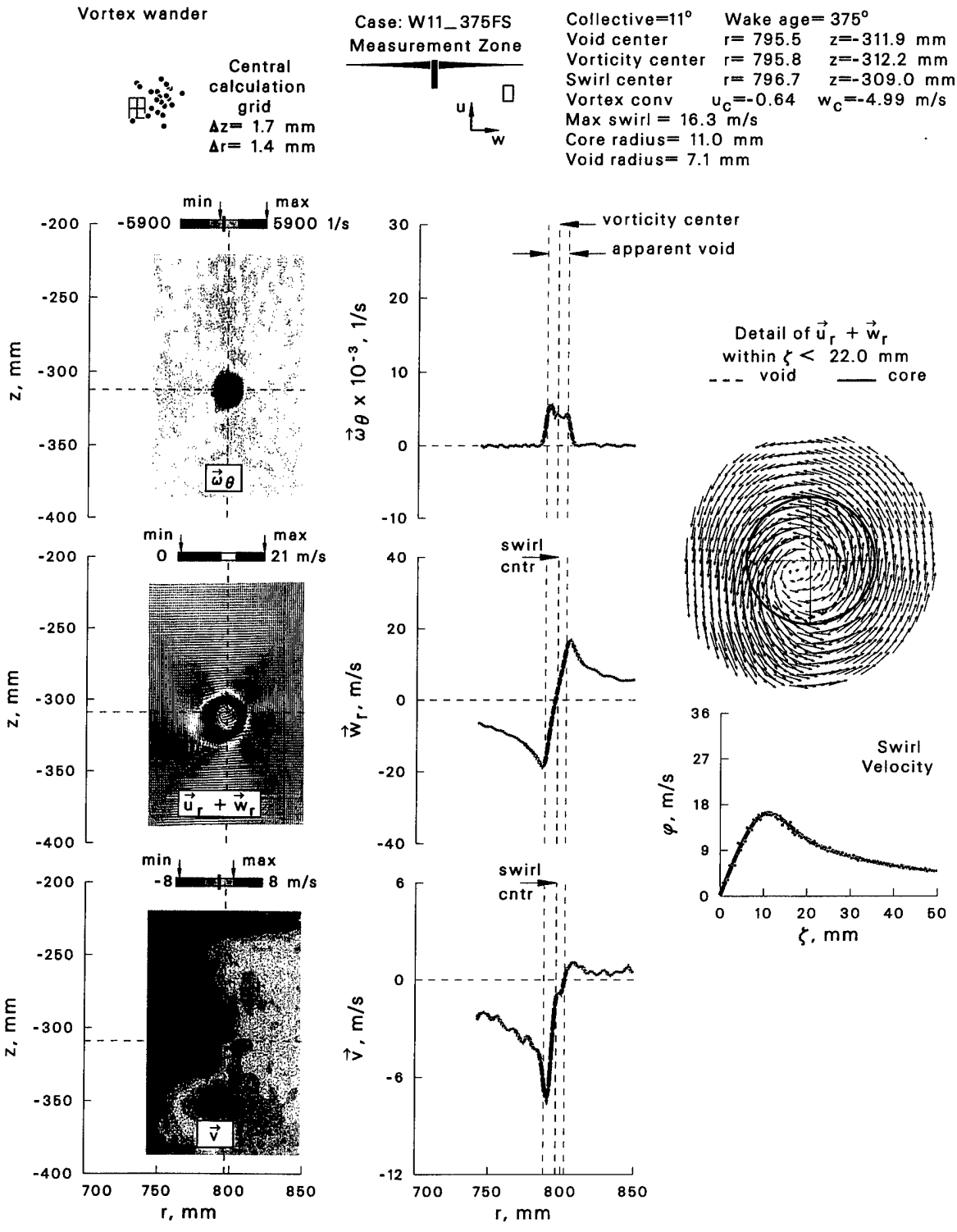

Figure 38: Velocity and vorticity characteristics with reference to the center of swirl at $\psi = 375°$.

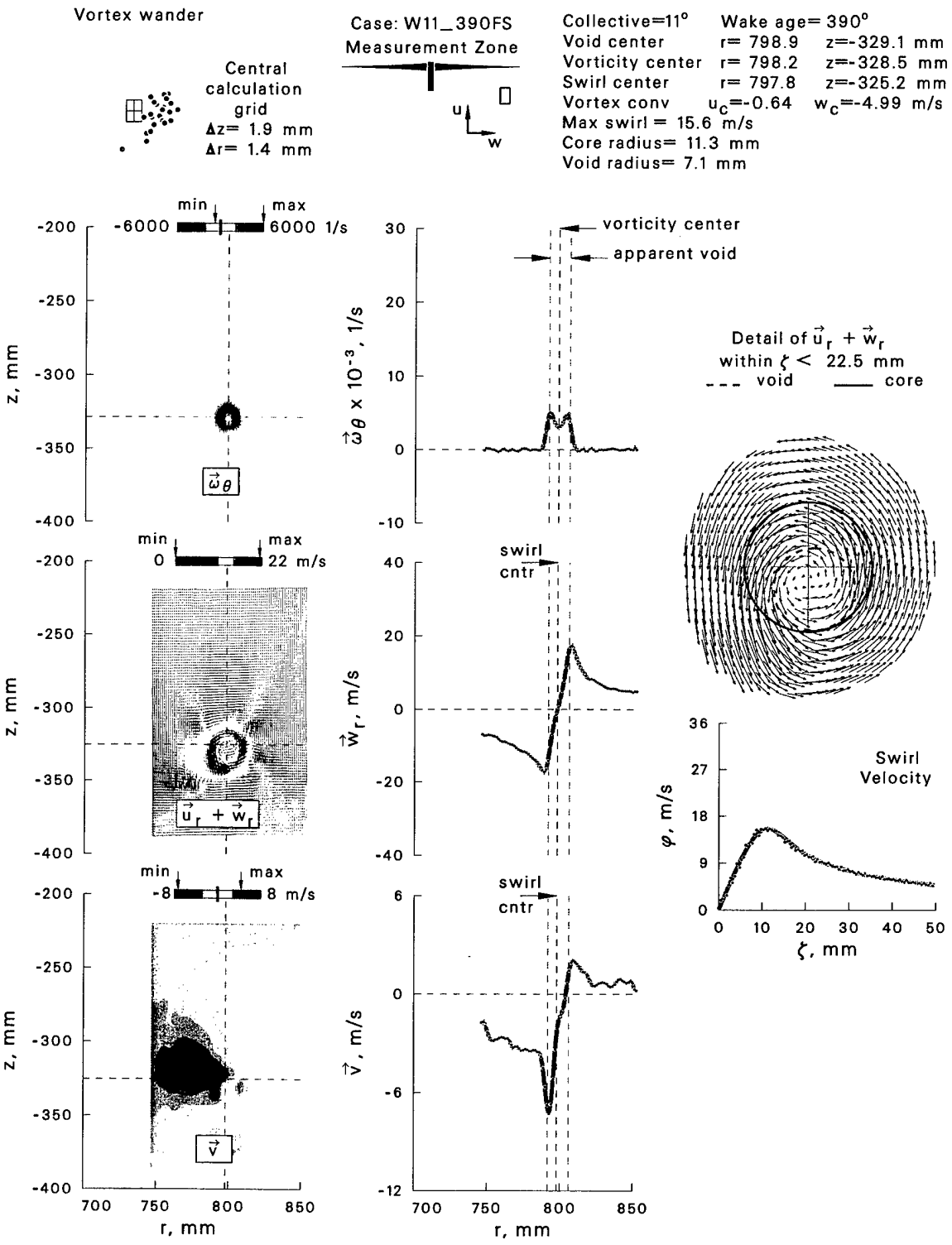

Figure 39: Velocity and vorticity characteristics with reference to the center of swirl at $\psi = 390°$.

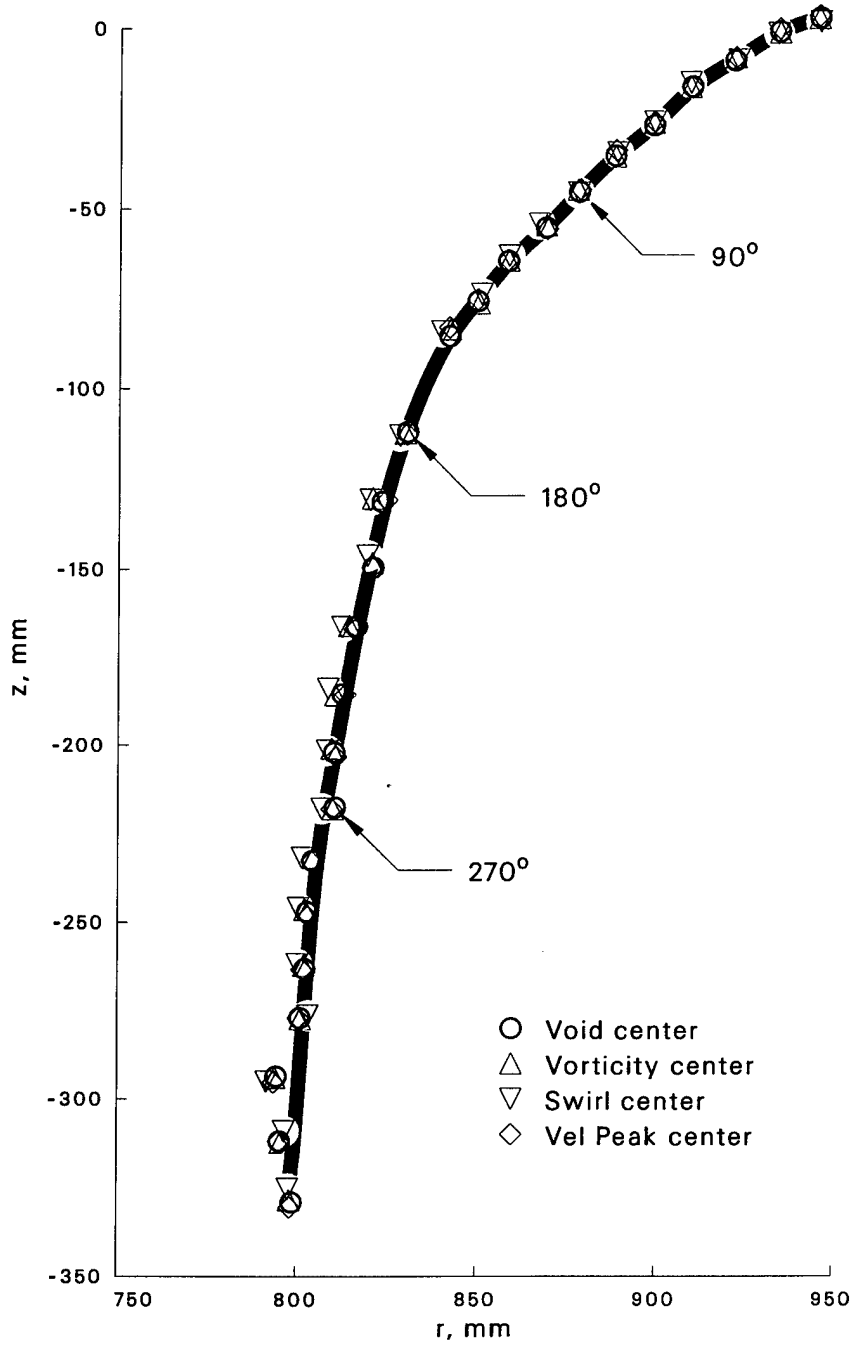

Figure 40: Void, vorticity, and swirl center locations from $\psi = 0°$ to 390°.

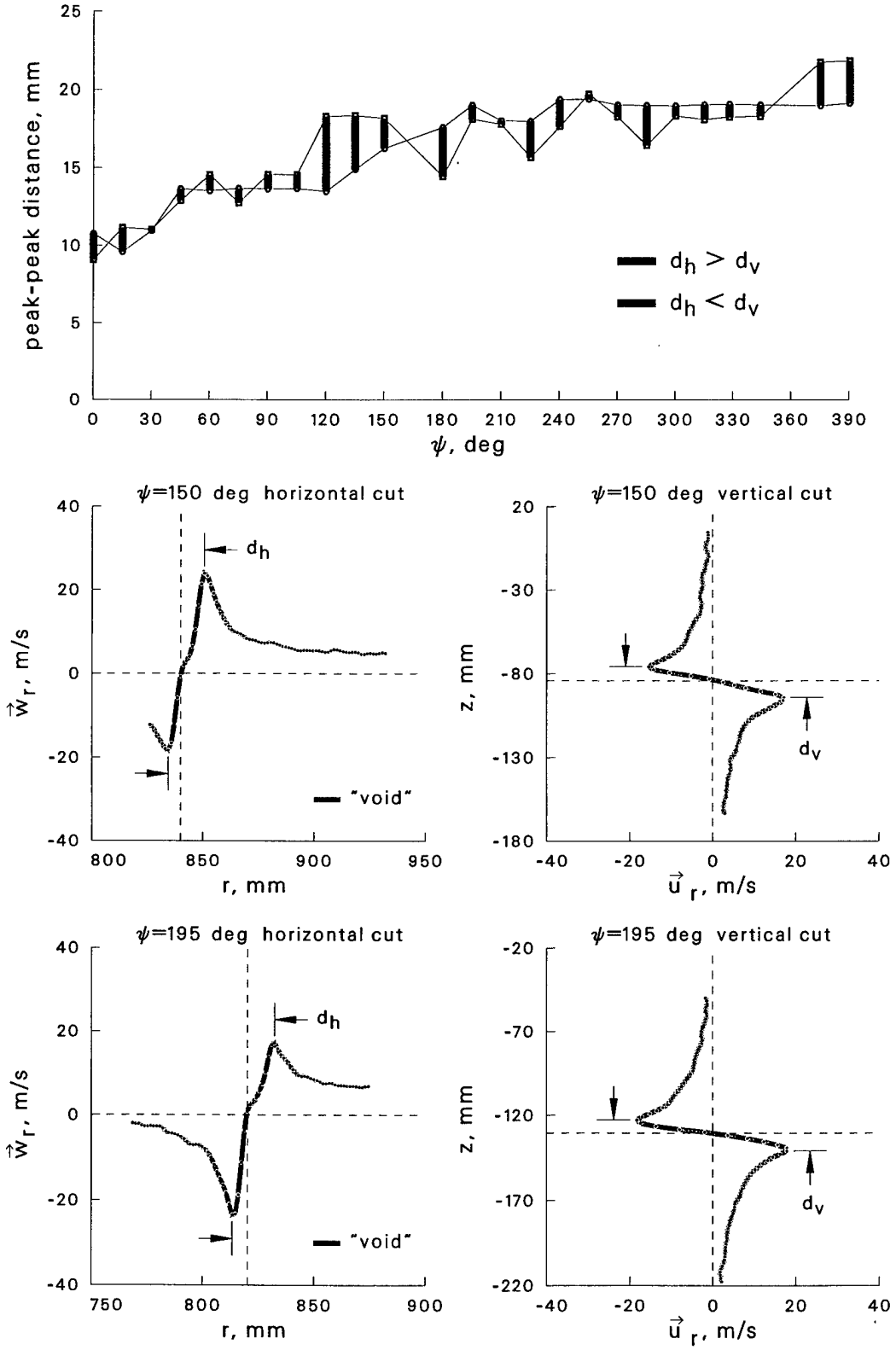

Figure 41: Evidence for the dynamic elliptic shape of the vortex during $\psi = 0°$ to $390°$.

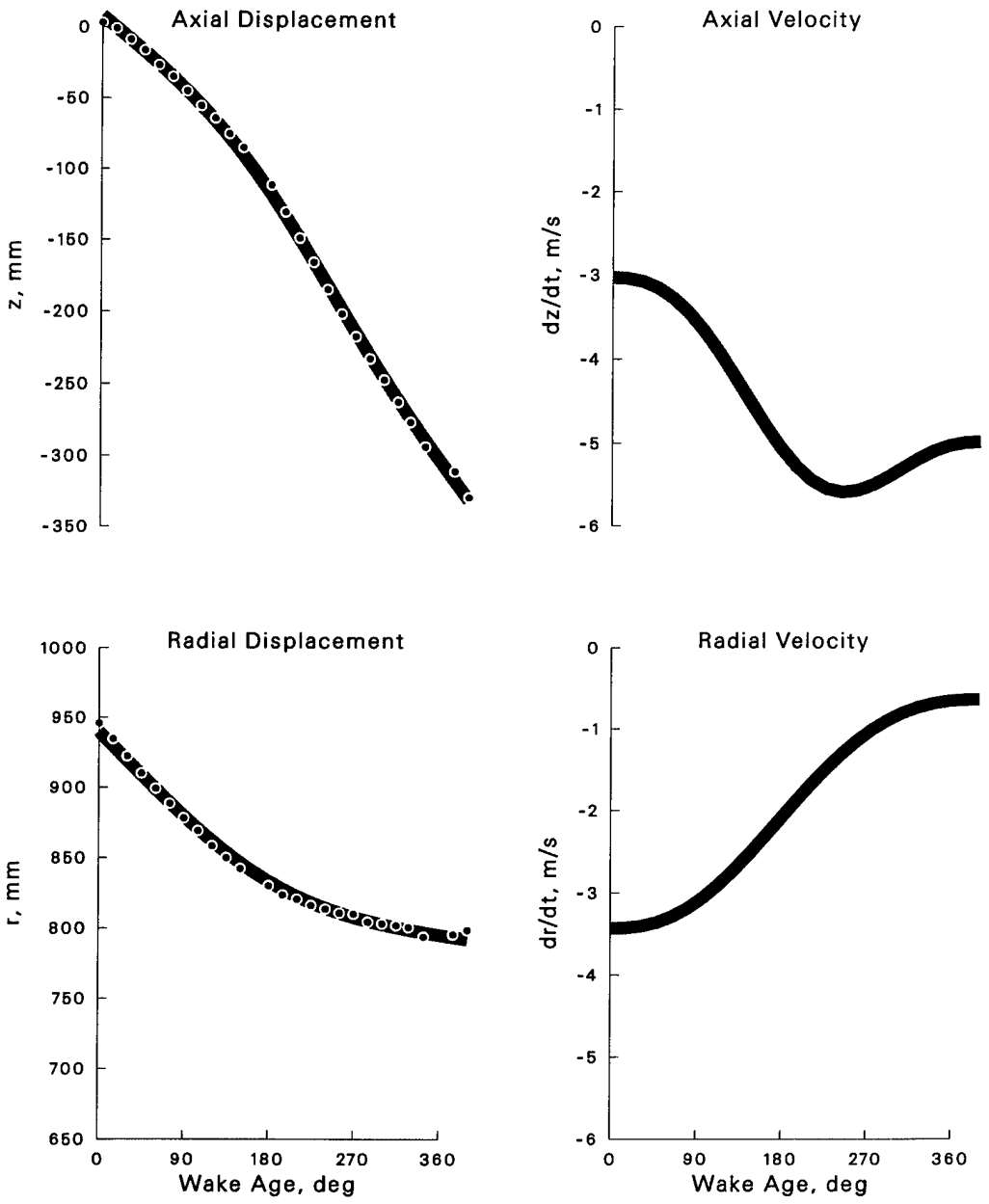

Figure 42: Axial and radial convection of the trailing vortex from $\psi = 0°$ to 390°.

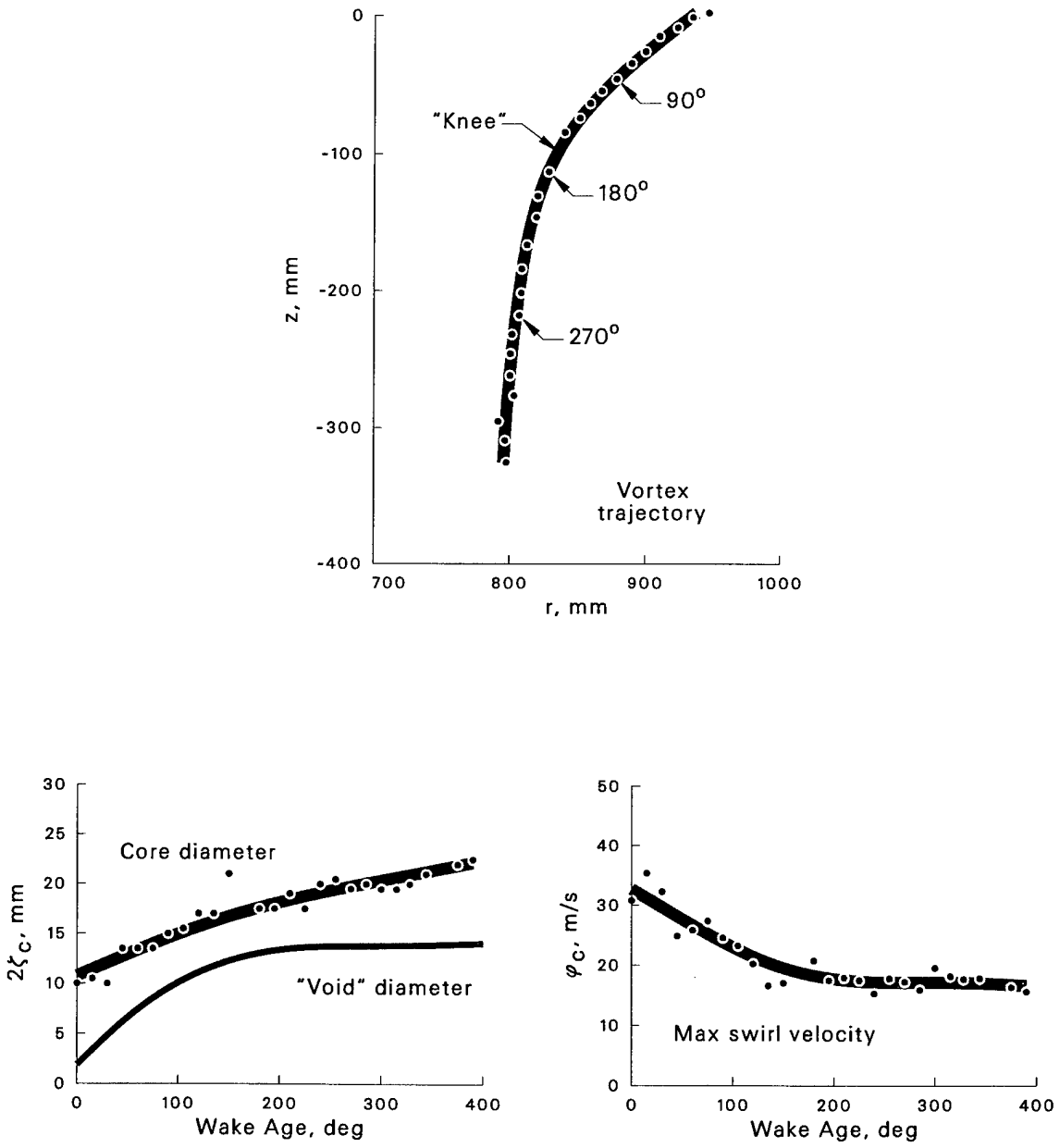

Figure 43: Core size and maximum swirl velocity of the trailing vortex along its trajectory from $\psi = 0°$ to 390°.

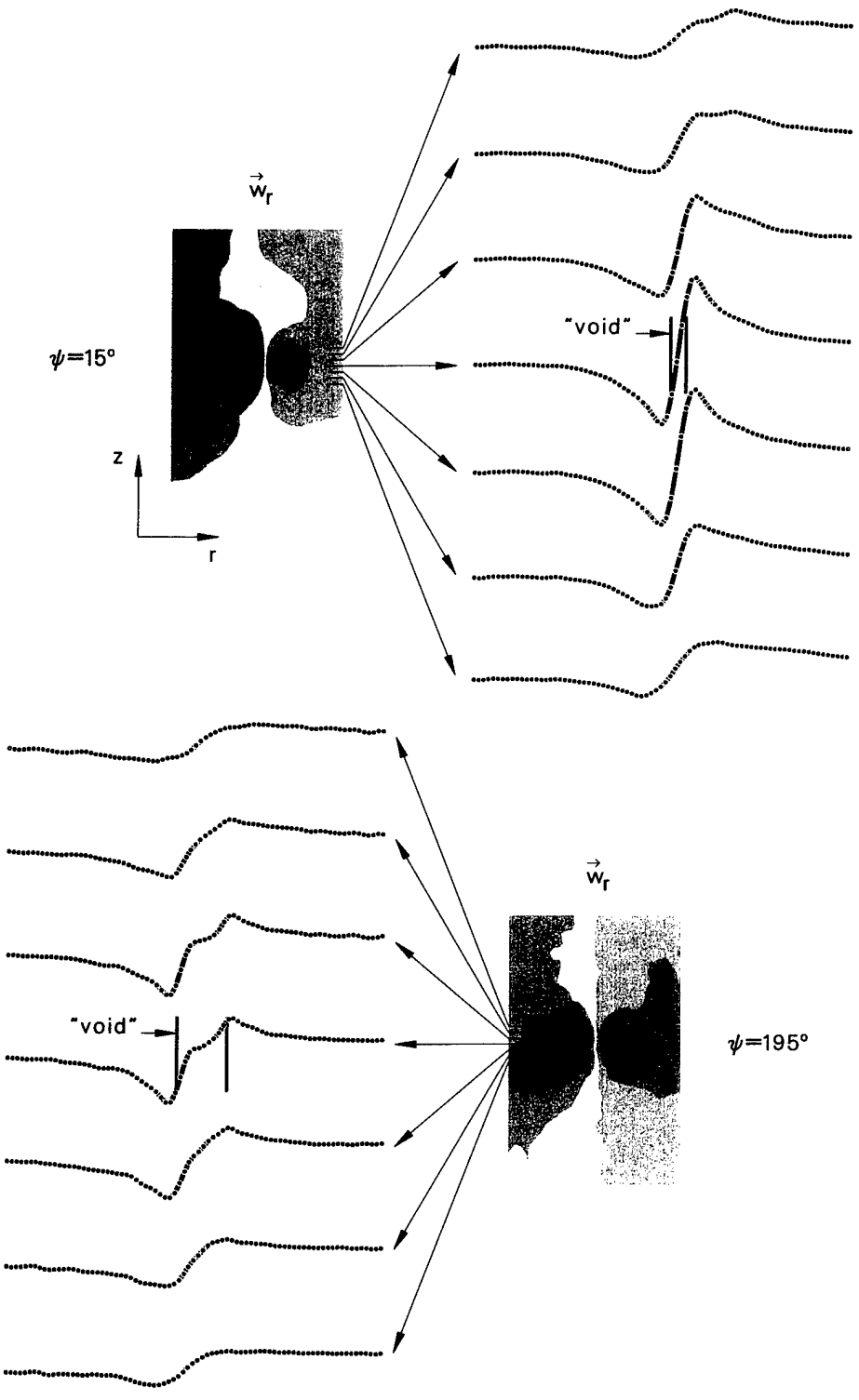

Figure 44: Vertical velocity ($\vec{w}_r$) profiles along several cross sections of the trailing vortex at $\psi = 15°$ and 195°.

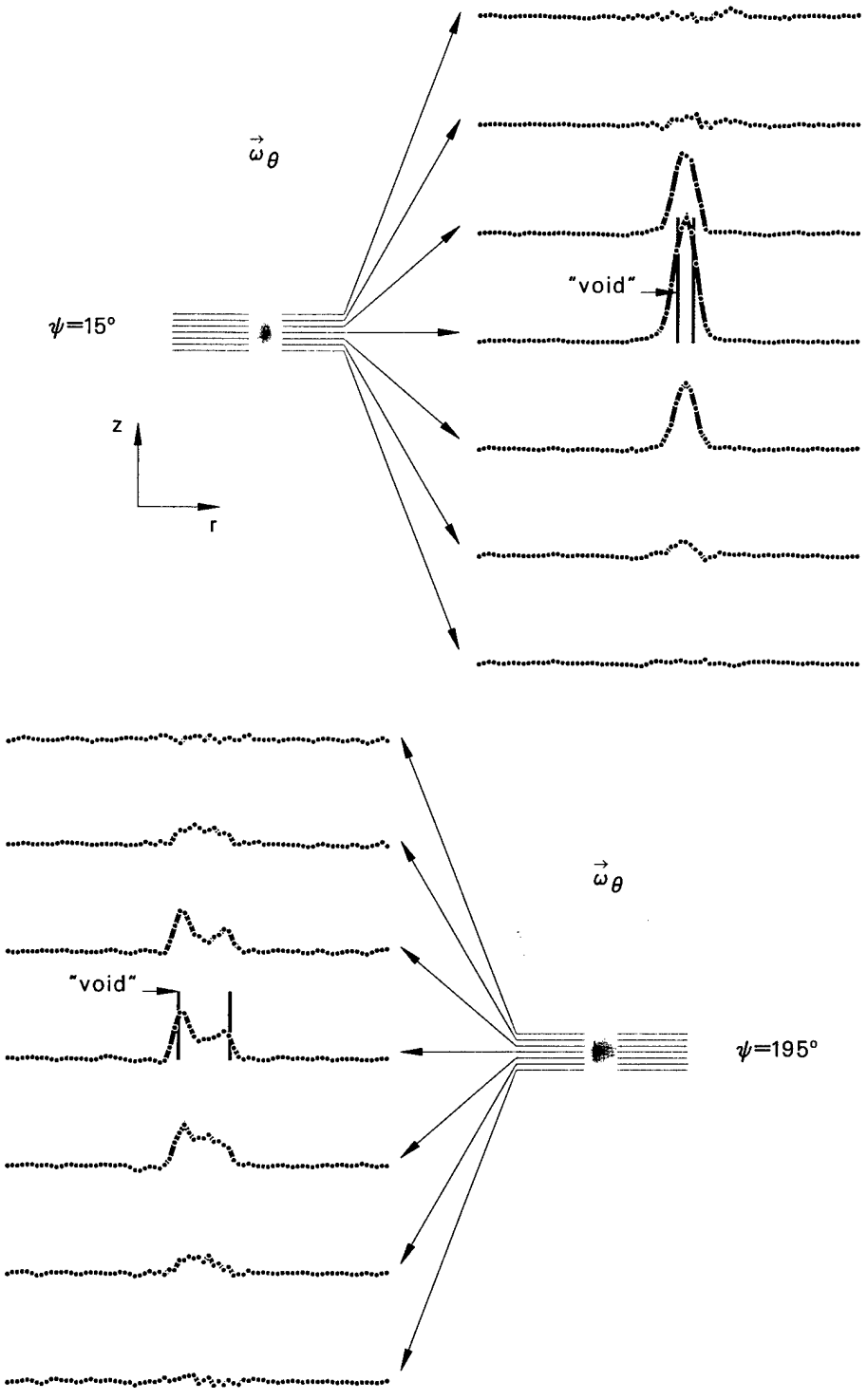

Figure 45: Vorticity ($\vec{\omega}_\theta$) profiles along several cross sections of the trailing vortex at $\psi = 15°$ and 195°.

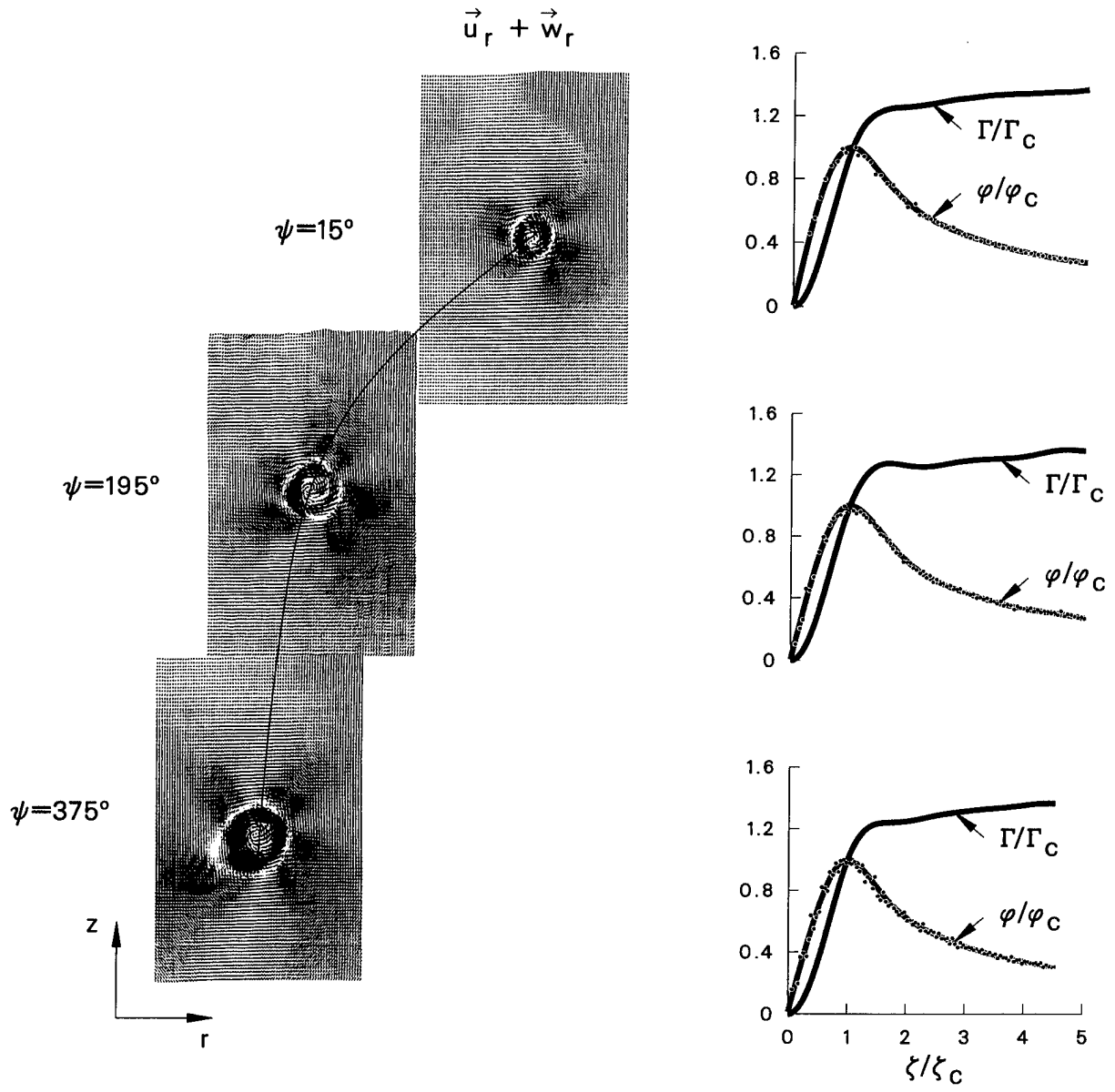

Figure 46: Circulation (Γ) and swirl velocity (σ), calculated along radius ζ relative to the swirl center using the inplane velocity field at $\psi = 15°$, 195°, and 375°.

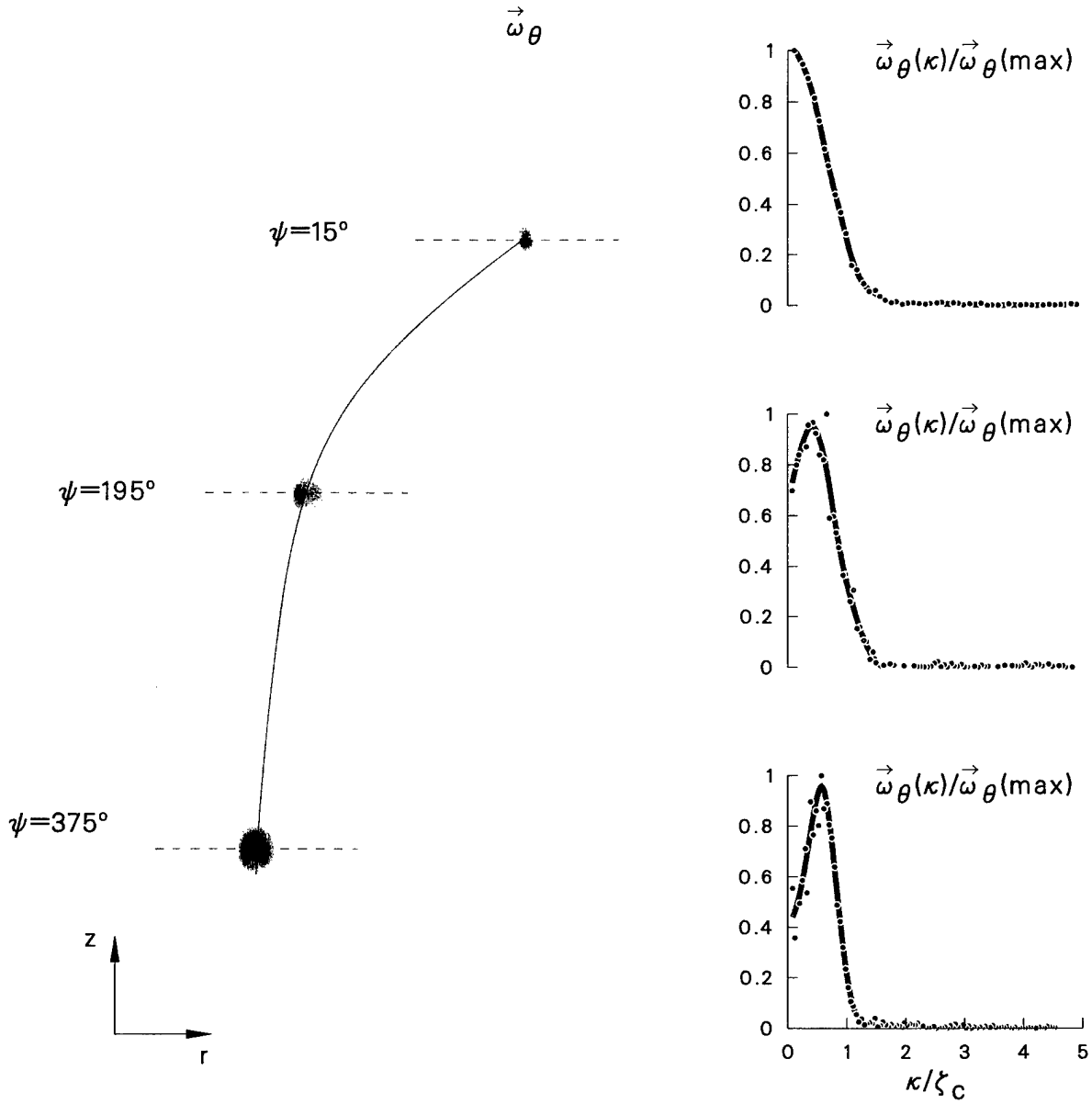

Figure 47: Vorticity ($\vec{\omega}_\theta$), calculated along radius κ relative to the vorticity center using the inplane velocity field at $\psi = 15°$, 195°, and 375°.

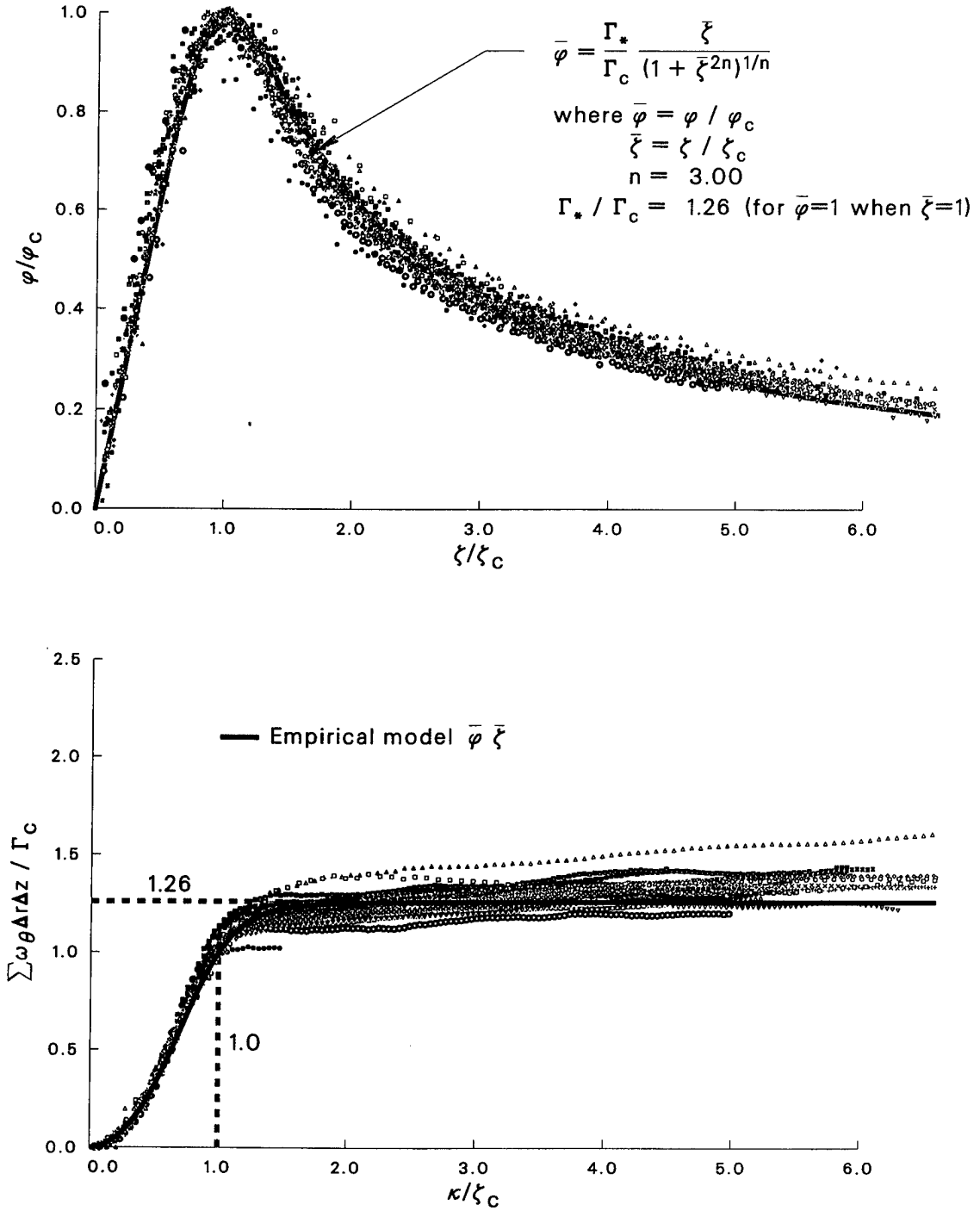

Figure 48: Nondimensional swirl velocity and vorticity distributions for all wake ages $\psi = 0°$ to 390°.

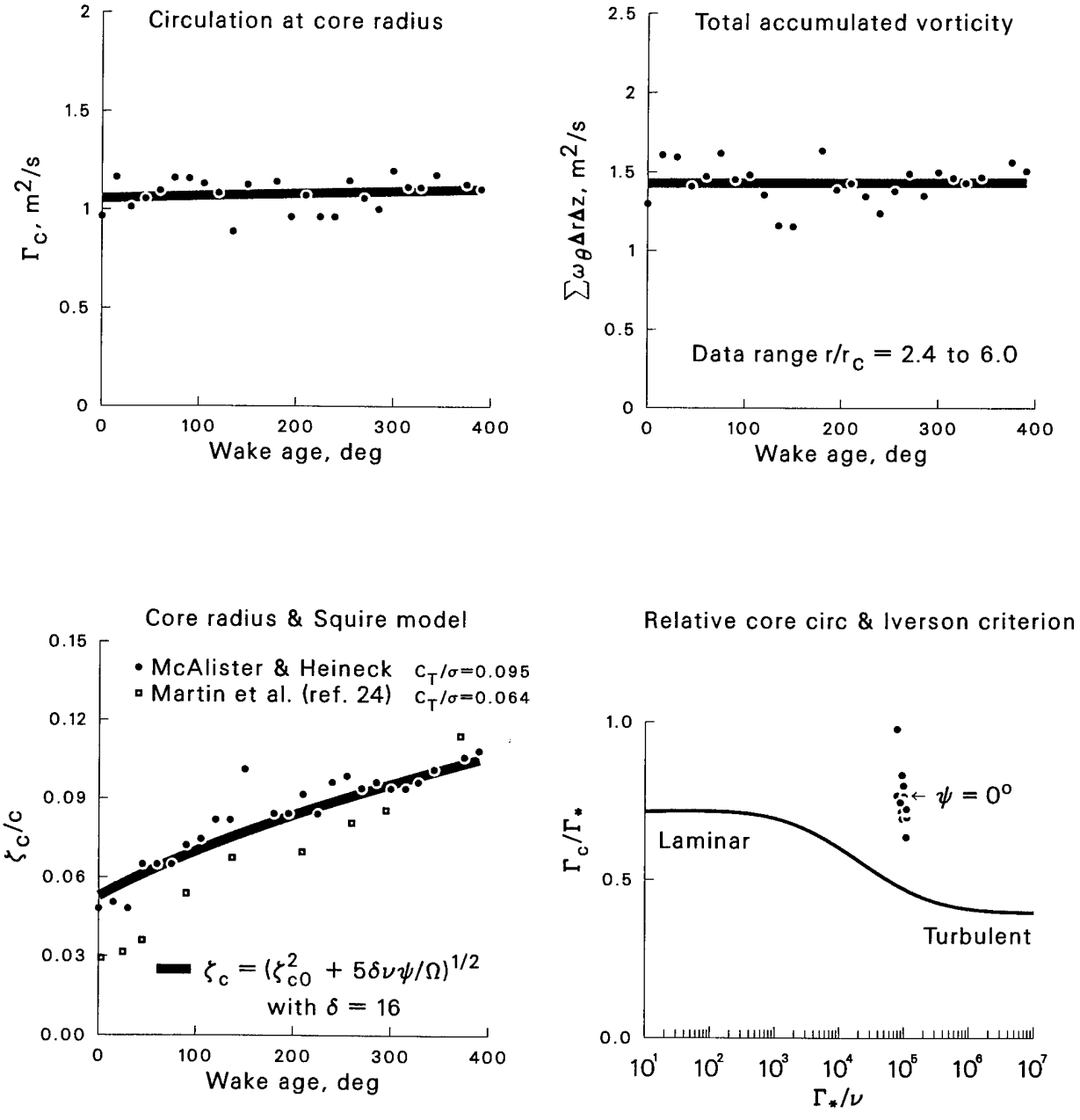

Figure 49: Vortex size and strength during wake ages $\psi = 0°$ to 390°.

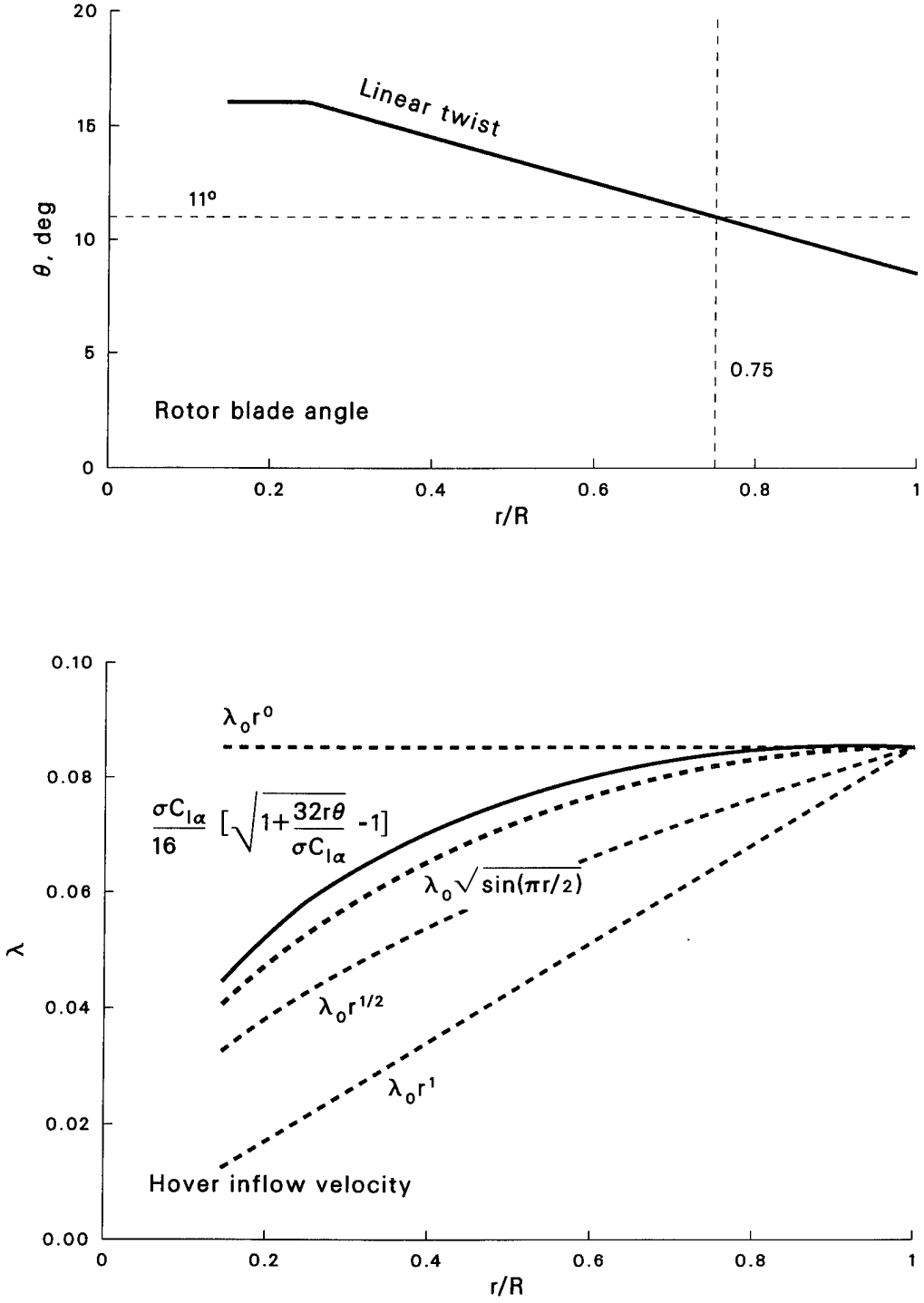

Figure 50: Local blade angle and hover inflow velocity.

REPORT DOCUMENTATION PAGE

Form Approved
OMB No. 0704-0188

1. REPORT DATE *(DD-MM-YYYY)*	2. REPORT TYPE	3. DATES COVERED *(From - To)*
01-05-2002	Technical Paper	

4. TITLE AND SUBTITLE
Measurements of the Early Development of Trailing Vorticity from a Rotor

5a. CONTRACT NUMBER

5b. GRANT NUMBER

5c. PROGRAM ELEMENT NUMBER

6. AUTHOR(S)
K.W. McAlister and J.T. Heineck

5d. PROJECT NUMBER

5e. TASK NUMBER

5f. WORK UNIT NUMBER
712-92-43

7. PERFORMING ORGANIZATION NAME(S) AND ADDRESS(ES)
Army/NASA Rotorcraft Division, Aeroflightdynamics Directorate (AMRDEC),
U.S. Army Aviation and Missile Command, Ames Research Center,
Moffett Field, CA 94035 and
Ames Research Center,
Moffett Field, CA 94035

8. PERFORMING ORGANIZATION REPORT NUMBER
A-0208212

9. SPONSORING/MONITORING AGENCY NAME(S) AND ADDRESS(ES)
National Aeronautics and Space Administration
Washington, DC 20546-0001 and U.S. Army Aviation and Missile Command,
Redstone Arsenal, AL 95898-5000

10. SPONSORING/MONITOR'S ACRONYM(S)
NASA/TP-2002-211848
AFDD/TR-02-A-001

11. SPONSORING/MONITORING REPORT NUMBER

12. DISTRIBUTION/AVAILABILITY STATEMENT
Unclassified - Unlimited
Subject Category 02 Distribution: Standard
Availability: NASA CASI (301) 621-0390

13. SUPPLEMENTARY NOTES
Point of Contact: Kenneth W. McAlister, Ames Research Center, Mail Stop 215-1, Moffett Field, CA 94035 (650) 604-5892

14. ABSTRACT

The wake behind a two-bladed model rotor in light climb was measured using particle image velocimetry, with particular emphasis on the development of the trailing vortex during the first revolution of the rotor. The distribution of vorticity was distinguished from the slightly elliptical swirl pattern. Peculiar dynamics within the "void" region may explain why the peak vorticity appeared to shift away from the center as the vortex aged, suggesting the onset of instability. The swirl and axial velocities (which reached 44% and 12% of the rotor tip speed, respectively) were found to be asymmetric relative to the vortex center. In particular, the axial flow was composed of two concentrated zones moving in opposite directions. The radial distribution of the circulation rapidly increased in magnitude until reaching a point just beyond the core radius, after which the rate of growth decreased significantly. The core-radius circulation increased slightly with wake age, but the large-radius circulation appeared to remain relatively constant. The radial distributions of swirl velocity and vorticity exhibit self-similar behaviors, especially within the core. The diameter of the vortex core was initially about 10% of the rotor-blade chord, but more than doubled its size after one revolution of the rotor.

15. SUBJECT TERMS
Rotor wake, Trailing vortex, Model rotor, Particle image velocimetry

16. SECURITY CLASSIFICATION OF:			17. LIMITATION OF ABSTRACT	18. NUMBER OF PAGES	19b. NAME OF RESPONSIBLE PERSON
a. REPORT	b. ABSTRACT	c. THIS PAGE			Kenneth W. McAlister
					19b. TELEPHONE NUMBER *(Include area code)*
Unclassified	Unclassified	Unclassified	Unlimited	67	(650) 604-5892